2011

DESIGN AND ANALYSIS OF MACRO SWITCHED IMPEDANCE MOTORS

Weston C. Johnson
University of Kentucky, weston@clutejohnson.com

STUDENT AGREEMENT:

I represent that my thesis or dissertation and abstract are my original work. Proper attribution has been given to all outside sources. I understand that I am solely responsible for obtaining any needed copyright permissions. I have obtained needed written permission statement(s) from the owner(s) of each third-party copyrighted matter to be included in my work, allowing electronic distribution (if such use is not permitted by the fair use doctrine) which will be submitted to UKnowledge as Additional File.

I hereby grant to The University of Kentucky and its agents the irrevocable, non-exclusive, and royalty-free license to archive and make accessible my work in whole or in part in all forms of media, now or hereafter known. I agree that the document mentioned above may be made available immediately for worldwide access unless an embargo applies.

I retain all other ownership rights to the copyright of my work. I also retain the right to use in future works (such as articles or books) all or part of my work. I understand that I am free to register the copyright to my work.

REVIEW, APPROVAL AND ACCEPTANCE

The document mentioned above has been reviewed and accepted by the student's advisor, on behalf of the advisory committee, and by the Director of Graduate Studies (DGS), on behalf of the program; we verify that this is the final, approved version of the student's thesis including all changes required by the advisory committee. The undersigned agree to abide by the statements above.

Weston C. Johnson, Student

Dr. Arthur Radun, Major Professor

Dr. Zhi Chen, Director of Graduate Studies

2011

DESIGN AND ANALYSIS OF MACRO SWITCHED IMPEDANCE MOTORS

Weston C. Johnson
University of Kentucky, weston@clutejohnson.com

STUDENT AGREEMENT:

I represent that my thesis or dissertation and abstract are my original work. Proper attribution has been given to all outside sources. I understand that I am solely responsible for obtaining any needed copyright permissions. I have obtained and attached hereto needed written permission statement(s) from the owner(s) of each third-party copyrighted matter to be included in my work, allowing electronic distribution (if such use is not permitted by the fair use doctrine).

I hereby grant to The University of Kentucky and its agents the irrevocable, non-exclusive, and royalty-free license to archive and make accessible my work in whole or in part in all forms of media, now or hereafter known. I agree that the document mentioned above may be made available immediately for worldwide access unless a preapproved embargo applies. I retain all other ownership rights to the copyright of my work. I also retain the right to use in future works (such as articles or books) all or part of my work. I understand that I am free to register the copyright to my work.

REVIEW, APPROVAL AND ACCEPTANCE

The document mentioned above has been reviewed and accepted by the student's advisor, on behalf of the advisory committee, and by the Director of Graduate Studies (DGS), on behalf of the program; we verify that this is the final, approved version of the student's dissertation including all changes required by the advisory committee. The undersigned agree to abide by the statements above.

Weston C. Johnson, Student

Dr. Arthur Radun, Major Professor

Dr. Zhi Chen, Director of Graduate Studies

DESIGN AND ANALYSIS OF MACRO SWITCHED IMPEDANCE MOTORS

DISSERTATION

A dissertation submitted in partial fulfillment of the requirements for the degree of Doctor of Philosophy in the College of Engineering at the University of Kentucky

By

Weston C. Johnson

Co-Directors: Dr Arthur Radun, Professor of Electrical Engineering

and Dr Kevin Donohue, Professor of Electrical Engineering

Lexington, Kentucky

ABSTRACT OF DISSERTATION

DESIGN AND ANALYSIS OF MACRO SWITCHED IMPEDANCE MOTORS

For present day global economies energy use is the single most important criteria determining a nation's wealth and sustainability. The global energy needs are met primarily by fossil fuels which are of finite supply. One means to extend the life span of the fossil fuel reserves has been to improve the efficiency of existing systems including generation, storage, usage etc., as a means of conservation. This dissertation investigates a motor technology that promises to complement existing conservation techniques.

Given advances in high voltage power semiconductors, manufacturing techniques and materials research this dissertation evaluates the potential of the switched impedance motor (SIM), a type of electrostatic motor (ESM), as an efficient alternative to induction machines. Starting with a broad look at how force can be created using electrical means, this dissertation reviews the contributions of prior art, details their inhibitors and develops analytic expressions that allow these inhibitors to be overcome. Using these analytic expressions as design tools allows future SIM designers to realize this motor topology's potential as a highly efficient machine and a global tool for energy conservation.

Keywords: electrostatic, switched impedance, capacitive motor, electret, breakdown mitigation

Weston Johnson

Date

DESIGN AND ANALYSIS OF SWITCHED IMPEDANCE MOTORS

By

Weston C. Johnson

Dr Arthur Radun

Dr Kevin Donohue

Dr Zhi Chen

Date

Table of Contents

List of Tables

List of Figures

Chapter 1 Introduction

For present day global economies energy use is the single most important criteria determining a nation's wealth and sustainability. At present, global energy needs are met primarily by fossil fuels which are of finite supply. One means to extend the life span of the fossil fuel reserves has been to improve the efficiency of existing systems including generation, storage, usage etc., as a means of conservation. This is an across-the-board global effort affecting all aspects of common life from railway locomotives, jet aircraft, automobiles and common household devices. These have all seen improvements in overall efficiency as a means to reduce operating costs as energy prices continue to climb. However, efficiency improvements are not limited to devices. In the US, many states now give tax rebates or energy credits for 'green' energy consumption prompting modern buildings to invest in new energy technologies such as solar or geothermal. The federal government has also implemented policy and programs to assist citizens in purchasing hybrid-vehicles in an effort to reduce fuel consumption and increase overall vehicle efficiency.

This dissertation investigates a motor technology that promises to complement existing conservation techniques. Given advances in high voltage power semiconductors and materials research this dissertation evaluates the potential of the switched impedance motor (SIM), which is a type of electrostatic motor (ESM) as an efficient alternative to induction machines. This dissertation has the following four goals:

1. Development of a logical design methodology for the SIM. This includes obtaining general sizing constraints for performance prediction.
2. Design and construction of a SIM. Obtain static performance data to validate design methodology and sizing parameters of part 1.
3. Using the constructed SIM of part 2, simulate its dynamic characteristics.
4. Determine the semiconductor technology properties to make the SIM feasible.

1.1 Energy Research Background

Globally, the research investment into new and novel methods for energy generation and consumption to achieve improved sustainability has been staggering. The topics of research are vast, from new prepackaged nuclear power plants, to novel fluorescent lighting, to improved solar cell technologies now reported to be at or around 41% efficient[1], to novel lightweight

materials and many other examples. This energy research includes industrial and federal government programs. In fact the US Department of Energy has an ongoing program, termed *Energy Star*, which is designed to promote and educate the public and industry about the benefits of using devices with improved efficiencies. For US industry, electric motors consume roughly 70% of all electrical power used in manufacturing[2]. Thus, even a marginal improvement in motor efficiency, if adopted across industry, would result in significant reduction of power demand and thus fossil fuel demand.

In an effort to reduce electric power requirements, the majority of which are used for electromechanical energy conversions (i.e. electric pumps, fans, conveyors, and locomotion) a review of the methods by which electrical forces are generated (mechanical) has been accomplished to achieve an overview of electromechanical technologies. Comparison of the various electromechanical energy conversion technologies, was done using a force density metric to insure equality and generality. This force density metric was calculated assuming only that existing materials and practical electrical energy sources are utilized for comparison.

1.2 Electrical Methods of Force Generation

At present, industry primarily employs devices based upon magnetic field forces. However, it is not commonly known 'why' this is so, or what other force means may be applicable or even superior for a given application despite multiple electromechanical force production methods existing. Thus, a review of the major methods of electromechanical force production is productive to gain perspective of the various methods. To insure simplicity without losing accuracy, this force method review provides a relative comparison of the electromechanical stress (force per unit area) that each method can produce.

Useful electromechanical force production can be categorized as being produced by, magnetic fields, electric fields, and electromagnetic fields. These categories coincide with the approximations used to solve Mawell's equations for the magnetic and electric fields. The magnetic field and electric field categories coincide to the analysis approximations to the general electromagnetic field case. These approximations are valid for frequencies whose wavelengths are much larger than the dimensions of the apparatus where they are to work. However, when the wavelength of the frequencies used within an apparatus begins to approach the dimensions of the apparatus, neither the magnetic field nor electric field approximations

can be used. In this case, Maxwell's equations for the electromagnetic fields in their entirety must be solved.

Figure 1 shows one way to further classify electromechanical force production methods. It defines the primary field mechanism typically applied to lumped parameter systems and under this, lists continuum systems in this same category. Thus, magnetic field force producing systems where the forces act on a rigid body such as motors and solenoids are lumped parameter systems are categorized in this same family with hybrid or continuum systems that include magnetohydrodymanic (fluid) and magnetostrictive (elastic) force systems.

$$\vec{F} = q\left[\vec{E} + v \times \vec{B}\right] = m\vec{a} \quad \textbf{(1)}$$

Electromechanical force production, based upon electromagnetic, magnetic and electric fields, is governed fundamentally by Equation (1), the Lorentz Force Equation. In (1), *q* is the charge of the particle (electron or ion), *E* is the electric field intensity, *v* is the particle velocity, *B* is the magnetic field density, *m* is the particle mass, and *a* is the particle acceleration. At a fundamental level the forces in lumped parameter or continuum electromechanical systems are acting upon charged particles (electrons, ions) that have mass and are accelerated by the applied field.

There are numerous continuum electromechanical systems, the majority of which are some variation of those listed in Figure 1. For example, Hall Effect Thrusters and Field Effect Electric Propulsion (FEEP) are subcategories of ion wind or electro- hydrodynamics.[3]

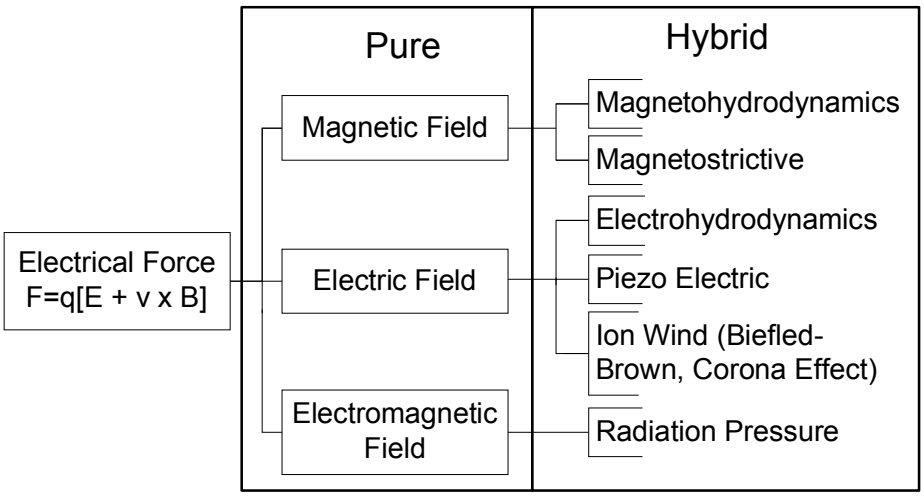

Figure 1 Electric Force Types

The Lorentz Force Equation describes the force from electric and magnetic sources acting upon a single charge. The Lorentz Equation can be expanded to determine the total force that exists per unit volume and is shown in (2), the Minkowski force Equation.

$$\vec{F} = \nabla \cdot \left[\left(\varepsilon \overrightarrow{E_i E_j} - \frac{1}{2}E^2\right) + \left(\varepsilon \overrightarrow{B_i B_j} - \frac{1}{2}B^2\right)\right] - \varepsilon \frac{\partial}{\partial t}(\vec{E} \times \overrightarrow{B}) = \nabla \cdot \prod - \frac{\partial}{\partial t}(\vec{D} \times \vec{B}) \qquad (2)$$

"A tensor whose divergence yields a force per unit volume is regarded as a stress tensor."[3] Therefore, the terms of $\prod$ in Equation (2) are known as the electromagnetic stress tensor or Maxwell's stress tensor. (A derivation of Equation (2) is given in Appendix A.) An assumption of (2) is that permeability, μ and permittivity, ε are constant and do not vary within the material. If these properties do change, with density due to a compression, then the material is said to be electro- or magnetostrictive. This property is not considered in here although it may offer potential uses that have yet to be exploited.

1.2.1 Magnetic Forces

In magnetic applications, traditional or hybrid, it is assumed that the electric field, *E*, of Equation (1) is zero or negligible. Magnetic forces are currently the most common means of generating electromechanical forces of any listed in Figure 1 and its force has been called 'heavy' as it utilizes dense materials (iron, copper etc.) to guide the field and produce its force.

Magnetic force is produced through the interaction of magnetic fields and currents in conductors or molecular or atomic currents in magnetic materials. Through variations of the magnetic field, linear and most commonly, rotational motion, can be achieved. The magnetic force per unit area is limited primarily by the amount of magnetic field available for an application as shown below in (3).

$$\frac{F_{Mag}}{A} = \frac{1}{2}\frac{B^2}{\mu_0} = \frac{1}{2}\mu_0 H^2 \approx 16 * 10^5 \frac{N}{m^2} \approx 232 \frac{lb}{in^2} \qquad (3)$$

The maximum *B* field attainable before saturation begins is 2T in CoFeV (used in aerospace applications) although 1.2T and 1.6T (in SiFe) are more common in commercial applications.

1.2.2 Electrostatic Forces

While magnetic based electro-mechanical forces may be the most widely utilized forces, electrostatic (ES) forces were the first to be discovered. Although the utility of ES systems were initially dismissed, as will be discussed later, the area has seen significant research recently at the micro scale and known broadly as Micro Electromechanical Systems (MEMS).

The origin of electrostatic (ES) force is the static charge. In electrostatic (ES) applications, lumped parameter or continuum, it is assumed that the magnetic field, *B*, of (1) is zero or negligible. While useful magnetic fields are limited by the permeability of a material, ES forces are limited by the electrical breakdown of its medium, generally air. The Paschen curve in Figure 2 gives the breakdown voltage of different gasses versus the product of the air gap and pressure. The electrical breakdown of air is important to ES electromechanical devices because they require a gap to enable the motion of its various pieces.

Considering air as the gap medium at 1atm allows a maximum electric field of about 30kV/cm to be created before breakdown and arcing occurs in air. This results in a force per unit area value of about 5.8*m*psi as shown in (4). Using industry preferred gaping, 254µm (10mil) and 25.4µm (1mil) gaps, both at 1 atmosphere results in 30*m*psi and 0.15psi respectively, both significantly lower than the magnetic case.

$$\frac{F_{ES}}{A} = \frac{1}{2}\frac{D^2}{\varepsilon_0} = \frac{1}{2}\varepsilon_0 E^2 \approx 40\frac{N}{m^2} \approx 58 * 10^{-4}\frac{lb}{in^2} \quad \textbf{(4)}$$

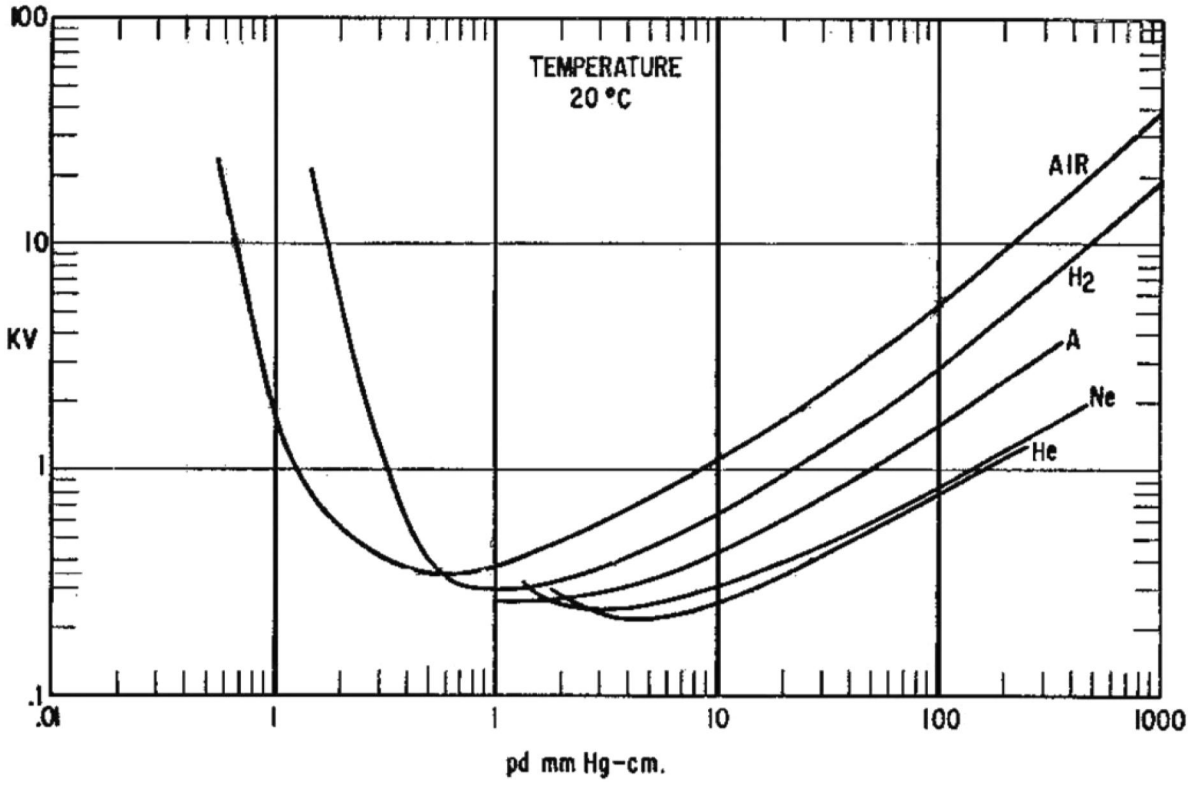

Figure 2 Paschen Curves

The left half of the Paschen curve shows a result that may not be intuitive at first glance. This portion of the curve indicates that for very small products of gap and pressure the dielectric strength of the gap medium actually increases. This is due to the small number of electric breakdown initiating ions and the small number of ionizing collisions that these ions can undergo. For this reason ES machines are competitive at small dimensions, characteristic of micro-machinery, MEMS or otherwise, as mentioned previously. The right-half of the Paschen curve, with large pressure and gap product, is typically utilized when designing macro-scaled machinery. When in this right-half region the task of ES force utilization has been very difficult due to the high voltages needed to produce a field and thus a force of economic value. Equation (4) shows that a high electric field is required for large forces, thus the breakdown electric field determines the maximum force. $V = Ed$ explains why a small *d* (gap) is needed to obtain a small voltage once the maximum electric field has been achieved.

Figure 3 and Figure 4 show the electric field and voltage versus plate spacing at 1 atmosphere. At an air gap of 254µm (10mil) E_{max}= $6.5*10^{6V}/_{m}$=$65k^{V}/_{cm}$, resulting in a voltage equal to V= 1,600V. At an air gap of 25.4 µm (1mil) E_{max} = $15*10^{6\ V}/_{m}$ = $150k^{V}/_{cm}$, and results in a voltage of V=400V. Figure 5 shows the maximum achievable Maxwell stress (in psi) versus plate spacing at 1 atmosphere.

If new gas dielectrics were available and/or means to control the mechanical vibrations such that micro air-gaps are reliable during operation, then economic force production of ES motors would then have significant advantages over their EM counterparts. ES motors do not require iron or copper windings nor do they require the yoke region necessary for a magnetic machine's operation. The yoke of an ES machine is not needed because an electric circuit does not have to be completed unlike in a magnetic circuit of a magnetic machine. A magnetic machine requires a closed circuit because the divergence of B is zero while an electric field machine does not require a closed circuit since the divergence of D is not zero. Thus, ES machines may be fabricated from less material, resulting in lighter machines.

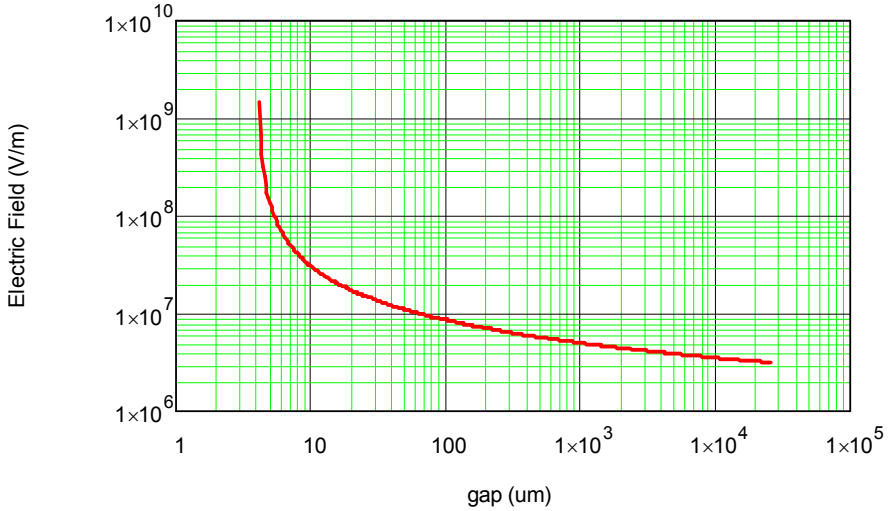

Figure 3 Electric Field vs Plate Spacing

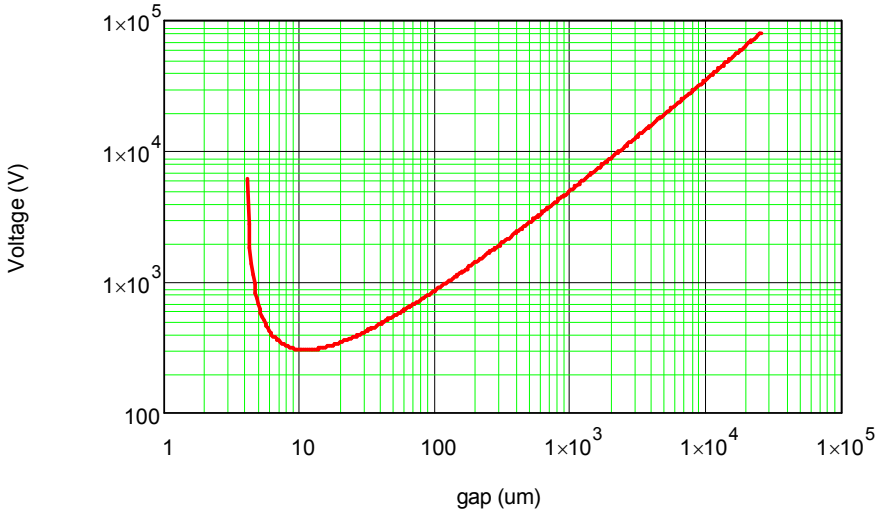

Figure 4 Voltage vs Plate Spacing

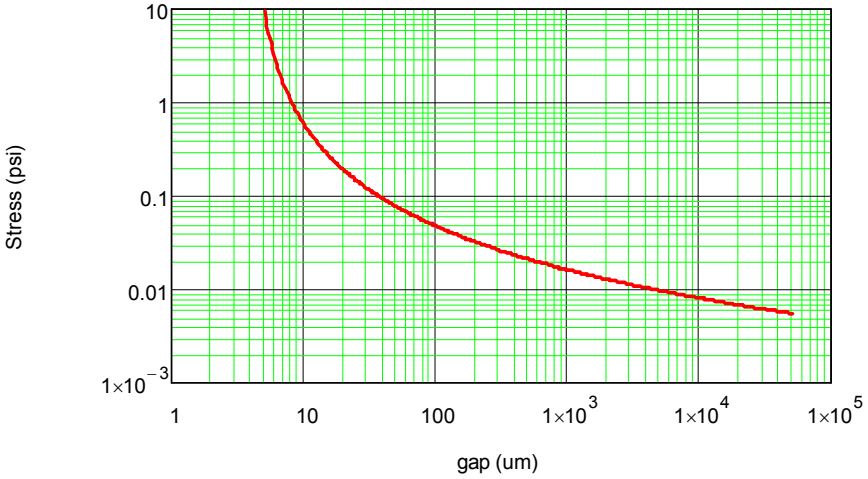

Figure 5 Maximum Maxwell Stress vs Plate Spacing

1.2.3 Radiation Pressure

If viewed as a particle, then an EM field propagates via traveling photons that have momentum. Radiation pressure from photons was first predicted by Maxwell although it was not until Lebedev in 1910 that the effect was observed and measured[4].

$$E = f * h \tag{5}$$

$$\rho = \frac{E}{c} \tag{6}$$

$$P = \frac{\vec{S}}{c} \approx \frac{1\frac{kW}{m^2}}{3 * 10^8 \frac{m}{s}} \approx 3\frac{\mu W * s}{m^3} \tag{7}$$

$$\frac{F_{Press}}{A} = P \approx 3\frac{\mu N}{m^2} \approx 5 * 10^{-11}\frac{lb}{in^2} \tag{8}$$

In (5), E is the total energy of a photon, f is the frequency of that photon and *h* is Planck's constant. In (6), ρ is the particle momentum, E is the total energy imparted to the surface by the photon particle and *c* is speed of light. The pressure *P* created by the traveling wave is given by (7) where *S* is the Poynting vector that gives power per unit area. The product of the pressure and the impact surface area gives the resulting force, F=PA, as shown in (8). This equation, has been computed with the assumption that 1kW per square meter is available in a standard atmosphere resulting in a stress of 50pico-psi.

While impractical for most earth bound applications, solar sails are based upon this force because non-terrestrial applications allow for increased power per unit area as well as reduced external forces such as aerodynamic drag and gravity that could easily exceed the radiation stress.

1.2.4 Piezoelectric

For force applications, this is more aptly described as the *inverse piezoelectric effect* where force is the output rather than the input[5]. This inverse effect occurs when a voltage is applied to a crystal lattice causing stress within the lattice. This voltage induced stress results in the lattice expanding or contracting, generating a usable force.

$$E = \frac{d}{\varepsilon_o \varepsilon_r} T = gT \tag{9}$$

In Equation (9) the electric field *E* induces a mechanical stress *T* related by the piezo-voltage coefficient *g*[6]. A stress value for piezoelectric forces can be determined from (10).

$$T = \frac{F_{Piezo}}{A} = \frac{\varepsilon_0 \varepsilon_r V}{dl} = \frac{1250\varepsilon_0 * 700kV}{480 * 10^{-12}\frac{m}{V} * 1m} \approx 16\frac{MN}{in^2} \approx 2340\frac{lb}{in^2} \quad \textbf{(10)}$$

In (10), *d* is the piezoelectric charge coefficient which is unique to each piezo material and *l* is the length between the voltage nodes[6]. The piezo stress value computed in (10) is for 402 Lead Zirconate Titanate (PZT)[7].

1.2.5 Ion Wind (Biefeld-Brown or Corona Effect)

Ionization of a gas such as air, as described by the Paschen curve (Figure 2) can be used to generate ions, the acceleration of which can produce a reactive force by Newton's law on the apparatus producing and accelerating the ions. This force method is governed by $\vec{F} = m\vec{a}$ where it is the mass of the charged ions accelerated by an electrostatic field that creates force (lift or thrust). This method is limited by the ion current density for a given gap distance which thus limits the force density.

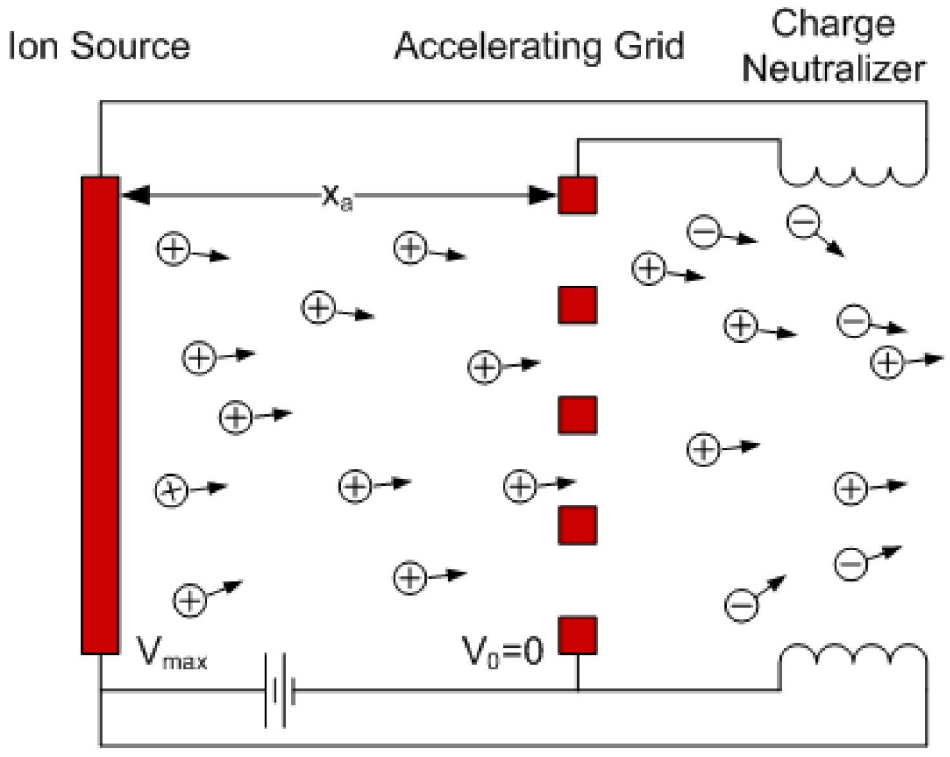

Figure 6 Ion Thruster Generalized Schematic

$$v(x) = \sqrt{\frac{2q(V_{max} - V_0)}{m}} \tag{11}$$

$$\frac{dV}{dx} = 2\sqrt{\frac{J}{\varepsilon_0}} * \left(\sqrt[4]{\frac{m(V_{max} - V_0)}{2q}}\right) \tag{12}$$

$$E = -\frac{dV}{dx} = \frac{V_{max}}{x_{max}} \tag{13}$$

$$\frac{F}{A} = \frac{1}{2}\varepsilon_0 E^2 \approx 440\frac{N}{m^2} \approx 0.064\frac{lb}{in^2} \tag{14}$$

Equations (11) through (14) estimate the stress due to the ion wind assuming one-dimensional flow and a fixed electrode spacing and voltage. This results in a force density that is independent of the charge-to-mass ratio of the ions.[8] In Equations (11) through (14) *m* is the ion mass, *x* is the gap distance, and *q* is the ion charge. Equation (11) computes a single ion's velocity by equating the kinetic energy and the work done moving a charge *q* through a potential difference V-V_O. In a hard vacuum, such as space where an ion thruster may be used, an electric field strength of $10^7\frac{V}{M}$ has been the practical limit.[8] This limit on the electric field prevents further force density from being achieved. It is worth noting, that the limited factor for this force method is the same as with ES methods, a limit of the practical field strength. Again, if a novel dielectric were developed to allow increased voltages, increased force densities could be developed. Appendix B gives further details to the derivation.

1.2.6 Force Comparison Conclusion

Several electromechanical force sources have been compared using estimates of the maximum electromechanical stress in an effort to gage their usefulness. The comparison, given in Table 1 shows each of the computed maximum electromechanical stress for the electrical-mechanical systems considered. The sole assumption of the computation is that the computations have been made based upon upper end yet feasible field values. As seen from the comparison the traditional EM force method does not have the largest stress value, piezoelectric methods do. Thus, there may be applications where piezo force methods would be much better suited to the job.

Table 1 PSI Value Comparison

Force Type	SI	PSI
Radiation Press.	3E-6	5E-11
Ion Wind	440	0.064
ES	1000	0.15
Magnetic	16E+5	232
Piezo	16E+6	2340

1.3 Chapter 1 Summary

While the maximum electromechanical stress has been determined for each method, each method has its own unique design constraints, which must be observed for efficient results. The broad, general methods by which various electromechanical forces may be developed have been reviewed and compared using an electromechanical stress metric. This review showed that piezoelectric methods provide the largest stress. However, this method will have difficulty obtaining useful rotational motion due to its small achievable displacement and crystal expansion-contraction cycle time.

Electrostatic force systems, though they have lower electromechanical stress than piezo or magnetic force systems, could have system advantages in some applications due to their lower losses from lower currents and the potentially lower density materials used in their fabrication.

The challenge for developing competitive ES machines at macro scales is in achieving and operating with high electric fields while minimizing terminal voltage. Traditionally this has been achieved with MEMS technology, but could be possible using advanced dielectric coatings and/or advanced high permittivity gasses such that the Paschen curve for the gap medium is shifted in such a way that a larger gap can achieve a useful field strength while preventing field breakdown.

Chapter 1 showed that an ESM has the potential to exceed induction machines for small gaps. However, prior to analyzing a motor and developing a specific design, a broad review of the field of electrostatic motors would be beneficial to those who are unfamiliar with the area. For this reason, a summary of ESMs is given.

2.1 Topologies

Electrostatic motors (ESMs) are a class of electromechanical machine that produces useful mechanical work due to the employment of an electric field. ESMs, as one would expect, have various sub-categories or topologies each employing a unique characteristic of the electric field and static charges. Figure 7 below shows various ESM topologies.

ESM operations are performed by purposefully placing charges, which via Coulombic forces are then attracted or repelled to a new location. Once in location, the charge is redistributed purposefully to again create attractive or repulsive forces for continuous operation. The various categories of ESMs only differ in their means of charge placement, containment, and replacement which is analogous to magnetic machines. ESMs can be characterized by their ability to "accept charge" for a given applied voltage, rather than "accept magnetic flux" $\vec{B}$ for a given current. For this reason, ESMs are capacitance machines rather than inductive. To help clarify ESM operation, a few of the topologies are summarized.

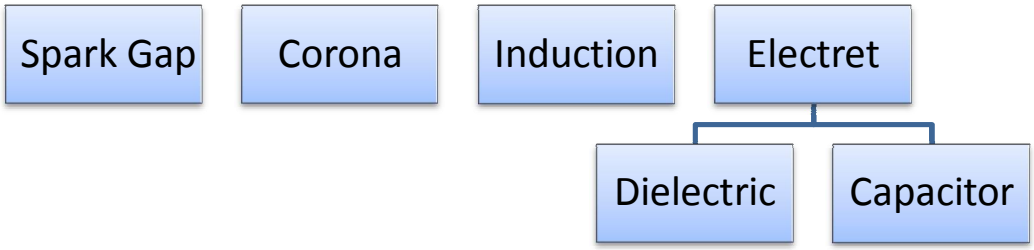

Figure 7 ESM Topologies

2.1.1 Spark Gap or Brush

Benjamin Franklin in 1748 is the first person to be recorded as producing an ESM, and even one of measurable power, about 0.1W.[9] While his motor was more of an intellectual curiosity rather than a device of utility, it does begin the history of ESMs.

As shown in Figure 8, the spark gap motor utilizes a voltage source to provide charge to an isolated conductor. Once charge is placed, the charge itself begins to repel from the dipole source, as they are of the same polarity. If a charge of sufficient value is able to produce a repulsive force to overcome any mechanical resistance, a net torque will be generated and rotation will begin. At another location, a dipole of opposite polarity neutralizes the original charge and places a new change of opposite polarity on the conductor, thus allowing the process to continue. This motor typically needs a small push, to be started.

2.1.2 Corona Motors

Rather than charging a conductor, charge may be placed on an insulator to achieve a result similar to the spark gap motor. If a voltage is increased beyond the surrounding medium's breakdown voltage (V_{Bk}), then arcing will occur. Just prior to breakdown, the surrounding medium may begin to ionize, a process where charge is 'sprayed' into the medium, collectively known as corona. A corona motor utilizes this ionization mechanism to purposefully spray charge, with sharp needles or comb like appendages, onto an insulator. (The sharp edges assist in developing *corona* from low voltage sources, as the electric field at an edge is vastly higher than its planar surroundings.) However, once the charge is placed onto the insulator where it is unable to redistribute, it will repel itself from its source, because the charge being placed is of the same polarity as its source. Similarly to the spark gap motor, charge is continuously placed until a sufficient repulsion force exists to turn the rotor (or arcing occurs through another path). To allow for continual motion, charge of opposite polarity is placed onto the rotor (or stator) to neutralize the original charge and to create a new polar repulsion act. Figure 9 illustrates the process of torque development for the corona motor.

The operational characteristics of the corona motor are closely related to the environment in which it operates. Temperature, humidity and operating time all affect its characteristics.[10]

As an interesting side note, "[t]he corona motor is the converse of the Van de Graff generator. In both cases charge is the active medium, but while in the Van de Graff generator it

is transported against an electric field to supply voltage, in the motor it is allowed to move with the field in order to supply torque."[11]

2.1.3 Induction or Hysteresis

An ES induction motor operates upon the principle that "polarization of a dielectric in a variable electric field lags behind the field inducing the polarization or, more specifically, that a dielectric placed into a rotating electric field experiences a force acting on the induced polarization charges causing the dielectric to follow the rotation of the field" [9]. As the dielectric polarization is 'induced' by the external electric field, it is termed an electrostatic induction motor.

2.1.3.1 Hidetaro Ho

In 1901 Hidetaro Ho published an article in the Japan Issue of the Journal of the Institution of Electrical Engineers describes his ES hysteresis motor. The article describes a simple ESM motor (which was a variation of one by Riccardo Aro, a student of Galileo Ferraris and contemporary of Nicola Tesla) and gives a theoretical analysis for the hysteresis effect. His analysis also derives the proper resistance, for a given rotating electric field, to operate successfully in hysteresis. Ho states that the hysteresis EMS operates under the following principle:

> *"[A]s the electric field rotates, each pair of the sectors which are diametrically opposite to each other is subjected to an alternating electromotive force which would produce, if the sectors be absolutely insulated from each other, induced charges in these pieces of in foil, which appear and disappear at the same time with the potential difference impressed by the stator and therefore no torque can be developed. If, on the other hand, the sectors be connected up with small resistance, a very considerable amount of induced charges which are equal and opposite would appear on the two sectors of a pair, and a considerable attraction between the quadrant and the discs is the consequence, but no tangential pull can be obtained since the induced charges appear and disappear at the same time as the potential difference of the stator. If, however, the resistance have a certain proper value, we may expect such a condition that the flow of charge in the process of induction and neutralization is retarded by the resistance and the charge of a sector lags behind the rotating potential difference of the stator, in which case certain torque must be obtained in the direction of the rotating of field."*[12]

Ho provides a thorough analytical analysis of this motor and concludes his paper by comparing his induction ESM equations with those of magnetic induction machines. His analysis showed that the two topologies are remarkably similar.

2.1.4 Electret

An electret is a permanently polarized dielectric and is the analogous electric version of the permanent magnet. Like the corona motor, isolating the rotor to maintain continuous polarization is difficult without environmental isolation. However, should this be achieved this topology may be utilized and controlled similar to any permanent magnet or stepper motor.[9]

2.1.5 Variable Capacitance

The capacitor topology, the subject of this dissertation, is constituted by a variable overlap of charged conductors which are insulated from each other constituting a variable capacitor. Capacitance, defined as ratio of charge to voltage, is a characterizing parameter of an electro-static system and describes the ability of a system to store charge for a given applied voltage and is defined in (15).

$$C \equiv \frac{Q}{V} = \frac{\int_A E \cdot da}{\int_{L_-}^{L_+} E \cdot dl} = \frac{\varepsilon A}{L} \tag{15}$$

In essence, this topology constitutes a multi-electrode capacitor. The variable capacitor motor can operate in both synchronous and asynchronous modes, as well as from AC and DC sources[9], and thus embodies a very flexible topology. Figure 11 shows a simple, force generating, multi-electrode capacitor wherein force is developed as a result of Coulombic forces, the force developed between two static charges. In Figure 11, the rotor is held stationary while Phase B switch (Sw_B) is closed, however, a force may be generated to the left or right should Sw_A or Sw_C respectively, be closed.

2.1.5.1 Switched Impedance Motor

The ES motor is one of high voltage and low current, thus, a motor of high impedance. For this reason, an ESM of linear capacitor topology, with a multitude of electrodes to switch between capacitors (phases) to insure continuous motion, may be termed a *switched impedance motor* or SIM. The following chapters provide an analysis this topology.

2.1.5.2 John Trump – Synchronous Impedance Motor

In 1933, John Trump, of the Massachusetts Institute of Technology, completed a PhD dissertation on electrostatic motors in a vacuum. (The present work is loosely based upon his dissertation.) In brief, Trump designed and constructed an electrostatic motor (ESM) for synchronous operation. The ESM motor by Trump was a 200W, 75kV motor and was operated

using a light vacuum for the air gap dielectric. In operation the device rotated continuously at 2000rpm. Trump summarized the future of his work with the following statement:

> *"The measured power output of the machine … indicates that power concentration comparable with that of modern alternating-current machines could be realized at once in a new design of the same physical dimensions."*[13]

> *"While exact comparison of the relative compactness of vacuum electrostatic and electromagnetic power machines must necessarily await the determination of the practical insulation limitations of high vacuum, it seems reasonable at the present time to predict that vacuum electrostatic machines are ultimately capable of greater compactness, lightness and lower cost than is now realized in modern electromagnetic machines".*[13]

While nearly 75 years has passed since Trump's ESM work, his predictions may yet come true though maintaining a vacuum with a rotating seal remains a technical challenge. Photos of the 1933 device are given for reference in Figure 12 and Figure 13.

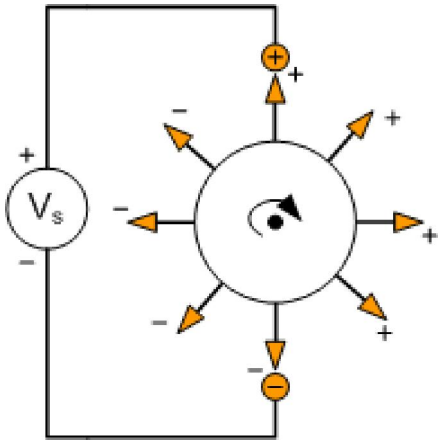

Figure 8 Spark Gap Motor

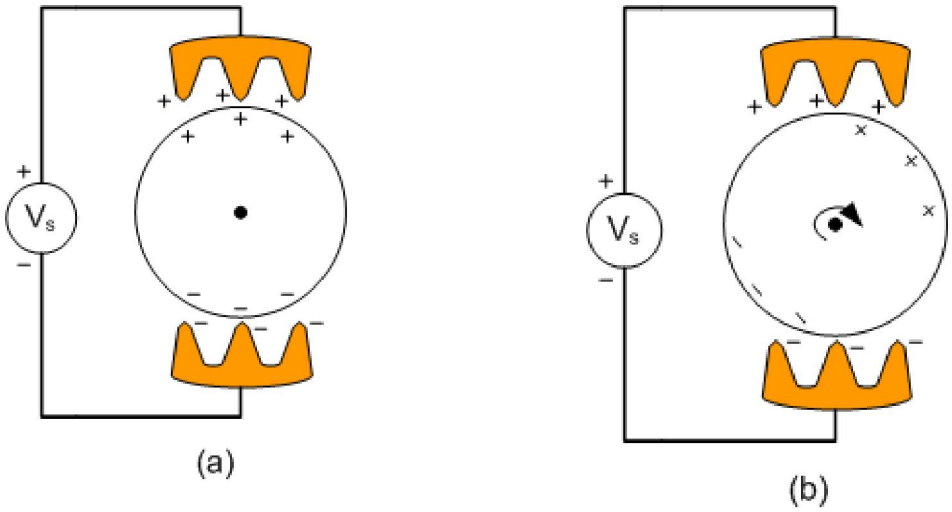

Figure 9 Corona Motor Operation

(a) Charge placement via ionization (b) Charge repels source

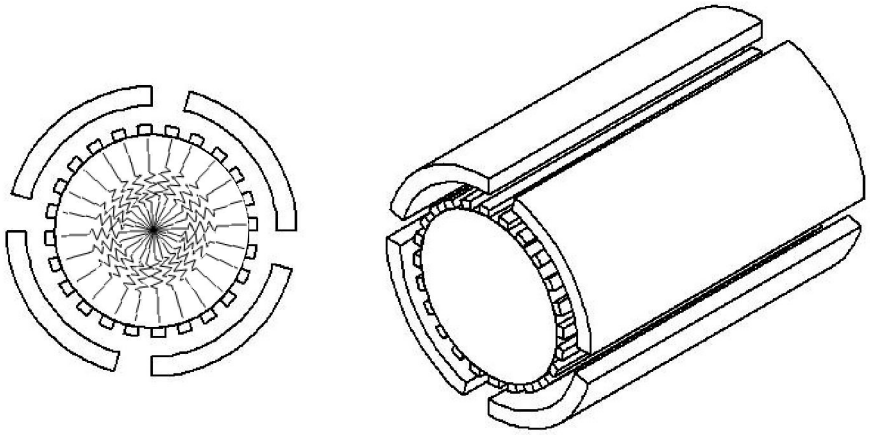

Figure 10 Ho ESM

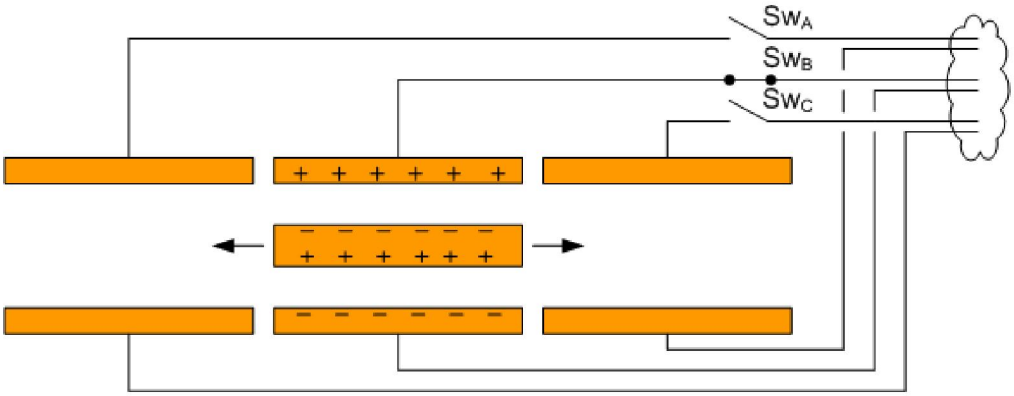

Figure 11 Force Development from ES Capacitor Motor

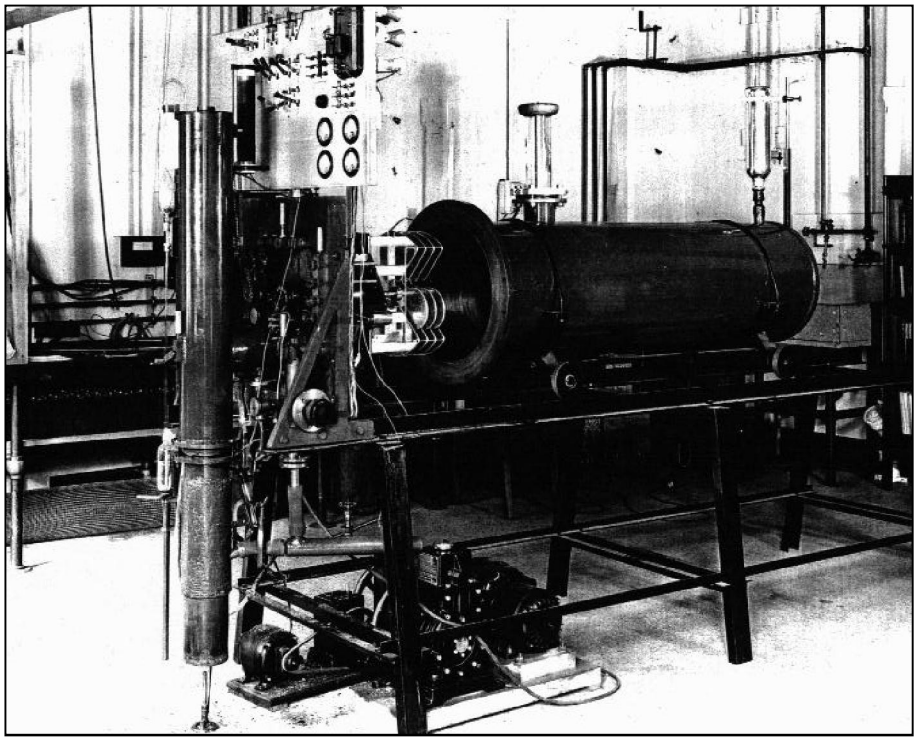

Figure 12 Trump 1933 ESM System

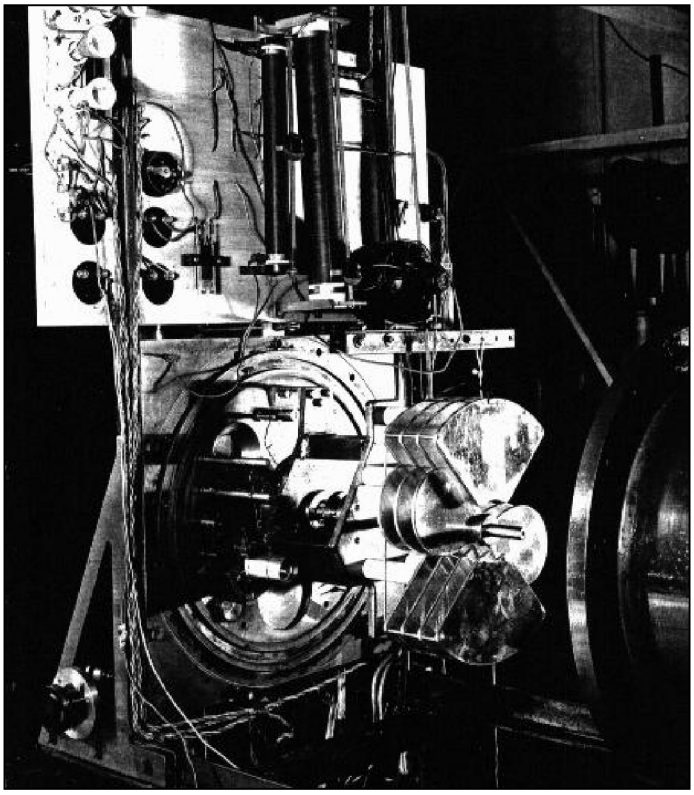

Figure 13 Trump Exposed ESM Plates

2.2 Chapter 2 Summary

ESM technology has not been adopted by industry for multiple reasons including poor material properties, poor controls, inability to develop and manage high voltage, poor knowledge of breakdown of air in the air gap and insufficient analytical tools. Ho and Trump both recognized these limitations which to some degree continue to persist even to today. Despite the long interval since the ESM conception and the contributions of both Ho and Trump the subsequent 100 years since their work has brought about many advances in all of the previously limiting areas as well as a greater need for the technology.

ESMs, and in particular ESMs using the variable capacitor topology, are flexible and efficient. Efficiency of this topology occurs because the losses of an ES machine would be significantly less, especially at low speeds, because the continuous I^2R losses of EM machines do not exist in ES machinery. I^2R losses of ES machines only exist while they are charging or discharging. Thus, the I^2R losses of ES machines are not a *continuous* time source of loss as in EM machines. In addition, ES machines to not have multiple turns of wire necessary to guide the magnetic field from current flow and losses of dielectric materials are typically much less than magnetic materials. It is the SIM capacitor topology that is the focus of this dissertation, although all topologies will benefit from the research presented herein.

A high level comparison of force density between various force generating methods was presented in Chapter 1. Based upon this analysis it was shown that an ESM could be superior to magnetic machines if a means to prevent breakdown and manage gaps measured in microns existed. In addition, mature modeling techniques to analyze the electric fields including their breakdown, capacitance generation, and the electro-mechanical coupling theory to produce useful force all need to be defined for the ESM to become the viable efficient machine that is need for continued economic growth.

Hidetaro Ho and John Trump were limited by materials, controls and analytical capabilities in the design of their ESMs. In the subsequent 100 years vast improvements in these areas, as well as in manufacturing techniques, have occurred. This chapter presents the theory and analytic techniques necessary for small *pd* product ESMs to be of use. However, breakdown of the field in the gap is difficult to define for just *any* material, or *pd* product and thus requires empiric testing of gap breakdown to know its limits and safe operating regions. Despite this requirement, development of a logical design and analysis methodology, that allows general sizing constraints to be predicted, has been defined. This design and analysis methodology is now presented for fulfillment of the first goal of this dissertation.

3.1 Design Methodology

In the design of any system clear understanding of the goal or output to be achieved is necessary. The applications goal will provide direction for the design although it must be tempered with what can be practically achieved. Finding a balance between goal ideals and that which can be realized entails trade-offs as specifics are defined, as is typical with any design. For instance, a SIM design may start with the definition of the desired torque and/or speed. Based upon this desired output torque and speed, a specific capacitance profile must be created. That profile requires structure and mechanical assemblies which must be defined to implement it. All of these must additionally meet any environmental and area or volume constraints. All of these will seldom be met upon the first design, thus an iterative design process is necessary to insure all constraints are optimized. Figure 14 and Figure 15 highlight a simple SIM design methodology that results in specifics of the gap and rotor-stator plate sizing from which capacitance profiles can be modeled for continued refinement.

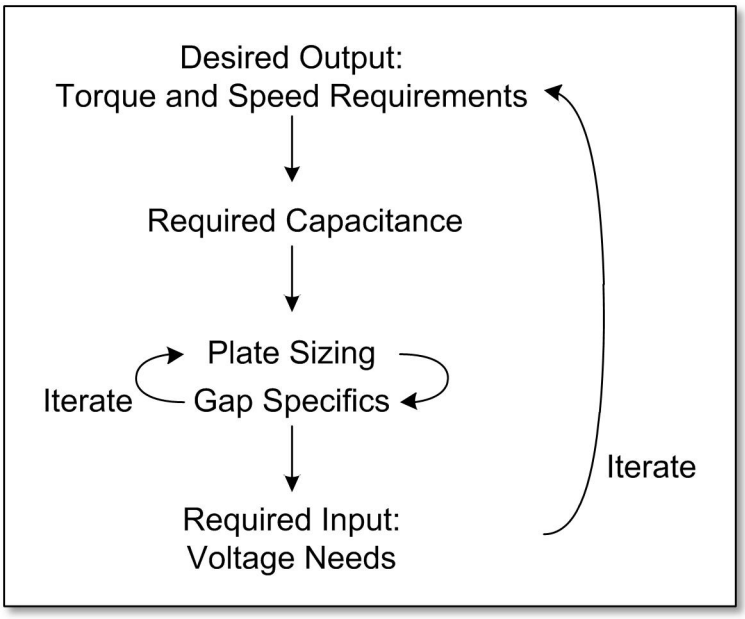

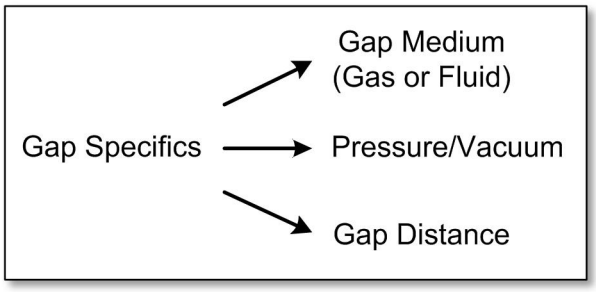

Figure 15 Specific Parameters for Gap Definition

Independent of any application design goals, analysis of the electric fields in the gap is necessary. Field analysis begins with a thorough understanding of the field breakdown mechanism and field modeling techniques.

3.2 Electric Field Breakdown

All prior known macro scale ESM work developed force based upon macro air gaps, the area on the right-hand side of the Paschen curve. While never mentioned directly in literature searches, it has been assumed that the primary reasons for this are:

1. Poor insight into breakdown mechanisms (ie. ionization and field emissions)
2. An inability to prevent breakdown for the small *pd* product operation range
3. Limited manufacturing technology to hold tolerances

John Trump in his experiments utilized large 1cm gaps with a vacuum to prevent breakdown. Other researchers simply chose to utilize lower voltages or a topology that benefited from breakdown such as the spark gap motor. To be of use to industry and society at large the SIM will need to achieve force densities at least on par with traditional magnetic machines as described in Chapter 1. Utilization of the small *pd* product area on the left-hand side of the Paschen curve, in the realm of micro air gaps and low pressure could achieve this goal. To do so, arcing, ionization and/or discharge mechanisms must be prevented or handled in a nondestructive manner. Assuming for the moment that viable options to prevent or delay breakdown were possible these options would be described generally by the Paschen curve. The Paschen curve in Figure 2 showed that one method to prevent or delay breakdown is by utilizing the left half of the curve, an area where the gap and pressure product (*pd*) are very small. By utilizing this portion of the curve the force density of an ES machine could exceed that of a magnetic.

Figure 16 compares force density between electric and magnetic fields graphically. The figure has four curves that show the relative position of (a) the electric breakdown strength at a constant 30kV/cm (3V/um) which is the commonly accepted breakdown of air and utilized in MEMS, (b) the electric force density based upon Equation (4) and the computed Paschen curve, (c) the typically attainable magnetic field of 1.2T and (d) the magnetic field of 2T that is attainable with premium performance materials. This figure shows that an air gap smaller than roughly 5µm on an ES motor could exceed that of a magnetic.

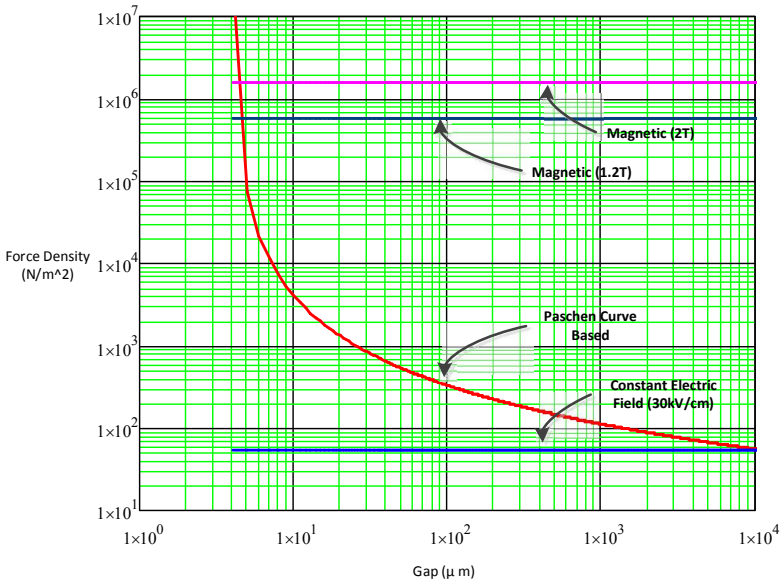

Figure 16 Force Density Comparison - Magnetic and Electric Field at 1atm

However, Paschen curves only describe breakdown of the electric field in the gap medium due to ionization and eventual avalanche process. Discharge can also occur through another mechanism known as *field emissions*. Field emissions are one reason why breakdown and sparks occur in a vacuum, which is not possible if one considers only ionization and the avalanche mechanisms used to generate Paschen curves.[14] (For gaps smaller than 2nm, an additional mechanism called *tunneling* may also occur.)

Field emissions, an effect of the *work function* of the conducting material, occur when electrons are pulled from their atomic bond across the gap to the opposite polarity source. To help illustrate the multiple mechanisms that can result in breakdown, a plot identifying their respective regions of operation is shown in Figure 17. For gaps <3μm field emission breakdown primarily exists, from approximately 3μm to ~8μm an approximately linear transitional stage exists wherein ionization is inhibited due to the gap size yet field emission exist, and above ~8μm the gap is large enough such that an avalanche process from ionization breakdown dominates.[15]

Field emissions may be understood by examining (1) further, shown again below for reference.

$$\vec{F} = q\left[\vec{E} + r \times \vec{B}\right] \quad (1)$$

Charge of a conductor is typically considered to be comprised of surface charge or freely moving charge (q_{free}) used for conduction and current processes. However, within a conductive

material, additional charged particles do exist. These internal charged particles, or bound particles (q_{B+} and q_{B-}), normally cancel, thus preventing any net charge from existing within a conductor. However, during field emission, a bound charge is pulled from its atomic bond and accelerated by the field towards the opposite polarity charge. Equation (16) shows Lorentz's Force Equation with the expansion of charge types for an electrostatic case.

$$\overrightarrow{F_{ES}} = (q_{B+} - q_{B-} + q_{free})\vec{E} \quad \textbf{(16)}$$

Determining if the breakdown mechanism was due to avalanche or field emission can be done using the Fowler-Nordheim Equation (17) which describes the current of breakdown.

$$I = aE^2 e^{\frac{-b\Phi^{3/2}}{E}} \quad \textbf{(17)}$$

"If the current is due to field emission, a plot of $1/E$ vs $\ln(I/E^2)$ should yield a straight line with a negative slope that is proportional to the work function of the metal."[14] In Equation (17), *a* and *b* are empirically determined constants and Φ is the work function value.

Independent of the breakdown mechanism, a unified analytic model for breakdown is difficult to generate as numerous mechanisms exist as previously described. For this reason, empirical models are generally utilized for small gaps where transitional breakdown phases exist.

Figure 17 shows a typical curve for a gap spacing composed of air. However, if the gap were composed of a dielectric gas or specialized coatings with high dielectric strength and work function, then fields that more closely follow the Paschen curve are possible. In addition, the utilization of high precision machining and micro coatings that can be applied in thicknesses measured in nano and mirco meters, primarily developed for the semiconductor industry could help additionally. These are methods not available to Trump, Ho or other previous researchers.

Breakdown occurs when the maximum sustainable electric filed for the environment is exceeded. Understanding how the field is distributed, through voltage drops, is key to preventing them.

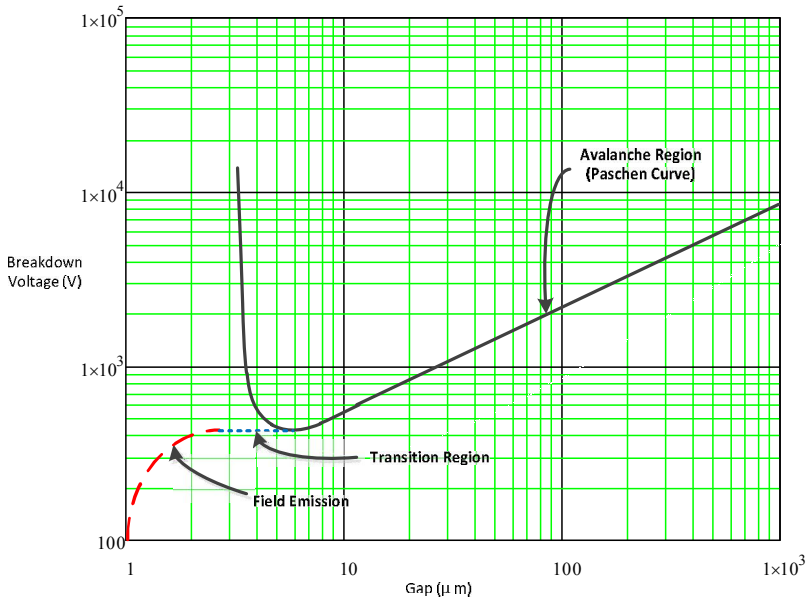

Figure 17 Modified Paschen Curve - Breakdown Mechanisms at 1atm

3.2.1 Voltage Drops

A voltage drop of the SIM will exist between two charged plates, such as the rotor and stator plates. The drop will occur across the gap and any material wherein the field exists (gap medium, insulative coatings etc) in proportion to the distance that the field line traverses through it (ie materials thickness) and their dielectric strength. An example of this relation is shown in Equation (18) and illustrated in Figure 18.

Although many options exist one coating in particular, zirconium oxide (ZrO_2) has a reported dielectric strength of 3-5MV/cm[16] which is ample to provide an insulative layer for the SIM conductive plates. To achieve the ideals of the left hand side of the Paschen curve the coating must be sufficiently small to permit enough field to pass such that a useful force can be generated. This relationship is shown in Equation (18) which states that the applied source voltage must be less than or equal to the maximum voltage breakdown of the gap and coating. Applying a voltage value above this value may result in breakdown of the coating that will result in arcing and shorting of the source.

Recognizing that the electric field cannot change instantaneously allows Equation (19) to be written and used to create Equation (23) and (24) to compute the voltage drop across the dielectric coating and air gap. Figure 18 shows the physical voltage drop relations while Figure 19 and Figure 20 show the voltage drops for ZrO2 and Kapton coatings and the respective drops in the gap for various thickness and gap spacings.

$$V_{source} \leq V_{gap\,max} + V_{coat\,max} = E_{gap\,max} d_{gap} + E_{coat\,max} d_{coat} \tag{18}$$

$$\varepsilon_{coating} E_{coating} = \varepsilon_{gap} E_{gap} \tag{19}$$

$$V_{Coating} = \left(\frac{\frac{\varepsilon_{gap} d_{coating}}{\varepsilon_{coating} d_{air}}}{1 + \frac{\varepsilon_{gap} d_{coating}}{\varepsilon_{coating} d_{air}}} \right) V_{max} \tag{20}$$

$$V_{gap} = V_{max} - V_{Coating} \tag{21}$$

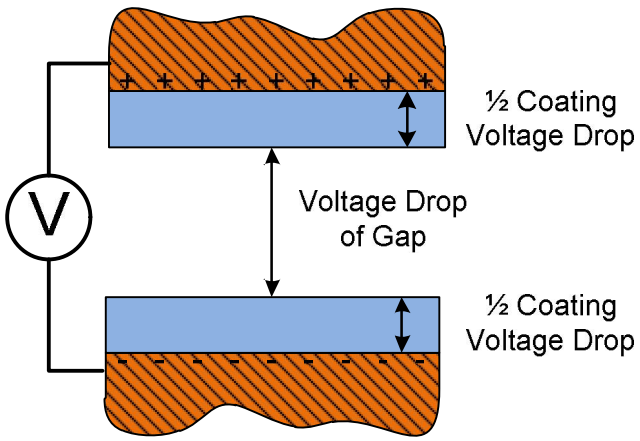

Figure 18 Voltage Drop Locations

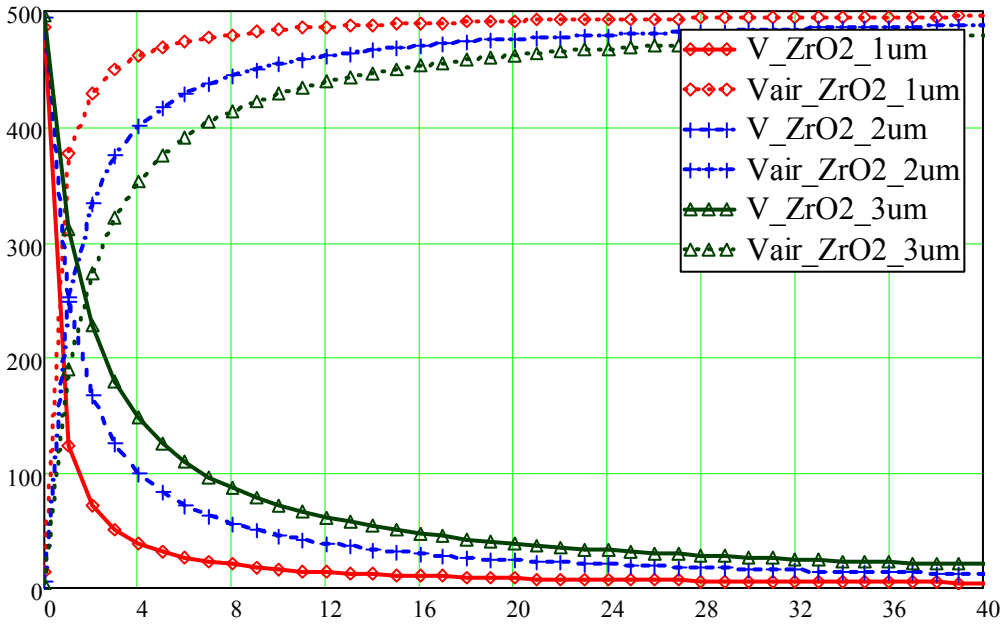

Figure 19 Voltage Drops at 1kV with 1, 3 and 5um Thick ZrO2 Coatings

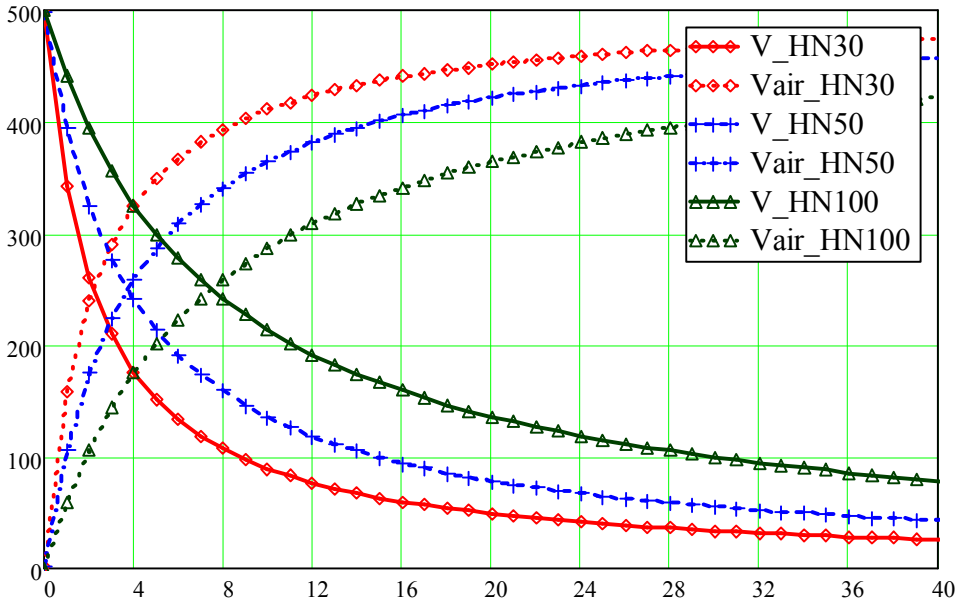

Figure 20 Voltage Drop of one Air Gap with 1kV Applied with Various Kapton Films

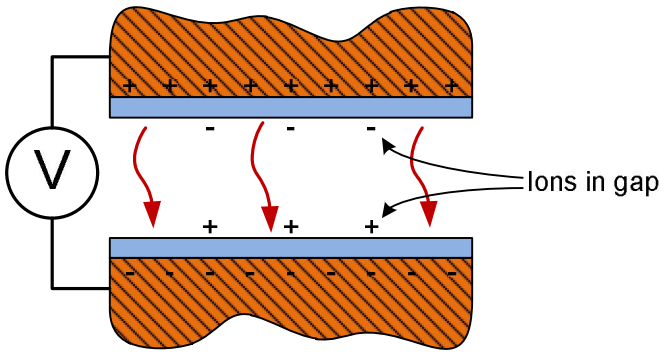

Figure 21 Gap Ions

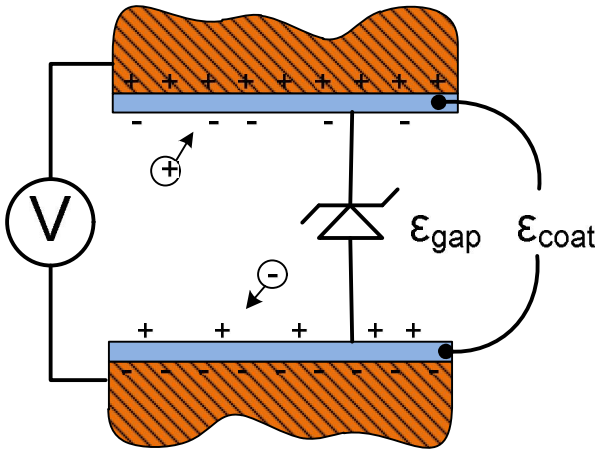

Figure 22 Zener/Avalanche Diode Model

Figure 19 and Figure 20 show the voltage drop effects of ZrO2 and Kapton dielectrics at various thicknesses according to Equations (23) and (24). The figures show that the voltage drop in the air gap increases with gap distance, as expected.

Note that the model of Figure 18 has only one air gap while an ESM will require a gap on either side of the rotor. As will be shown later, an electrically isolated rotor is preferred which, because charge on the rotor is fixed, sets the isolated rotor at a zero voltage with respect to the stators. For this reason, the voltage drops on either side of the rotor will sum to one half of the applied voltage as shown in Figure 19 and Figure 20. These figures also show that for a very small gap the voltage drop occurs mostly within the dielectric. (It will be shown in the next chapter that this inhibits an electric field from generating a useful force.)

3.2.2 Arcing in an Isolated Gap

Short duration gap arcing is possible with dielectric coatings even if the applied voltage is less than the breakdown voltage of the coating. Due to surface roughness and other material abnormalities, an electric field and voltage in excess of the gap breakdown strength may exist. This could occur via ionization of the gap that surrounds the plates. However, because the insulative properties of the coating have not broken there is no continuous source of energy to sustain an arc, thus only localized particles in the surrounding environment may provide charge.

Due to arcing which is a conductive process, the air gap may be modeled as a Zener diode, (or avalanche diode) as shown in Figure 22, with a breakdown voltage equivalent to that of the gap, about 30kV/cm for air. This model reflects the extinguishment of an arc once the charged ions are removed and their electric field (voltage) drops below the breakdown threshold.

Breakdown is described by the dielectric strength of the medium and its understanding is necessary to insure that sufficient charge can be developed on a plate to generate a useful force. With this understanding, a detailed description of the field itself can now proceed.

3.3 Analytic Modeling the Air Gap

One method to describe the electric field of the air gap of a SIM is to discretize the gap, then algebraically analyze each area. This discretized gap is depicted in Figure 23 and Figure 24 below wherein three gap regions that surround a positive and negative stator plate (S+, S-) as well as the rotor (R) are identified.

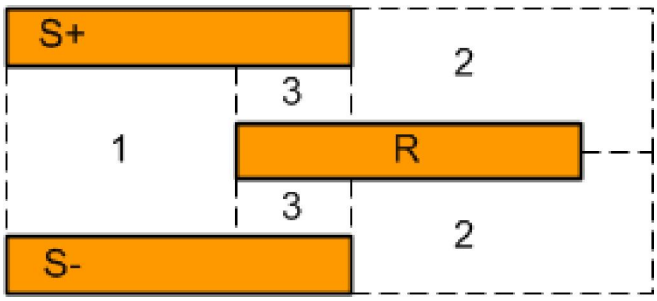

Figure 23 Air Gap Discretized Field Boundaries

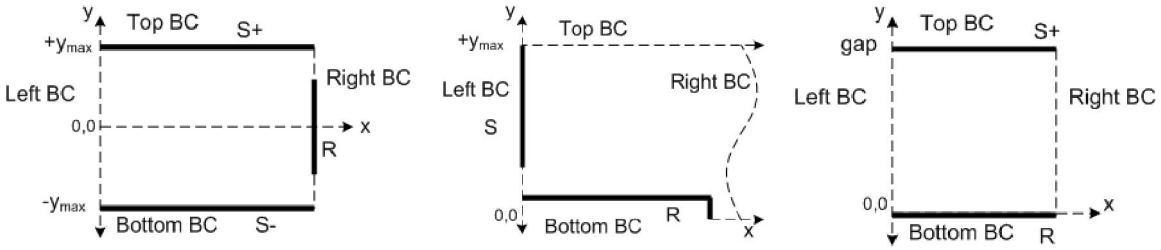

(Area 1) (Area 2) (Area 3)

Figure 24 Field Boundary Details of Air Gap

Figure 24(Area 1) details the field boundary to be solved for between the two stator plates when the rotor is unaligned. Figure 24(Area 2) details the trailing fringe field boundary between the rotor and stator plates, again while the stator and rotor plates are unaligned. Figure 24(Area 3) details the overlapped (aligned) area between the rotor and stator. It should be noted that the arrangement of Figure 23 is symmetric about the center of the rotor to help simplify a solution for the fields.

3.3.1 Area 1 – Stator Overlap

Area 1 is the open area between the two stator plates and represents a variable capacitor with large air gap. The left boundary condition (BC) of the area has been approximated as a linear voltage gradient from the negative stator plate to the positive plate. The top and bottom BCs are constants as they will be connected directly to a voltage source. The right BC and the rotor edge can be approximated using a Fourier Series (FS). The edges of the stator and rotor are assumed to be perfect conductors, which is appropriate for low frequency fields. Thus, all voltage drop of the right BC will occur in the air gaps between the rotor and stator plates. For simplicity, the rotor has been set to 0V with the two stator plates set to +/-V_{max}, a valid choice when the rotor is centered.

3.3.2 Area 2 – Trailing Edge

Area 2 is the trailing area of the rotor plate as it moves between the stator plates. Area 2 will consist of fringing flux connecting a side of a stator plate and a trailing face of the rotor plate. This area is challenging to analyze directly as knowledge of the top and right BC is not known nor easily approximated.

3.3.3 Area 3 – Primary Overlap

Area 3 is the aligned or overlapped area between the rotor and stator plate. As the air gaps are small, the left and right BC can be approximated as linear voltage gradients while the top and bottom BCs are constants.

3.4 Calculating the Fields of the Gap

Efficient design of an ESM requires knowledge of the field in the gap. Analytic solutions to these fields are one means to acquire this knowledge and dynamically design optimum SIMs. To find analytic solutions to the three regions Laplace's Equation must be solved.

3.4.1 Area 1 – Stator Overlap

Setting up the problem for this region has been accomplished by loosely following an example given by authors William H. Hayt and John A. Buck in *Engineering Electromagnetics*. Algebraic expressions for the electric field of the floating rotor SIM can be determined by utilization of Laplace's Equation, shown in (22). This equation (rather than Poisson's Equation) can be utilized because the air gap does not store charge.

$$\nabla^2 V = 0 \tag{22}$$

If the assumption is made that the voltage may be represented by two independent functions, X(x) and Y(y) (thus $V = XY$), which is to assume that field in x-direction is independent of the field in the y-direction, then Laplace's Equation may be rewritten as a combination of two independent functions.

$$\nabla^2 V = \frac{\partial^2 (XY)}{\partial X^2} + \frac{\partial^2 (XY)}{\partial Y^2} = 0 \tag{23}$$

Because of their independence, rearranging the function allows a constant to be determined.

$$\frac{1}{X}\frac{\partial^2 X}{\partial X^2} = -\frac{1}{Y}\frac{\partial^2 Y}{\partial Y^2} = \alpha^2 \tag{24}$$

Now, each function X and Y, has an independent representation and because the two independent functions are always equal they must be equal to a constant, defined as α^2. Rewriting to simplify, and replacing the partial differentials, definite differentials may be defined for the two functions.

$$\frac{d^2X}{dx^2} = \alpha^2 X \rightarrow d\frac{dX}{dx} = \alpha^2 X dx \rightarrow \frac{dX}{dx} = \alpha^2 \int X\, dx \tag{25}$$

Realizing that only the exponential function has the form where the derivative is equal to a function (or constant) allows the form of the solution to be immediately expressed.

$$X(x) = k_1 e^{\alpha x} = A cosh(\alpha x) + B sinh(\alpha x) \tag{26}$$

Now, solving for Y(y) in a similar manner results in the following.

$$Y(y) = k_2 e^{-\alpha y} = C cos(\alpha y) + D sin(\alpha y) \tag{27}$$

Finally, the voltage, expressed in terms of pure x and y components, may be written.

$$V = XY = [A\, cosh(\alpha x) + B sinh(\alpha y)][C cos(\alpha y) + D sin(\alpha y)] \tag{28}$$

Equation (28) can be expanded and by inspection arranged to show odd and even attributes.

$$\begin{aligned} V = {} & AC cosh(\propto x)\, cos(x) + AD cosh(\propto x)\, sin(\propto y) + BC sinh(\propto x)\, cos(\propto y) \\ & + BD sinh(\propto x) sin\,(\propto y) \end{aligned} \tag{29}$$

By judicious choice of axis, choosing odd symmetry about the y-axis, a large simplification can be made, specifically AC=BC=0, as these functions are not odd about the axis.

$$V = AD cosh(\propto x)\, sin(\propto y) + BD sinh(\propto x) sin\,(\propto y) \tag{30}$$

Now, the actual analysis of the field may be made based upon boundary conditions. Along the air gap edges, simple gradients will be assumed. This assumption is valid in particular when the gap distance is small. Along the left most edge, the simple BC will be defined as a linear gradient as Equation (31) shows.

$$V(x = 0, y) = V_{max} \frac{y}{y_{max}} \tag{31}$$

For this BC to occur, the voltage must approach the gradient function of (31) as $x \rightarrow 0$. In addition, as $x \rightarrow 0$ the factor, $BD \rightarrow 0$ and $AD \rightarrow AD sin(\alpha y)$. Thus, the factor AD may be determined.

$$AD = V_{max}\frac{y}{y_{max}\sin(\alpha y)} \tag{32}$$

The right most BC will be the piecewise combination of two linear voltage gradients in the air gap, separated by the rotor, which has a constant field. This profile, due to the symmetry of the chosen axis, can be represented by a Fourier sine series as the boundary is periodic. The voltage for Area 1 can now be computed and is shown in Equation (33).

$$\begin{aligned} V = V_{max}\frac{y}{y_{max}} + \sum_{n=1,odd}^{\infty} &\left(\frac{\sinh(\alpha_n x)\sinh(\alpha_n x)}{\sinh(\alpha_n x)}\right)\left(\frac{V_{max}}{n\pi}\right)\cos(n\pi) \\ &* \left[\left(\frac{y_{max}}{2n\pi}\right)\left(\frac{1}{gap} - \frac{2}{y_{max}}\right)\left(sin\left(\frac{2n\pi * gap}{y_{max}}\right)\right.\right. \\ &- \left(\frac{2n\pi * gap}{y_{max}} - n\pi\right)cos\left(\frac{2n\pi * gap}{y_{max}}\right) - n\pi\Big) \\ &+ \left(\frac{y_{max}}{2 * gap} - 1\right)\left(1 - \cos\left(\frac{2n\pi * gap}{y_{max}}\right)\right) \\ &\left. + \left(\frac{1}{n\pi}\right)\left(sin\left(\frac{2n\pi * gap}{y_{max}}\right) + \left(n\pi - \frac{2n\pi * gap}{y_{max}}\right)cos\left(\frac{2n\pi * gap}{y_{max}}\right)\right)\right] \end{aligned} \tag{33}$$

Evaluation of Equation (33) with an air gap of 15µm, 12mm gap between stator plates, 15mm rotor plate length, application of 1.0kV at 33%, 66% and 100% overlap results in a field as shown in Figure 25.

Finally, by integrating along the boundaries, the electric field, charge and capacitance can all be computed. The electric field is given by the negative gradient of the voltage field, charge is given by the surface integral of electric field and capacitance can be computed by the ratio of the charge to voltage. These steps are shown below.

$$\vec{E} = -\nabla V = \frac{\partial V}{\partial x}\overrightarrow{a_x} + \frac{\partial V}{\partial y}\overrightarrow{a_y} = -\left(\overrightarrow{E_x} + \overrightarrow{E_y}\right) \tag{34}$$

Splitting the voltage field into two components for computing the x-axis and y-axis components of the electric field, the partial differential equations reduce to ordinary differential equations and can be computed directly.

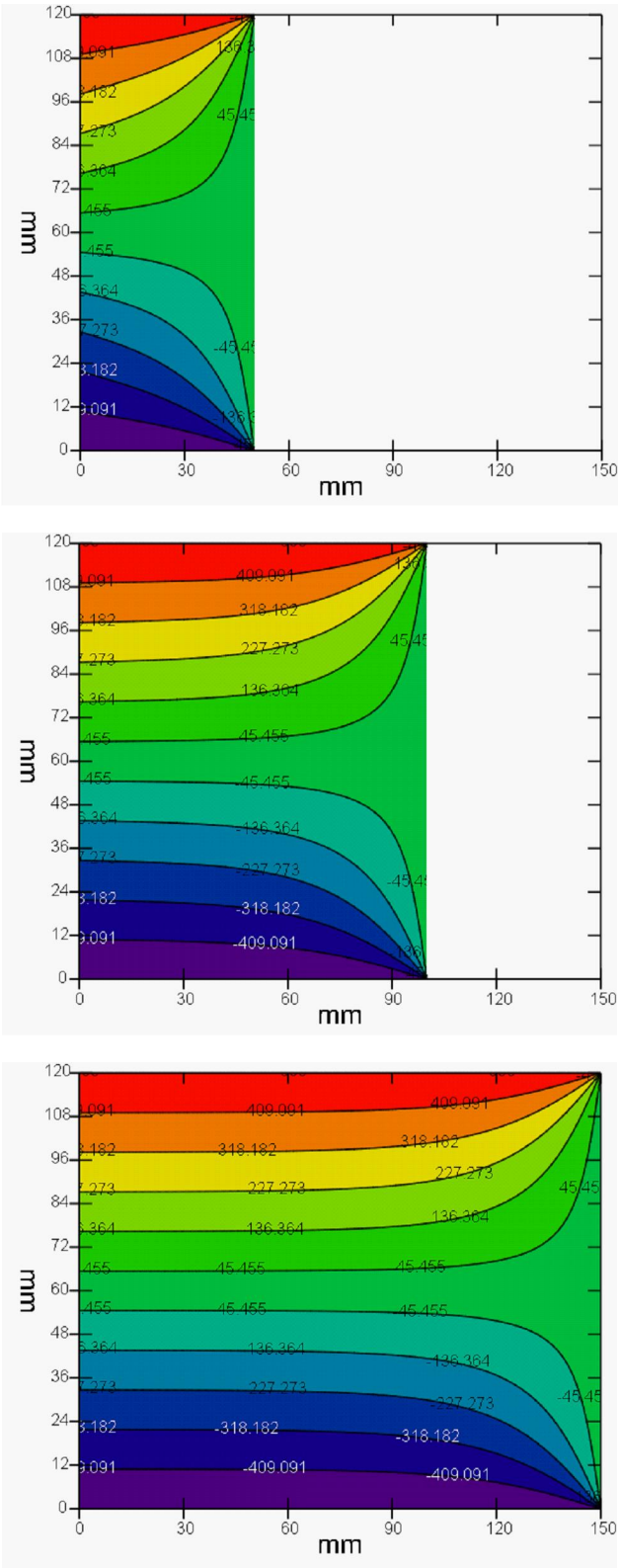

Figure 25 Area 1 Voltage Fringe Fields for 33% (top), 66% (middle) and 100% (bottom) Overlap

$$\overrightarrow{E_x} = 0 + \sum_{n=1,odd}^{\infty} \left[\alpha_n \left(\frac{\sin(\alpha_n y)\cosh(\alpha_n x)}{\sinh(\alpha_n x_{max})} \right) * \left(\frac{\sinh(\alpha_n x)\sinh(\alpha_n x)}{\sinh(\alpha_n x)} \right) \right]$$
$$* \left(\frac{V_{max}}{n\pi} \right) \cos(n\pi)$$
$$* \left[\left(\frac{y_{max}}{2n\pi} \right) \left(\frac{1}{gap} - \frac{2}{y_{max}} \right) \left(sin\left(\frac{2n\pi * gap}{y_{max}} \right) \right. \right.$$
$$\left. - \left(\frac{2n\pi * gap}{y_{max}} - n\pi \right) cos\left(\frac{2n\pi * gap}{y_{max}} \right) - n\pi \right) \quad (35)$$
$$+ \left(\frac{y_{max}}{2 * gap} - 1 \right) \left(1 - \cos\left(\frac{2n\pi * gap}{y_{max}} \right) \right)$$
$$\left. + \left(\frac{1}{n\pi} \right) \left(sin\left(\frac{2n\pi * gap}{y_{max}} \right) + \left(n\pi - \frac{2n\pi * gap}{y_{max}} \right) cos\left(\frac{2n\pi * gap}{y_{max}} \right) \right) \right]$$

$$\overrightarrow{E_y} = \frac{V_{max}}{y_{max}} + \sum_{n=1,odd}^{\infty} \alpha_n \left(\frac{\sinh(\alpha_n x)\cos(\alpha_n y)}{\sinh(\alpha_n x_{max})} \right) \left(\frac{V_{max}}{n\pi} \right) \cos(n\pi)$$
$$* \left[\left(\frac{y_{max}}{2n\pi} \right) \left(\frac{1}{gap} - \frac{2}{y_{max}} \right) \left(sin\left(\frac{2n\pi * gap}{y_{max}} \right) \right. \right.$$
$$\left. - \left(\frac{2n\pi * gap}{y_{max}} - n\pi \right) cos\left(\frac{2n\pi * gap}{y_{max}} \right) - n\pi \right) \quad (36)$$
$$+ \left(\frac{y_{max}}{2 * gap} - 1 \right) \left(1 - \cos\left(\frac{2n\pi * gap}{y_{max}} \right) \right)$$
$$\left. + \left(\frac{1}{n\pi} \right) \left(sin\left(\frac{2n\pi * gap}{y_{max}} \right) + \left(n\pi - \frac{2n\pi * gap}{y_{max}} \right) cos\left(\frac{2n\pi * gap}{y_{max}} \right) \right) \right]$$

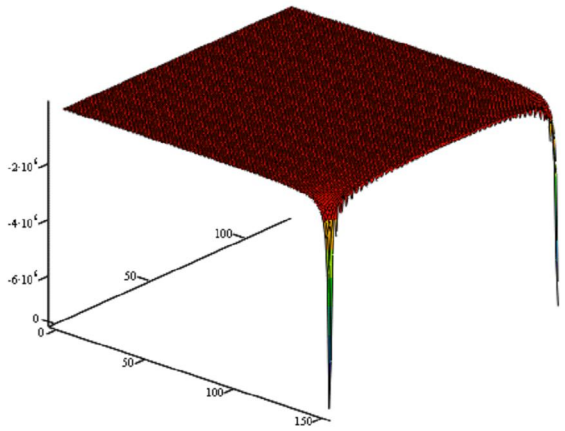

Figure 26 Electric Field of Area 1

Plotting the electric field shows that only the gap fringes have significant field. For computing the charge, it is assumed that the rotor is truly isolated, no source of leakage, thus it does not contribute the calculation. Further, it is also assumed that there is an equal yet opposite charge build up on the two stator plates. Charge and then capacitance can be computed for Area 1 by recognizing that E will exit normal the stator and rotor surfaces and assuming that all E has been accounted for in the model (eg all fringe is included). This assumption may have little merit when the rotor is unaligned, however, its validity will grow with rotor overlap (alignment) and it allows for a predictive solution to be found.

$$Q_{S+} = Q_{S-} = \oint \varepsilon \vec{E} \cdot ds \tag{37}$$

$$\begin{aligned} Q_{area1} = \varepsilon \frac{V_{max} x_{max}}{y_{max}} + \varepsilon \sum_{n=1,odd}^{\infty} \left(\frac{\cos(\alpha_n y)\,(\cosh(\alpha_n x_{max}) - 1)}{\sinh(\alpha_n x_{max})} \right) \\ * \left(\frac{V_{max}}{n\pi}\right) \cos(n\pi) \left[\left(\frac{y_{max}}{2n\pi}\right) \left(\frac{1}{gap} - \frac{2}{y_{max}}\right) \left(sin\left(\frac{2n\pi * gap}{y_{max}}\right) \right.\right. \\ \left. - \left(\frac{2n\pi * gap}{y_{max}} - n\pi\right) cos\left(\frac{2n\pi * gap}{y_{max}}\right) - n\pi \right) \\ + \left(\frac{y_{max}}{2 * gap} - 1\right) \left(1 - \cos\left(\frac{2n\pi * gap}{y_{max}}\right)\right) \\ \left. + \left(\frac{1}{n\pi}\right) \left(sin\left(\frac{2n\pi * gap}{y_{max}}\right) + \left(n\pi - \frac{2n\pi * gap}{y_{max}}\right) cos\left(\frac{2n\pi * gap}{y_{max}}\right) \right) \right] \end{aligned} \tag{38}$$

Solving for the charge of area 1 allows for the capacitance to finally be determined as shown in (39).

$$C_{area1} = \frac{Q_{area1}}{V_{max}} \quad (39)$$

3.4.2 Area 2 – Fringe Field

Area 2 is a trailing fringe field. The top and right boundaries (See Figure 24-b) are difficult to define as assumptions of linear gradients are not valid. However, one means to solve for the fringe field is via a conformal map whose purpose is to warp all space into a geometry which can be solved. By warping the problem to a simple geometry, assumptions of linear gradients of the transformed air gaps become valid which can then be used to solve the problem in the transformed domain. To help insure generality and because the initial and final geometry can be described with a polygon, a Schwarz-Christoffel conformal mapping method has been utilized.

In seeking simplicity and convenience, it was chosen to warp the initial geometric space into a rectangle, wherein the electric field could easily be solved. Once solved, the process for warping space into a rectangular space could be reversed while carrying the solution back, on a point-by-point basis. Because the transformations are analytic (satisfies Cauchy-Rieman) and conformal (derivative is non-zero) the properties of the system, such as conductivity or capacitance, remain invariant to the transformations.

Figure 27 outlines the geometry and boundary conditions for solving for the fringe field. With reference to Figure 23, the line between points A and B represent the trailing edge of a stator. The line between points B and D represent the air gap between the stator and rotor with point C being placed at the exact center of this gap. The lines connecting points D, E and F represent the non-overlapped top and half of the trailing edge of the rotor. Point F is located at the center point of the trailing edge of the rotor to insure symmetry of the positive and negative portions of this problem. Point G is located on the positive x-axis at infinity. It is assumed that the closed boundary from points A to G encompass all of the electric field.

By conveniently choosing an axis, the first of four transformations can be made. This first transformation is to splay all points of the Z-plane onto a single axis. This is accomplished by simply taking the square root of the points which transforms the Z-plane to the T1-plane, also known as the positive half-plane (H^+). Figure 28 shows this first transformation.

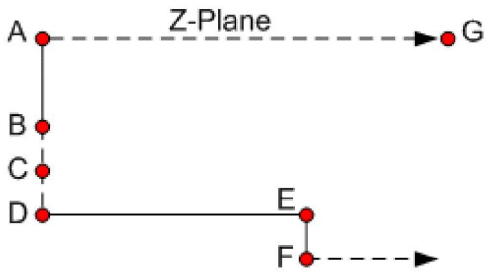

Figure 27 ESM Boundary To Solve

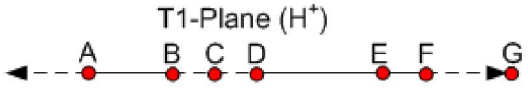

Figure 28 Non-Symmetric Half Plane (T1)

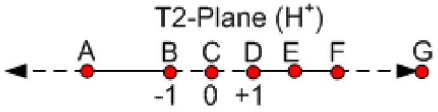

Figure 29 Symmetric Half-Plane (T2)

$$\frac{z-1}{z+1} = c\frac{w-1}{w+1} \tag{40}$$

Solving for the location of each point in the T1-plane results in non-symmetric locations as the original polygon of Figure 27 is non-symmetric. To create a rectangle, the corner point locations must be uniformly spaced and symmetric which requires the T1 points to be redistributed. To produce a rectangle by redistributing the corner points a bilinear transform was employed to shift the boundary points. This bilinear transform is given in (40), where *z* is a complex point in the z-plane, *w* is a complex point in the w-plane and *c* is a constant. Recognizing that the small air gap, points B-to-D, and the large air gap, points F-to-A must be spatially equal in the final rectangle, points B and D were purposefully chosen to be located at +/- 1.

Once the geometry has been defined, the Schwarz-Christoffel Equation for this particular geometry can be created and is given in (41), where K_1 and K_2 are two complex constants that describe shift, scale and rotation of the solution. Because of the chosen

geometry, only four points need to be identified. Points that do not represent a change in direction of the polygon (angle of 180˚) result in unity. Because the chosen geometry has been setup to insure each inflection is of 90˚ only four points need to be identified. Point G need not be identified because it resides at infinity and by definition results in a unity term.

$$Z(t) = K_1 + K_2 \int_{t_A}^{t_H} \frac{\sqrt{\tau - t_E}}{\sqrt{(\tau - t_A)(\tau - t_D)(\tau - t_F)}} d\tau \tag{41}$$

The specific locations of the remaining four points were then determined using a numerical method that compares line lengths between each set of points in the two planes Z and T1. This numerical method, developed by Foster and Anderson[17] solves for the unknown locations t_A, t_D, t_E and t_F by solving a ratio problem shown below in Equations (42) and (43). The method works because the process is conformal thus boundary ratios are equivalent between transformation domains.

$$\frac{Z_2 - Z_1}{Z_3 - Z_1} = \frac{\sum_{j=1}^{N} f(p_j^{12})}{\sum_{j=1}^{N} f(p_j^{13})} \tag{42}$$

$$p_j^{lm} = \frac{t_m + t_l}{2} + \frac{t_m - t_l}{2} cos\left[\frac{(2j-1)\pi}{2N}\right] \tag{43}$$

Solving for these ratios allows Equation (41) to be solved with an inverse elliptic integral. Now, the T2 plane can now be warped into a rectangle, the W plane. This transformation given by (44) transforms all of space represented by the upper half place, into a rectangle.

$$w = f(T2) = sn^{-1}(\varphi, k) = \int_0^{\varphi} \frac{1}{\sqrt{1 - k^2 sin^2(\varphi)}} d\varphi \tag{44}$$

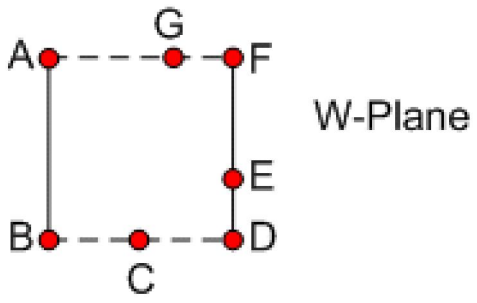

Figure 30 Rectangular Plane (W)

Finally, the voltage gradient, electric field and capacitance solutions can be computed. The solution in the W-plane is simple, as voltage and electric fields become linear functions of position as all space has been represented. Capacitance is computed as function of length and width in the W-Plane as shown in Equation (47), where K is the complete elliptic integral with parameter κ[18].

$$\frac{C}{\varepsilon_0} = \frac{K(\kappa')}{K(\kappa)} \tag{45}$$

$$C_{Z-Plane} = C_{T-Plane} = C_{W-Plane} \tag{46}$$

The left boundary defined by points A-B still represent the trailing edge of the stator and are given a potential of $\frac{1}{2}V_{max}$ while the right boundary defined by points D-F have a zero voltage defined by the rotor. The left and right boundaries are Dirchlet boundaries defined as a constant, while the top and bottom have linear gradient Neuman boundary conditions.

To minimize processing requirements, the solution was computed with 15 field lines (contour lines) which are defined by 75 unique points. Once the solution is computed at each point in the rectangle, the transformation process can be reversed while carrying the solution to solve for the field lines. Figure 31 shows the process of computing the voltage field for a rectangle, then carrying that solution back through the transformations. Figure 31(a) show the initial rectangle with voltage solution in Figure 31(b). This rectangle is then transformed back to a symmetric half plane via an elliptic integral, Figure 31(c and d). This symmetric half plane is then shifted via a bilinear transform to a non-symmetric half-plane as shown in Figure 31(e and f), which is finally transformed into the original geometry (polygon) via the Schwarz-Christoffel integral as shown in Figure 31(g and h) which is clearly comparable to Figure 27 that defines the originating geometry.

It is worth pointing out, that unless field lines are needed for a solution capacitance and charge can be computed for Area 2 using Equation (15) and (45) from the rectangular conformal W-plane shown in Figure 31(b). This domain in inclusive of all space and is *conformal*, thus physical parameters such as capacitance are invariant to the transformation. Thus capacitances of all of the transformed planes are equivalent as stated in Equation (46). For this reason, capacitance can be computed directly as if it is a parallel plate capacitor in this transformed domain.

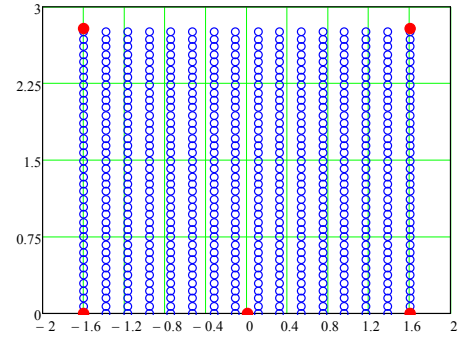

(a)

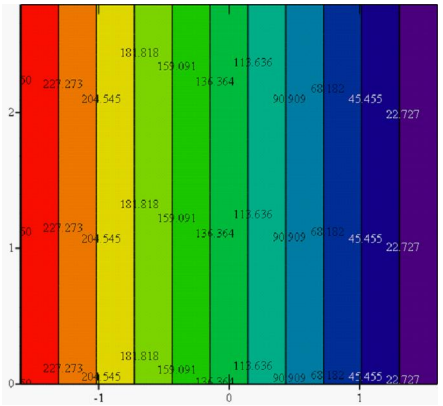

(b)

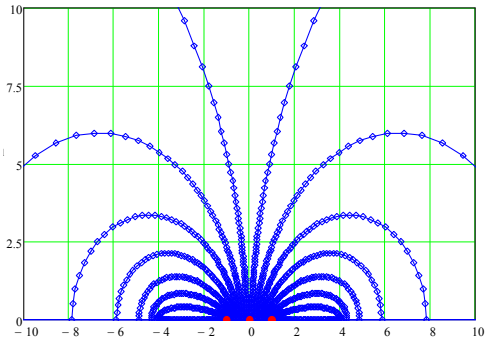

(c)

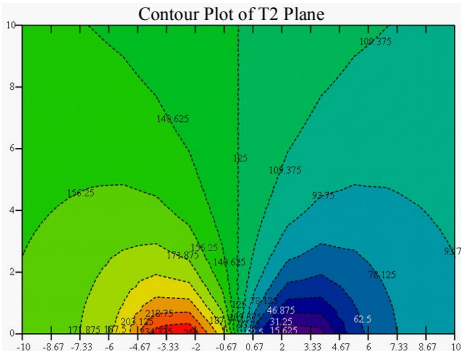

(d)

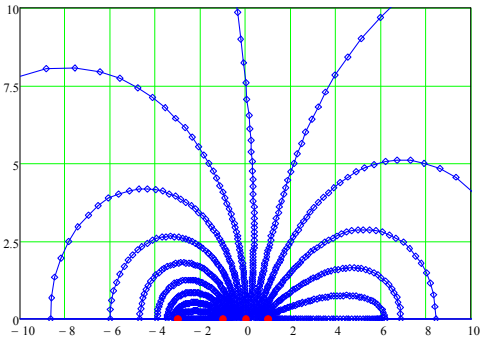

(e)

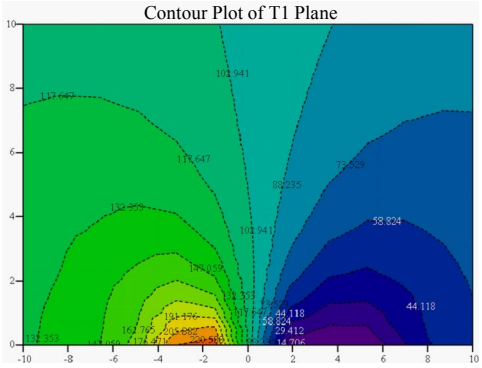

(f)

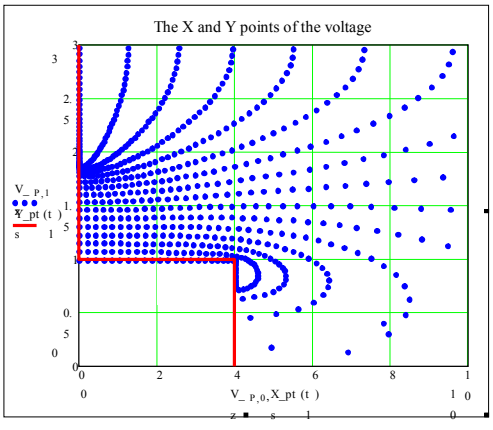

(g)

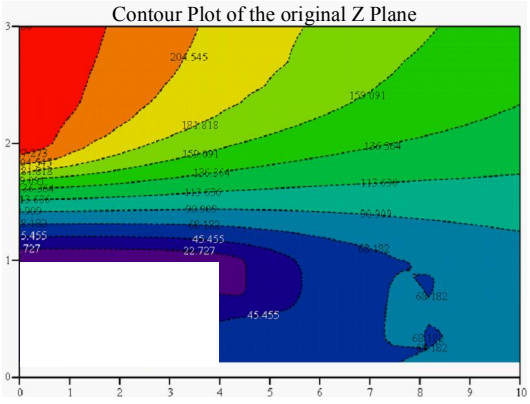

(h)

Figure 31 Area 2 Voltage Fringe Field Components

3.4.3 Area 3 - Rotor-Stator Overlapped Area

Except for scale and location, this area is defined identically to the rectangular solution of the previous section. It is assumed that no fringing occurs in this region due to a small air gap, that the top and bottom are constants as they are modeled as ideal conductors and that the left and right edges, bounded by an air gap, can be approximated as linear voltage gradients.

3.5 Modeling Mechanical and Coupling Forces

Now that a method to define the field has been developed, a mechanical model describing how force arises from the field is presented. To develop a logical design methodology for the SIM, mechanical, electrical and their coupling relations are needed. Modeling of the mechanical and coupling relations are presented now.

3.5.1 ES Forces of Simple Systems

The force between two point charges is given by Coulomb's Law. If this force is written on a per unit charge, then the vector field called the *electric field intensity* can be described, as shown in (47).

$$\vec{E} \equiv \frac{\vec{F}_{ES}}{Q} \tag{47}$$

Assuming parallel plates, (47) can be rewritten to determine the force based upon materials, material limits and geometry of an ES system, as shown in (48).

$$\overrightarrow{F_{ES}} = Q\vec{E} = \left(\oint_A \varepsilon \vec{E} \cdot da\right)\vec{E} = \varepsilon\overrightarrow{E^2}A \tag{48}$$

Recalling the definition of voltage, (48) can be rewritten to give the maximum force possible between parallel plates, which is shown in (49) and displayed in Figure 32.

$$\left|\overrightarrow{F_{ES-Norm}}\right| = \left|\frac{1}{2}A\overrightarrow{E^2}\right| = \frac{\varepsilon A}{2}\left(\frac{V}{\vec{d}}\right)^2 \tag{49}$$

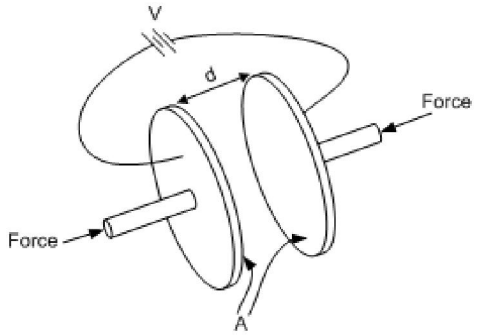

Figure 32: ES Force Diagram of Parallel Plates

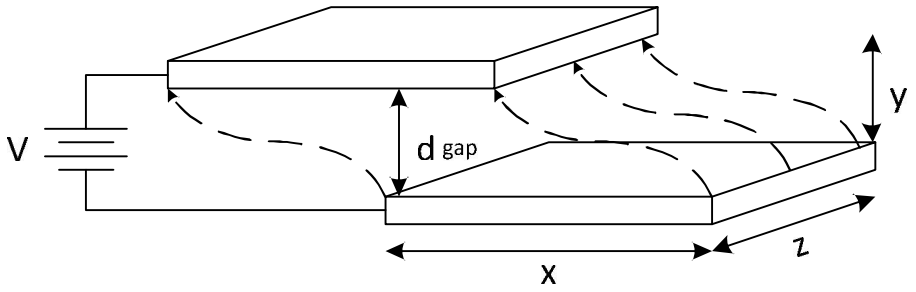

Figure 33: ES Force Diagram of Linear Plates

However, for a switched impedance linear motor, linear motion is desired. Thus, if the one plate shown in Figure 32 is held in a fixed position while the lower plate is allowed to move along a tangential path then the total force, utilizing stress tensors or conservation of energy analysis means, may be discovered and is shown in Equation (50). Note that force is developed with two degrees of freedom, a tangential force (or shearing force) and a normal force. It is the tangential force along the x-axis with which we gain utility from the SIM. A derivation of Equation (50) is given in Appendix C. Equation (50) shows the relationship between the forces and capacitance.

$$\begin{aligned}\overrightarrow{F_{ES}} &= \left(\frac{\varepsilon \cdot z}{2}\frac{{V_{gap}}^2}{d_{gap}}\right)a_X + \left(\frac{\varepsilon \cdot z \cdot x_{Ovr}}{2}\frac{{V_{gap}}^2}{{d_{gap}}^2}\right)a_Y \\ &= \frac{1}{2}C \cdot {V_{gap}}^2\left[\left(\frac{1}{x_{Ovr}}\right)a_X + \left(\frac{1}{d_{gap}}\right)a_Y\right]\end{aligned} \tag{50}$$

Combining the force equation with knowledge of the gap breakdown threshold as described in Equation (21) and Figure 19 and Figure 20 results in an optimal gap size for operation. The optimal gap size occurs when the tangential force, shown in Figure 34, is a maximum. If the voltage drop of the gap remains below a useful threshold, occurring when the gap is too small or the dielectric is too thick, then a less than optimal force producing field will occur. (The computed forces for the test rig of Chapter 4 using Kapton HN30 as a dielectric at various overlap positions are shown in Figure 34 and Figure 36.)

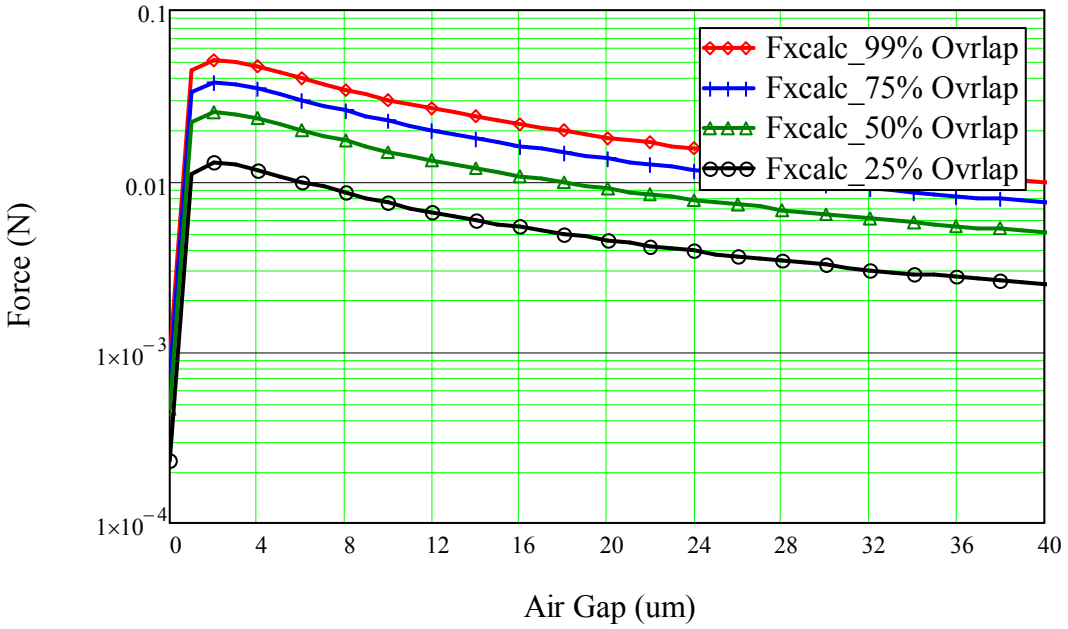

Figure 34 Computed Tangential Force vs Air Gap

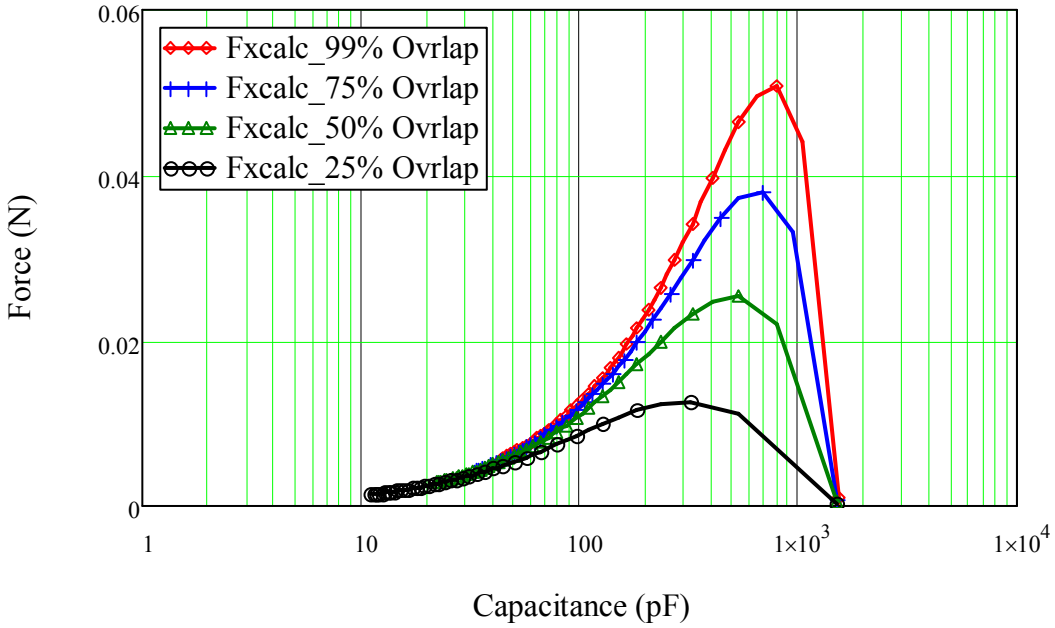

Figure 35 Computed Tangential Force vs Capacitance

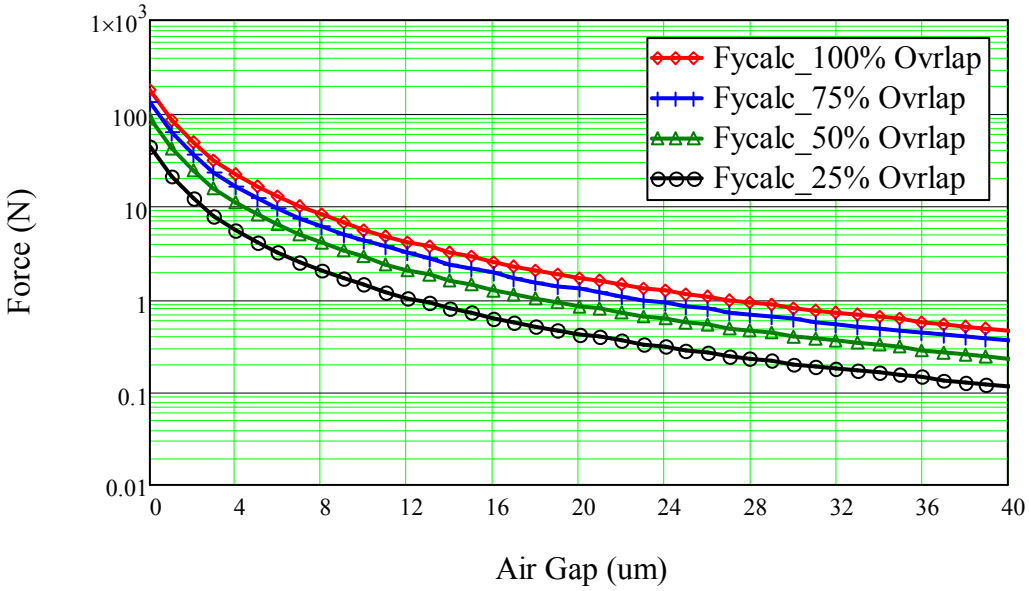

Figure 36 Computed Normal Force vs Air Gap

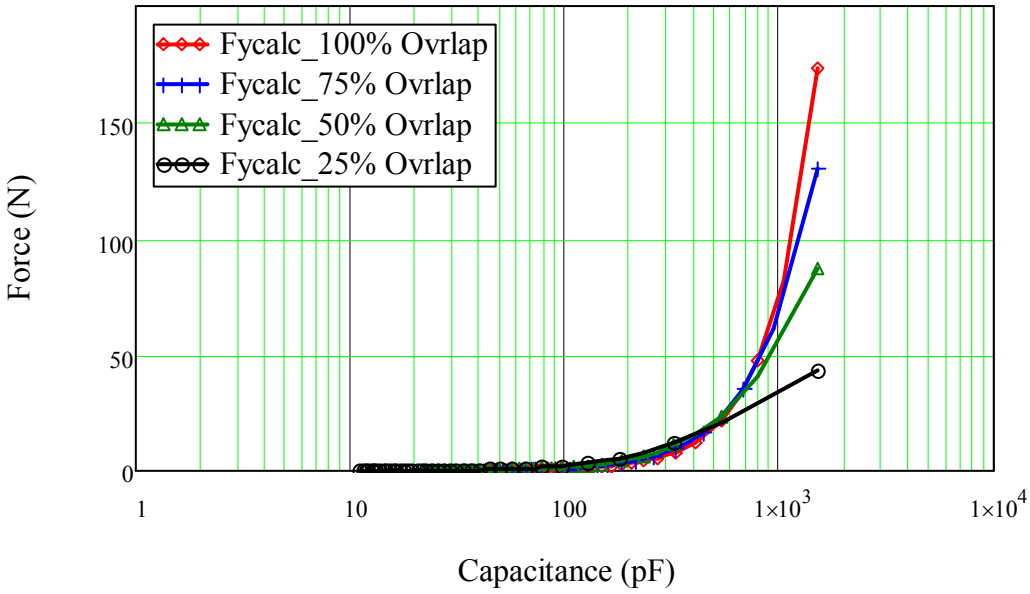

Figure 37 Computed Normal Force vs Capacitance

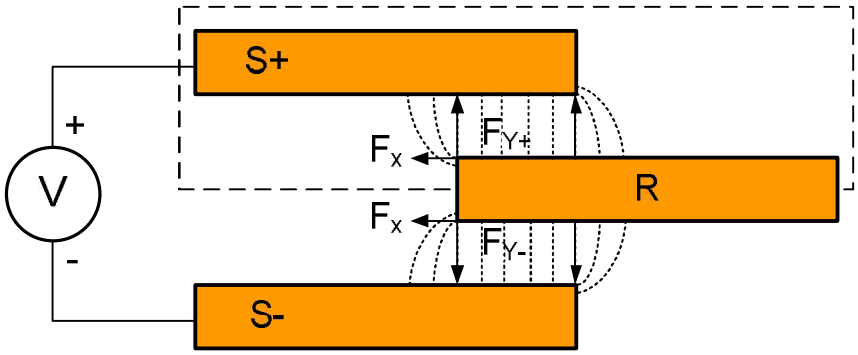

Figure 38 Force Symmetry Diagram

For development of an ESM, linear or rotational, it must be realized that Figure 33 and Equation (50) represent only half of a symmetric system as shown in Figure 38. When a voltage is applied to the stator plates, half of the applied voltage will drop in each air gap (assuming an electrically isolated rotor). Figure 38 also shows that the net tangential force will sum together as they are in the same direction. It also shows that the net normal force on the rotor will be zero. Equations (51) and (52) show this symmetric property.

$$\overrightarrow{F_{ES\_ESM\_X}} = \left(\varepsilon \cdot z \frac{{V_{gap}}^2}{d_{gap}}\right) a_X = \frac{C}{x} {V_{gap}}^2 \tag{51}$$

$$\overrightarrow{F_{ES\_ESM\_Y+}} = -\overrightarrow{F_{ES\_ESM\_Y-}} = \left(\frac{\varepsilon \cdot z \cdot x_{Ovr}}{2} \frac{{V_{gap}}^2}{{d_{gap}}^2}\right) a_Y = \frac{C}{2d_{gap}} {V_{gap}}^2 \tag{52}$$

While the net force on the rotor will be zero, a force upon the individual conductive plates (rotor and stator) will exist due to the induced charge buildup. For this reason, the bond between the conductive plate and their substrate must exceed the normal force else mechanical failure between the substrate and plate may occur.

3.6 Conclusion

This chapter presented a logical design methodology for a SIM. It also detailed breakdown mechanisms and locations as well as an analytic method to define the gap fields that lead into a description of linear forces.

While the fundamental design methods were presented, knowledge of the maximum obtainable breakdown field must be known to optimize an SIM design. Chapter 4 presents experimental results that determine the gap breakdown of air for development of a linear static test SIM design.

Chapter 4 Analytic Model Validation

In order to model SIM capabilities and performance characteristics, it is necessary to first measure the breakdown field strength of the gap to gage the upper limits of performance. Then with close correlation to measured experimental results of force and capacitance the analytic models presented in Chapter 3 can be shown accurate and valid. To achieve this validation, two static test rigs have been created. The first test rig is designed to measure the breakdown field strength of a simple air gap for generating Paschen curves. Then with this breakdown knowledge, predictions of achievable force generation can be computed, using the design methods of Chapter 3, with which a second test rig measuring forces and capacitance could verify.

4.1 Paschen Curve Measurement Test Rig

Prior to design and construction of a SIM, knowledge of the air gap breakdown field strength must be acquired to provide a baseline for predicting achievable performance. To accomplish this, a custom test rig that utilizes a *cylinder and piston* concept, shown in Figure 39 - Figure 41, was designed to allow precise positioning of parts from which plots of air gap vs breakdown voltage and field can be made. This cylinder design was used to limit angular positional deviations and prevent stack-up error, the combining of tolerance errors during the manufacturing process.

The test rig was designed to maintain a parallel tolerance of 12μm between faces of two 300 series stainless steel conduction heads. Linear positioning of the heads was accomplished using a ThorLabs® DM12 Differential Adjuster that is capable of making single micron linear positional changes. The conduction heads are precisely guided along an outer ceramic cylinder that provides reference for maintaining parallel position. The outer cylinder and piston head are made of Macor®, a machinable ceramic with high dielectric strength. Slots were cut into the outer cylinder allowing probes to connect with the two conduction heads so that a voltage can be applied between them. By recording the applied voltage at breakdown and the gap distance, measured from the precision adjuster, Paschen curves for air, Kapton® and ZrO_2 coatings of various thicknesses were created.

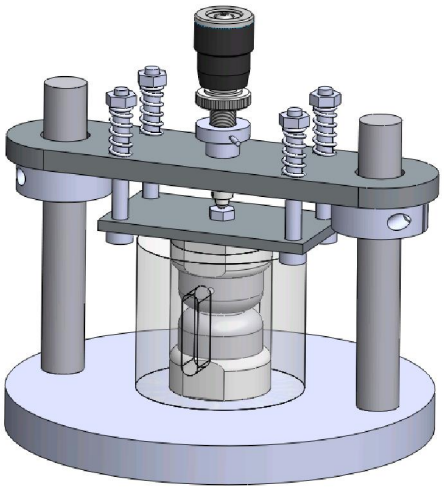

Figure 39 Paschen Curve Test Rig Model

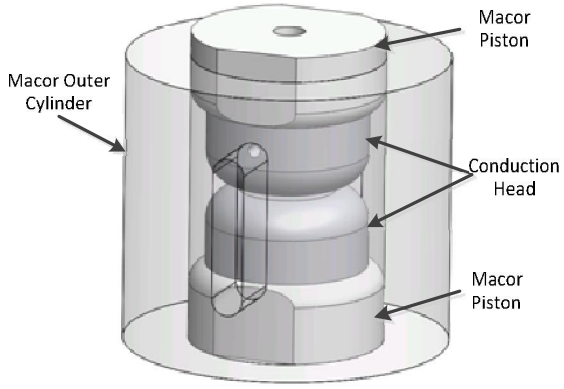

Figure 40 Cylinder and Piston Model of Test Rig

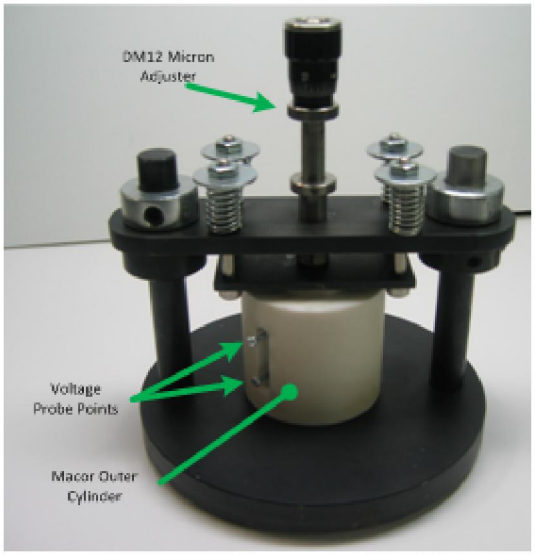

Figure 41 Assembled Paschen Curve Test Rig

4.2 Paschen Curve Test Rig Results

Because of their reportedly high dielectric strength, coatings of ZrO_2 and Kapton® of various thicknesses have been created and tested.

4.2.1 Zirconium Dioxide Coating Results

Experimental results of ZrO_2 coatings of 0.5µm, 1µm and 2µm thickness are shown in Figure 42. The figure shows the distinctions between the analytic Paschen Curve formulation and empirical measurements of the bare plate and coatings. It also shows that the ZrO_2 coating of 0.5µm has virtually no effect on the breakdown, following the bare plate (uncoated) curve closely while a 1µm or 2µm thick coating show a potentially useful effect at gaps below about 5µm. For gaps below about 5µm, the figures show that breakdown was inhibited by the coating. The 1µm coating showed a plateau breakdown effect while a 2µm coating shows a region of elevated breakdown field for gaps below about 2µm. Above 5µm, breakdown of all tested ZrO_2 coatings closely followed the bare plate breakdown.

Figure 42 also shows a nearly linear relation between the computed Paschen curve for air and the measured breakdown values for gaps above about 10µm. However, there is an offset to the two curve sets. The figure shows the computed Paschen breakdown roughly 100V lower than the empirical measurements. A primary reasons for this offset may be due to the testing geometry from which the general Paschen Curve formulation is derived. General Paschen Curves are created based upon an ASTM method such as D-877, D-3151 and D-149. These 'standard' methods utilize spherical probes rather than polished planar ones (conduction heads) necessary for SIM utilization. The geometric differences result in differing electric field patterns which could account for the offset.

Figure 43 shows the computed electric field for the ZrO2 coatings. The plot shows little variation in the applied field for the different coating thicknesses which implies a linear relation between the dielectric strength and thickness for the tested range.

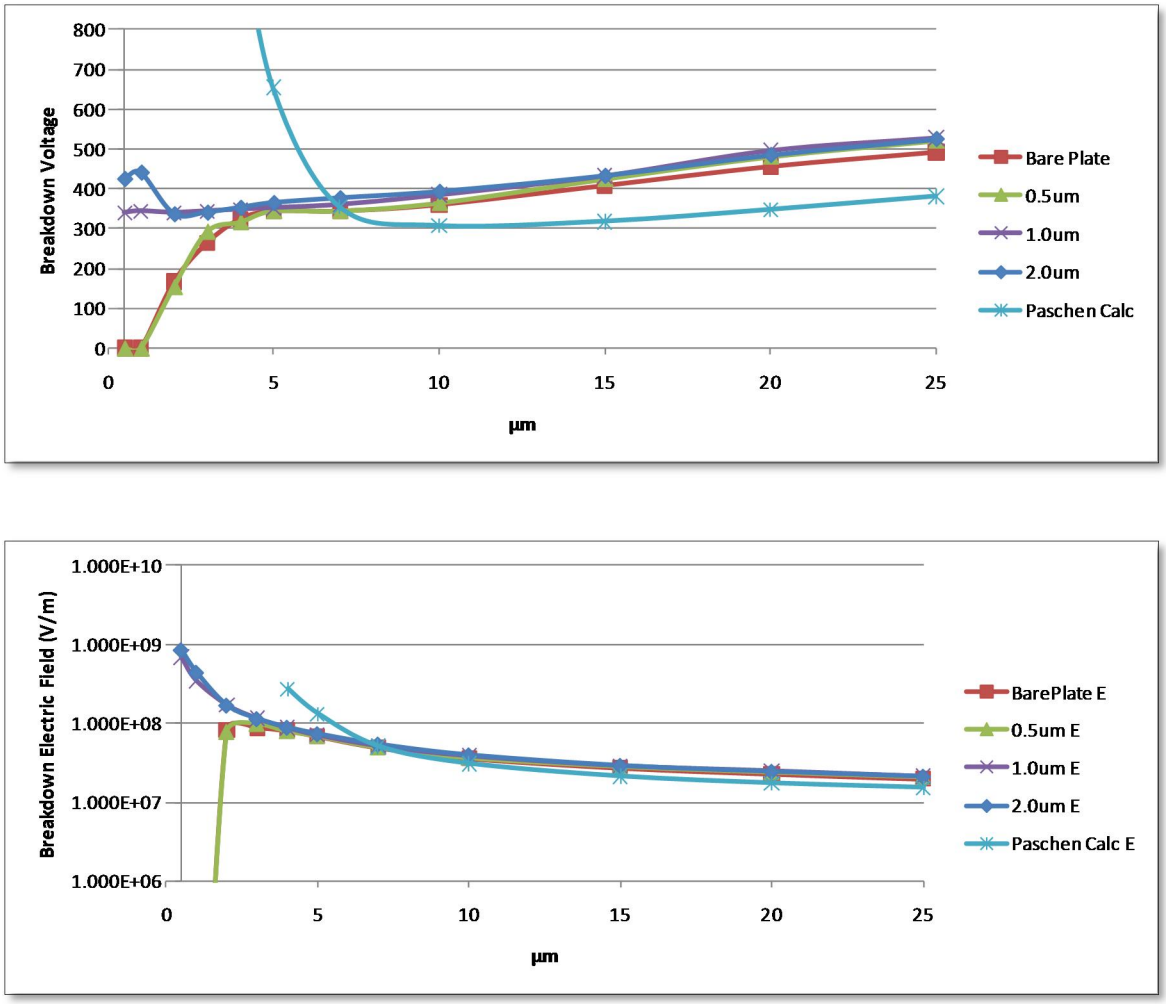

Figure 43 Computed Breakdown Field for ZrO_2 Coatings at 1atm

4.2.2 Kapton Film Results

As with ZrO_2, Paschen curves for Kapton film have been developed. Figure 44 shows the Paschen curves empirically measured for a bare plate and for film thickness of 7.6, 12.7 and 25.4µm which are the specific Kapton films of HN30, HN50 and HN100 respectively. Figure 45 shows a voltage breakdown detail of Figure 44 for gaps <25µm. Figure 46 shows the computed electric field breakdown with Figure 47 showing a detail of it for gaps <25µm.

The x-axis range for Kapton film figures expands to 150µm, well beyond the 25µm range of the ZrO_2 figures, to show their alignment with the bare plate measurement. This point is worth noting, Kapton has an improved ability over ZrO_2 to inhibit breakdown in relatively large gaps.

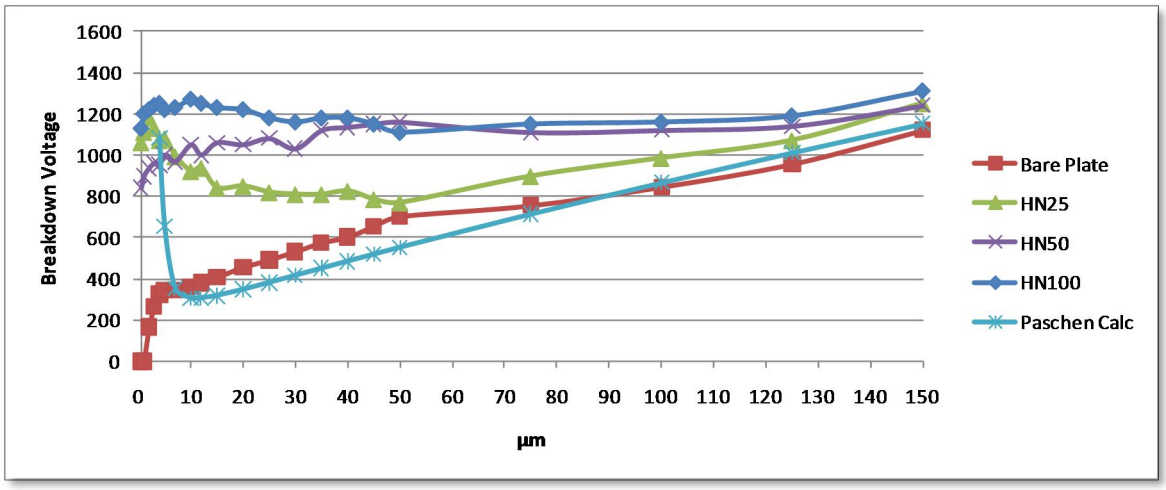

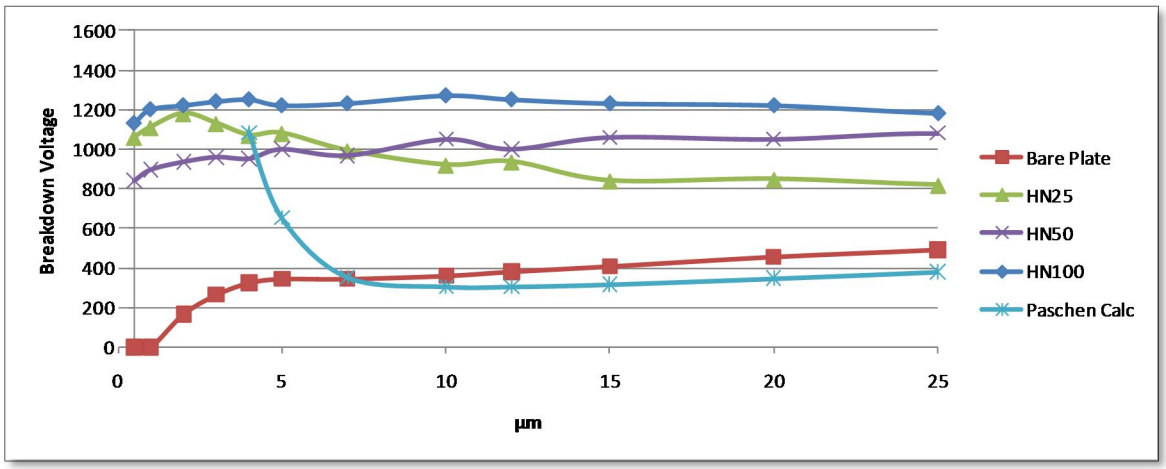

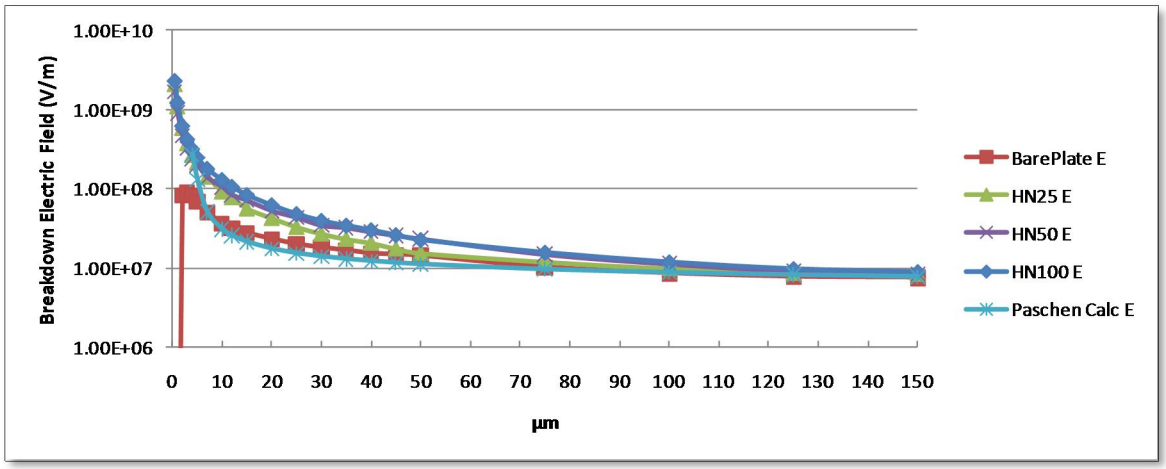

Figure 46 Computed Breakdown Field of Kapton Films <25µm

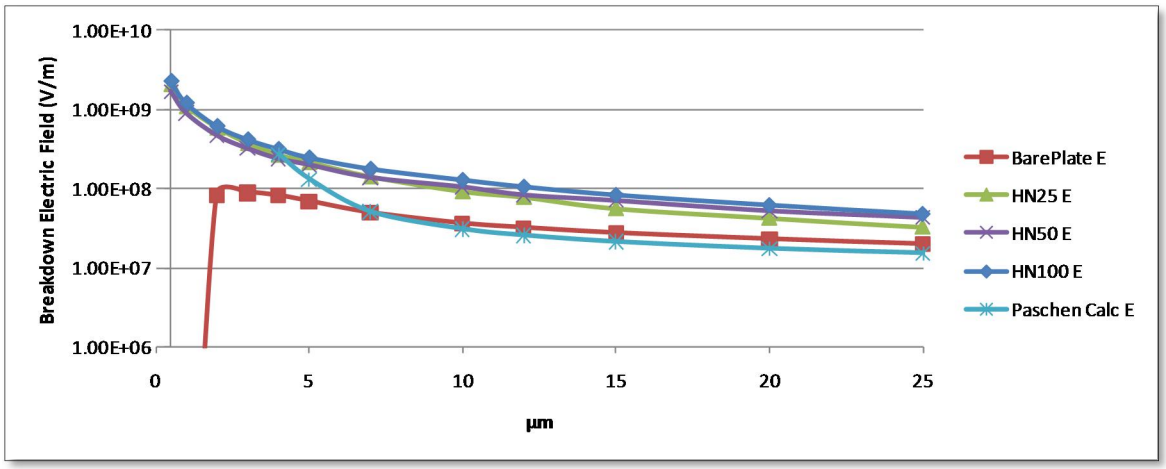

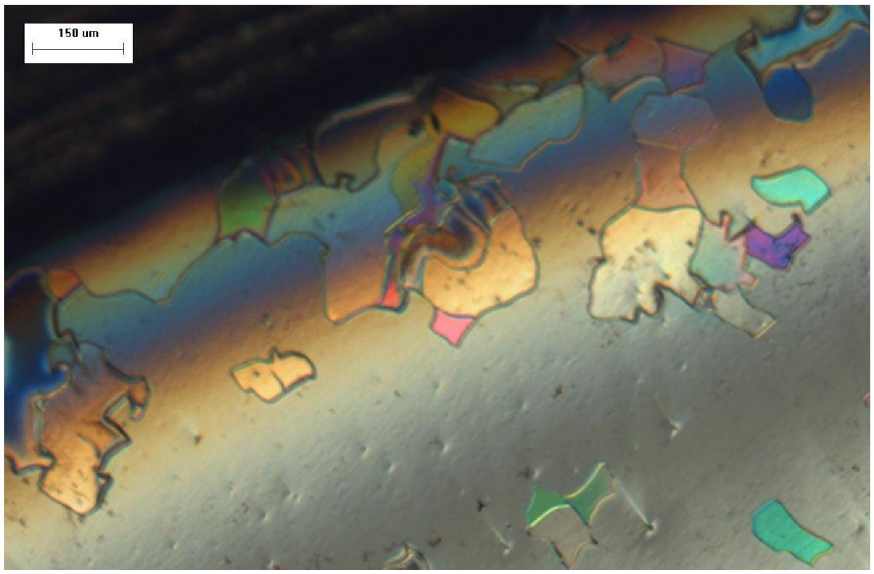

Figure 49 Flaking of ZrO2 Coating at Corner - Zoom

4.2.3 Zirconium Dioxide Inhibitors

These experiments have shown that ZrO_2 could be a useful coating for SIM applications, however, achieving large scale deposition economically will still need to be shown. The ability to apply "thick" coatings above 1µm proved difficult to achieve as stress internal to the zirconium crystal can grow during its deposition and can destroy the coating as shown in Figure 48 and Figure 49. Figure 48 shows a conduction head from the Paschen rig with 'fingers' of ZrO_2 pealing and flaking due to crystal stress present at room temperature and pressure.

4.2.4 Paschen Rig Test Summary

Figure 42 - Figure 47 show that it is possible to develop fields useful for ESMs using existing materials although maintaining the necessary gap in operation is an open question. Figure 50 shows the computed stress for the computed ideal Paschen curve, Kapton HN100, ZrO_2 at 2µm thickness and for the magnetic strengths of 1.2T, 1.6T and 2T as presented in Chapter 1. The figure shows that it is possible to generate electric fields on macro scales (because the Paschen test rig is a comparably large device) that could be useful for industry. In fact, there is only about 100x variation between HN100 and the stress computed for the magnetic field of 2T at 25µm (1mill).

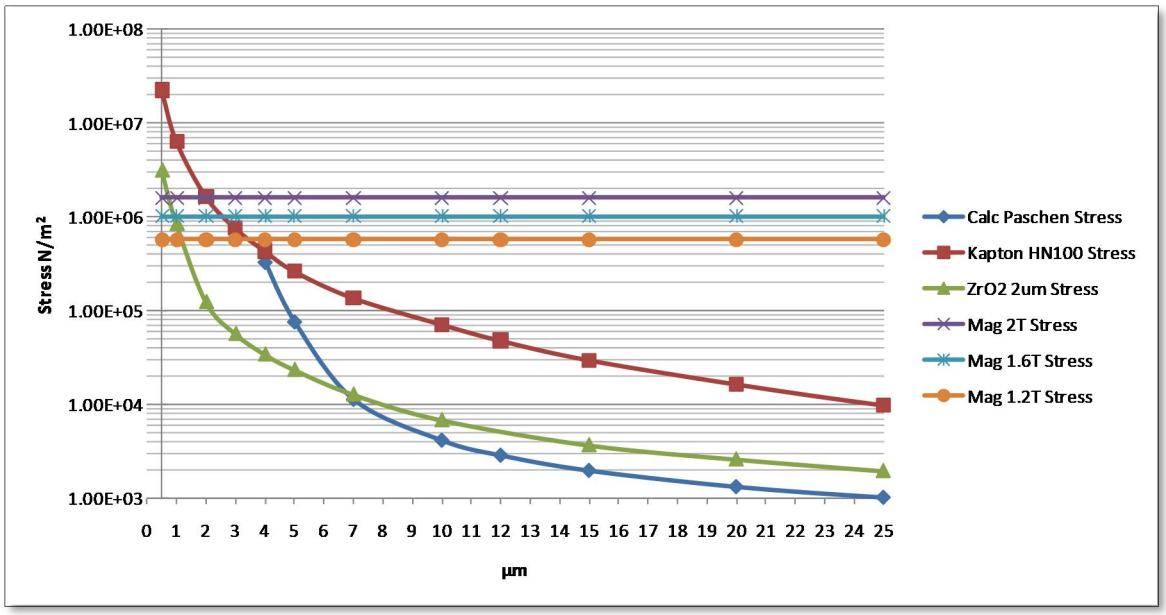

Figure 50 Maxwell Stress Comparison

4.3 Linear Force vs Gap Test Rig

Using the Paschen rig test results as a basis for the achievable electric field strengths allows the achievable forces to be predicted using analytic design methods developed in Chapter 3 and a linear static force test rig to be designed for comparison. In addition to empiric tested results, finite element (FE) models have been created and utilized to validate force models. By establishing close agreement of the normal and tangential forces between the analytic and experimental results validation for the analytic model can be claimed. As only a change of variable is necessary to utilize the linear models in a rotational frame applicable to SIMs validation of the linear model is assumed to also validate rotational frames.

4.3.1 Linear Force Rig Physical Description

A test rig designed to decouple the normal and tangential forces in a linear alignment was made. This design also allows various dielectrics to be tested with relative ease while neatly replicating the electrical structure of a SIM as shown in Figure 51.

The critical components of the linear force test rig are three conductive stainless steel heads at the center of the rig as shown in Figure 52. These stainless steel plates mimic two outer stator plates and one center rotor plate. These plates are held in fixed location and are electrically isolated by an insulating ceramic backing and ceramic screws as shown in Figure 53. The structure that holds them in place rests on linear rails. Rails were used to insure motion exists in only one direction, thus allowing measurement of a linear force that is decoupled from other axis forces. The electrical model of the experiment is shown in Figure 51 and helps to illustrate the relation of the coatings and air gap. The thickness of the coating is presumed to be fixed, while the air gap is varied by use of the displacement wedges.

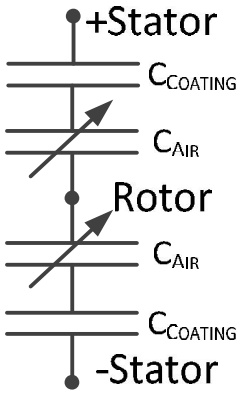

Figure 51 Equivalent Linear Rig Test Circuit

When a force is created, via placement of a charge due to an applied voltage, it is transferred through the rail structure to a compressive piezo-electric load cell as shown in Figure 54. The output of the load cell which measures applied force was then read from an oscilloscope for recording. Because air gaps for this system are measured in microns, it was necessary to use piezo-electric load cells whose full scale displacement for this force range is smaller than the gap. Once a force measurement has been obtained, the rotor or the stator plate positions were varied to change the rotor-stator overlap or to open the gap. During experiments, capacitance measurements of the conduction heads were made and compared to calculated values for indication of the achieved or effective gap size.

The linear test rig was fabricated using 300 series stainless steel similar to the conduction heads of the Paschen rig. Stainless was again chosen to insure that once a surface had been machined and polished to proper tolerance that oxidation or other corrosion would not adversely damage it. Each critical part of the rig was heat treated to minimize deformation under load and each critical surface was cut using an electric discharge machine (EDM) that can hold dimensional tolerance to within 2.54µm (0.1mil). Although each individual part has been held to a tight tolerance, the combination of part tolerance leads to a cumulative stack-up error. There are nine surfaces between the front surface of any conduction head and surface of the base plate which leads to a computed alignment error of about 23µm.

Submicron precision and knowledge of the gap is necessary to correlate experimental results to predicted values. To achieve this goal the DAS110 differential adjustment screw from ThorLabs® was used for the precision positioning. (Product data sheet is listed in Appendix D.) The screw has a 80tpi course thread and a fine adjustment screw able to achieve a displacement of 25.4µm. This adjustment screw is used to push a wedge that operates with a 10:1 ratio to insure fine positioning of the stator conduction heads. The displacement wedge thus reduces the movement of the differential adjustment screw by 10x and does so in a direction perpendicular to the screw as shown in Figure 55. The displacement of the wedge and wedge assembly is transferred to the structure holding the linear rails. A stator slide assembly with wedge assembly is shown in Figure 56.

Figure 57 shows a top view of the complete linear test rig with focused view of the conduction heads. The figure identifies the physical location relationships between the heads, rail structure and displacement wedge assembly.

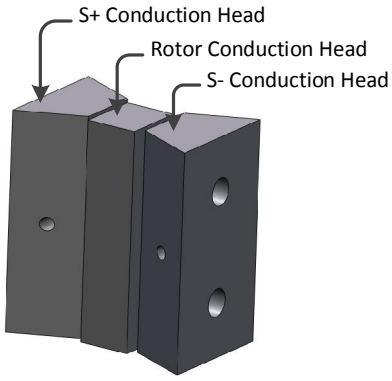

Figure 52 Conduction Heads

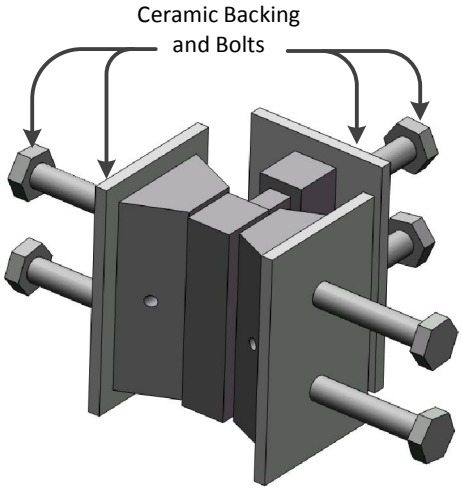

Figure 53 Conduction Heads with Ceramic Backing and Bolts

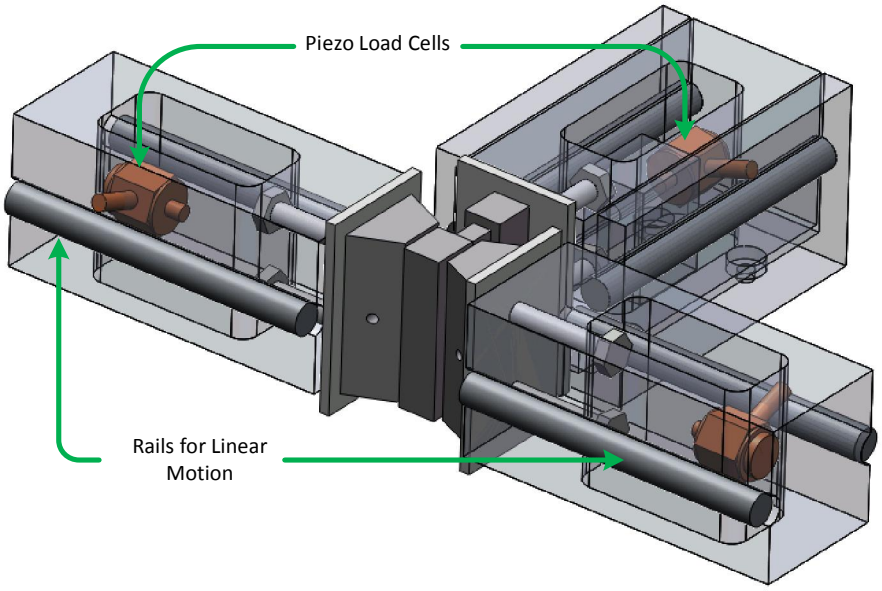

Figure 54 Relative Positioning of Conduction Heads, Rail Structure (transparent) and Load Cells

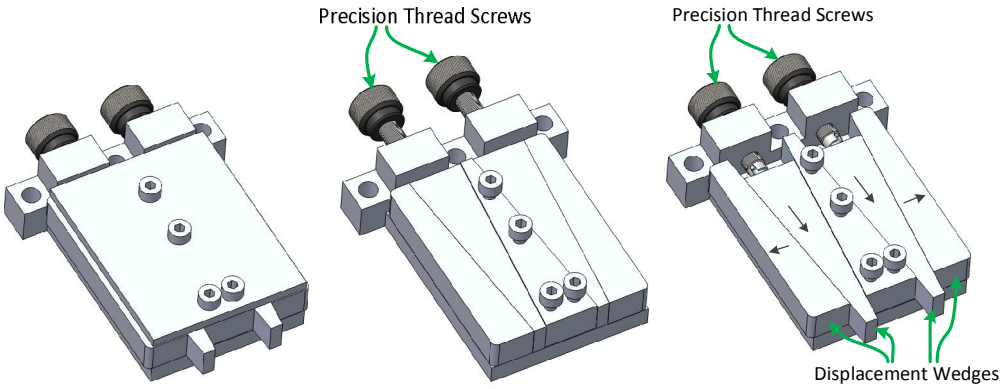

Figure 55 Displacement Wedge Assembly: Left – Assembly with Cap, Middle - Zero Displacement without Cap, Right- Full Displacement without Cap

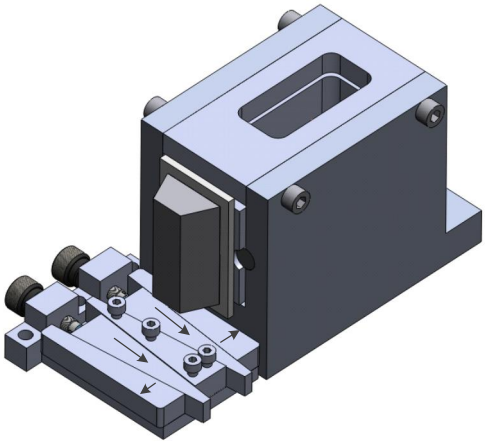

Figure 56 Displacement Wedge Pushing on Stator Slide Assembly

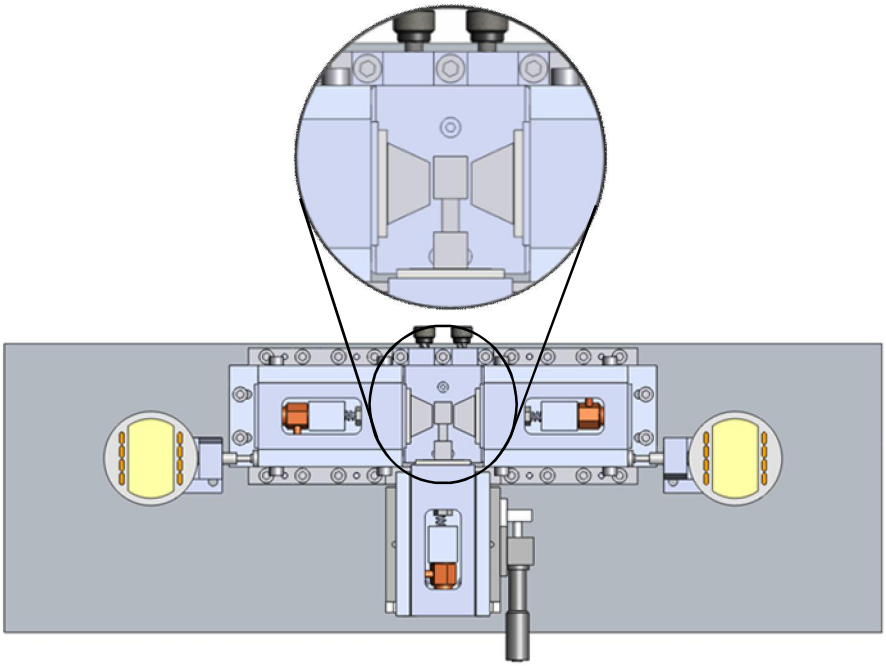

Figure 57 Top View of Linear Test Rig with Conduction Head Focus

4.3.2 Parasitic Capacitance

The linear rig is designed is to measure the normal and tangential forces due to a build-up of charge. Capacitance between the rotor and stator plates can be used to predict the force, however alternative paths around the rotor-stator air gap in which the electric field can develop and traverse will reduce the field and thus force. Although the components of the experimental rig are electrically isolated and utilize relatively large gaps between components to minimize stray fields, there will be some stray fringing that will reduce the useful field for force production. Figure 58 shows the physical model for this stray field and parasitic capacitances.

Figure 59(a) shows the electrical circuit for the test rig. In this model, C_{S+R} and C_{S-R} are inclusive of the air gap capacitance and coating capacitance shown in Figure 51. The model helps to illustrate the multiple paths that the field can traverse. Only C_{S+R} and C_{S-R} serve to produce force, thus all other capacitances represent parasitic fields which result in a reduction in force.

The value of the parasitic capacitance can be computed with relative ease if the stray capacitance to the base plate, noted by 'B', is transformed from a wye to delta connection as Figure 59(b) shows. $C_{\Delta Eq}$ is the equivalent parallel capacitance that does not contribute to C_{S+R} force production. Because the parasitic capacitances are composed of large air gaps, their capacitance values are relatively small and result in negligible effect so long as the rotor-stator gaps are significantly smaller. This is a design constrain for future SIM developers. In this case however the resulting values shown in (53) are based upon measurements of $C_{S+B} = 63pF$, $C_{S-B} = 63pF$, $C_{RB} = 60pF$, and $C_{S+S-} = 60pF$. Using the results of (53) permits Equation (54) to be solved for specific geometric conditions as needed.

$$C_{\Delta S+R} = \frac{\frac{1}{C_{S-B}}}{\frac{1}{C_{S+B}C_{RB}} + \frac{1}{C_{S+B}C_{S-B}} + \frac{1}{C_{RB}C_{S-B}}} = 20.3pF$$

$$C_{\Delta S-R} = \frac{\frac{1}{C_{S+B}}}{\frac{1}{C_{S+B}C_{RB}} + \frac{1}{C_{S+B}C_{S-B}} + \frac{1}{C_{RB}C_{S-B}}} = 20.3pF \quad \textbf{(53)}$$

$$C_{\Delta S+S-} = \frac{\frac{1}{C_{RB}}}{\frac{1}{C_{S+B}C_{RB}} + \frac{1}{C_{S+B}C_{S-B}} + \frac{1}{C_{RB}C_{S-B}}} = 21.3pF$$

$$C_{\Delta Eq} = C_{\Delta S+R} + \frac{(C_{S-R} + C_{\Delta S-R})(C_{RB}+C_{\Delta S+S-})}{(C_{S-R} + C_{\Delta S-R}) + (C_{RB}+C_{\Delta S+S-})} \quad \textbf{(54)}$$

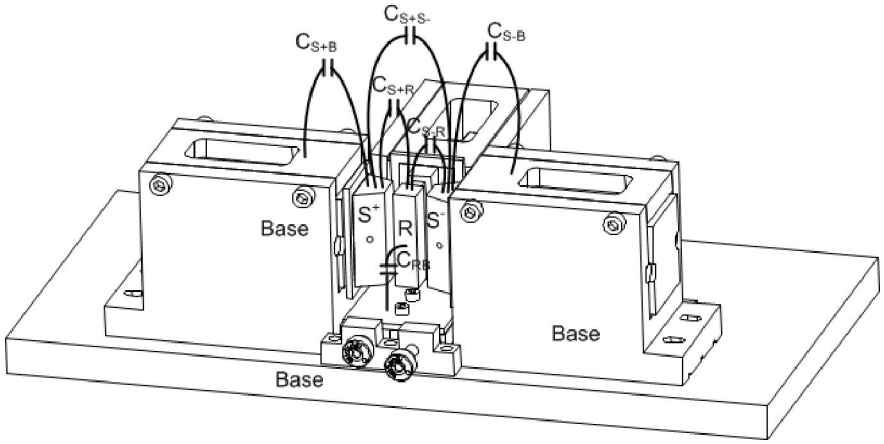

Figure 58 Physical Model of Parasitic Capacitances

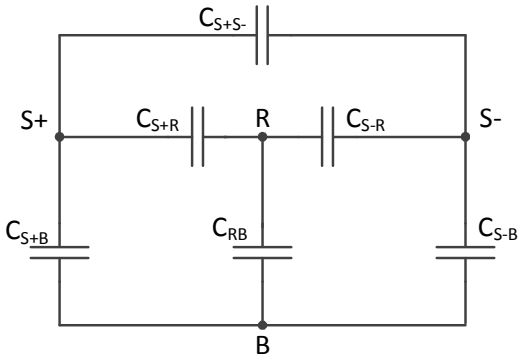

(a)

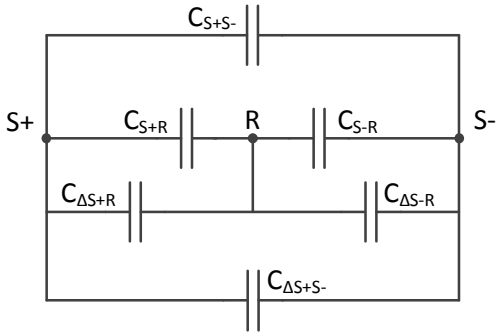

(b)

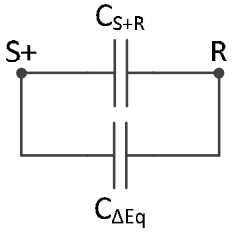

(c)

Figure 59 Electrical Diagrams with Parasitic Capacitance (a) Physical Model, (b) Equivalent Delta Model, (c) Equivalent Model

4.3.3 Linear Force Rig Experimental Setup

The physical rig is designed to isolate forces such that independent measurements of force can be made. Force is generated by applying a voltage between the two stator plates which places a charge and creates an electric field. The field then induces normal forces on the stator plates and a tangential force on the rotor plate. These forces are converted to electrical signals by the piezo load cells. The applied voltage and resulting three forces are shown on a four channel oscilloscope for recording.

Because force of the load cell is measured by the bending of a piezo crystal, it is necessary to condition and amplify the signal. Thus, each load cell was connected to a QSC 484-6 signal conditioner (amplifier) from Cooper Instruments. A block diagram of this setup is shown in Figure 60 and a photo of the experimental setup is shown in Figure 61.

Utilizing the Paschen curve data discussed previously as a guide to prevent breakdown, a family of curves describing the relation between force, gap and overlap for a given coating was created. Measurement of relative conduction head displacement was accomplished using two inductive Mahr® digital indicators with accuracies of ± 2nm. Measurement of the overlap was done using a Deltron® single axis micrometer positioning stage with positioning tolerance of 0.1mm which was ample for measuring overlap.

Because of the extreme precision of the Mahr indicators and piezo cells, minute vibrations could adversely affect the measurements. Thus, to minimize vibrations the test rig was placed upon a layer of acoustic board, rubber mat and common pile carpet which sat upon a bench that was supported by a bed of sand.

By measuring the capacitances between the stator and rotor plates the achieved or effective air gap could be calculated. Using bare plates (no dielectric in gap) the maximum C_{S+R} = 1.57pF and C_{S-R} =1.36pF. These equate to an effective gap of about 5µm. However, these values were rarely achieved, typical (easier to achieve) gaps of 18µm were more common during force measurement. Prior to each static position measurement, the capacitances were measured and used to compute the effective gap.

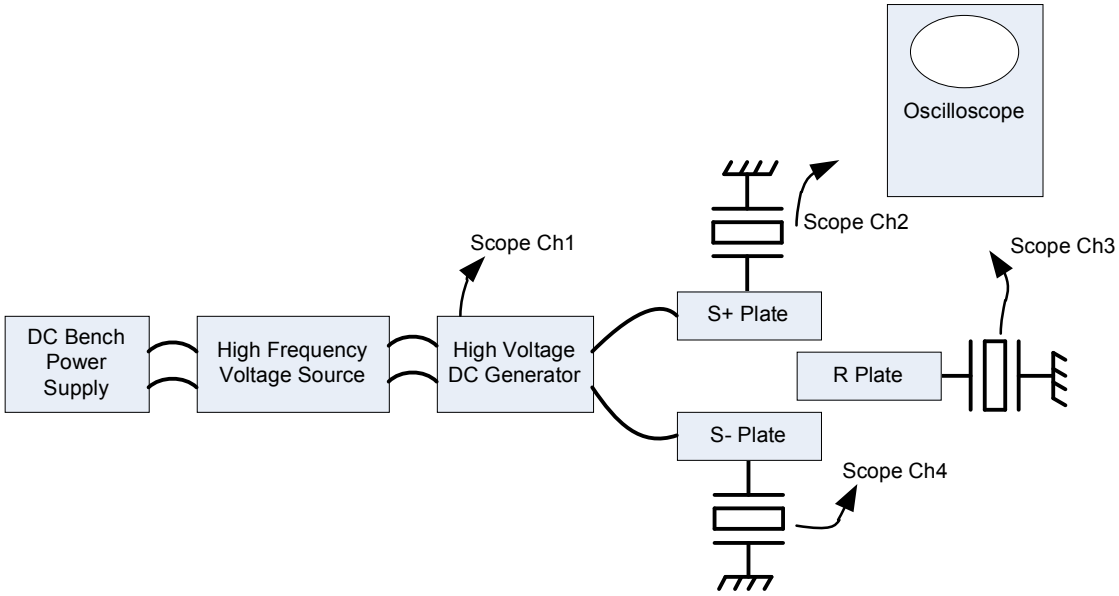

Figure 60 Linear Force Rig Block Diagram

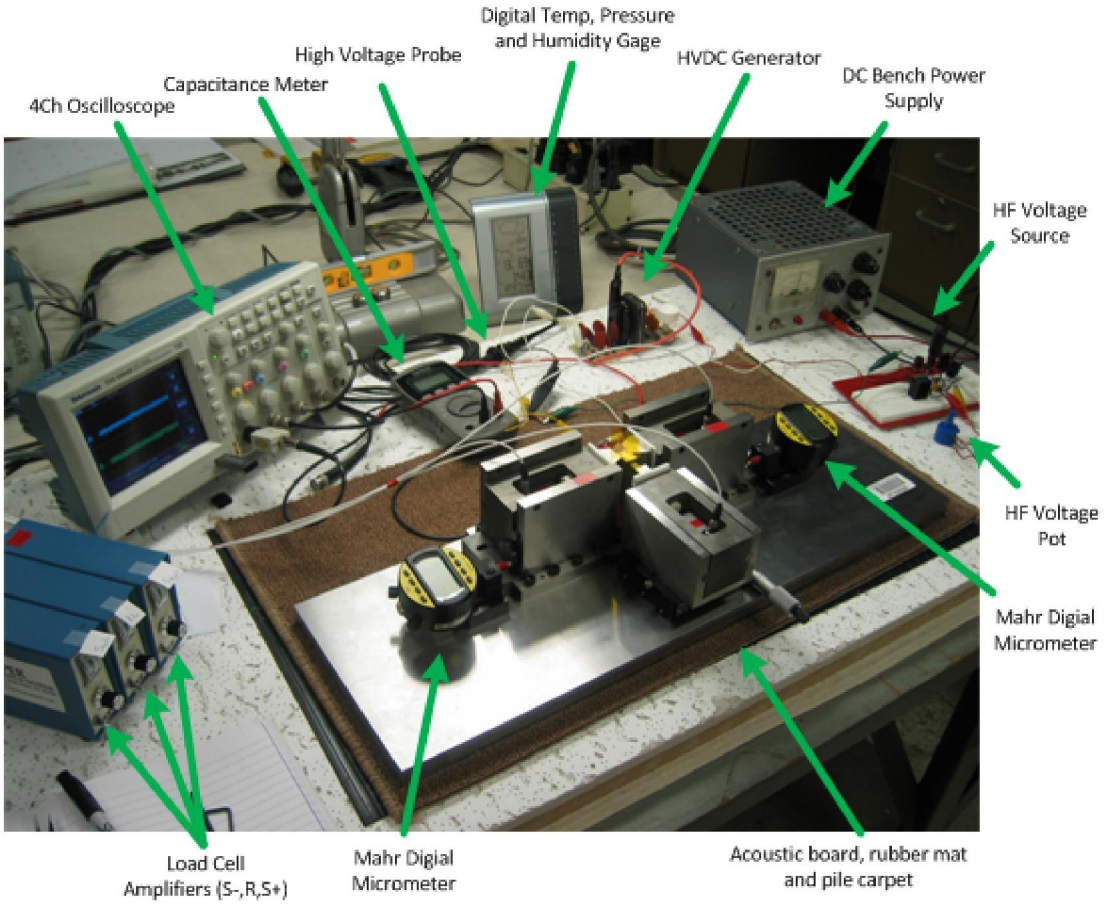

Figure 61 Actual Linear Force Rig Setup

4.3.4 Acquiring Force Measurements

Measurement of forces was accomplished by positioning the stator and rotor heads in a closed position such that the air gap is minimized and overlap is maximized. The digital indicators were then set to a 'zero' value. This relative physical positioning was used as the basis for future displacement measurements. The various capacitance values were then measured and used to compute the effective gap which was recorded. Once recorded, a voltage was applied to the stator plates and the resulting forces were read from a four channel digital oscilloscope. The gap was then expanded using the precision screw and wedge assembly until the proper displacement was read from the digital indicators and verified via capacitance readings. Once a desired gap was achieved, overlap between the rotor and stator was varied and recorded. This process was repeated until a family of curves was achieved. An example setting, with Kapton as the gap dielectric, is shown in Figure 62.

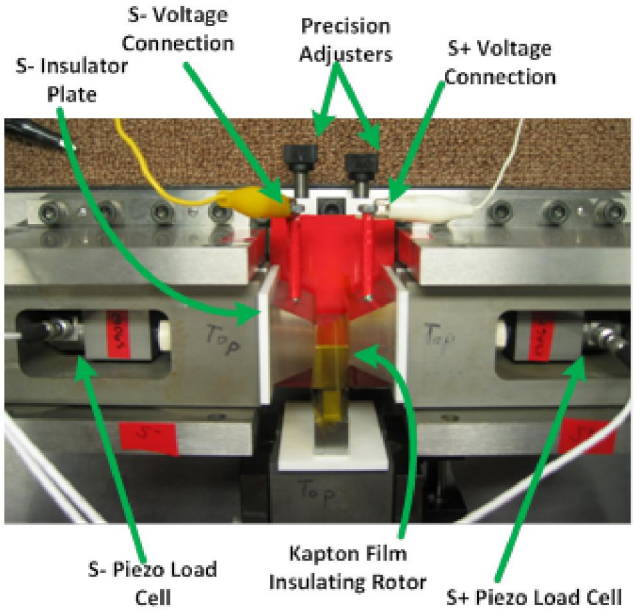

Figure 62 Conduction Heads with Kapton Dielectric

4.4 Analytic Model Validation

Direct measurement of capacitance and force has been made using the test rig. Comparison of these measurements and applied voltage to the analytic models developed in Chapter 3 along with finite element (FE) modeling was done to verify the models.

4.4.1 Finite Element Results

The stator and rotor plates described previously have been analyzed using finite element analysis for comparison. However, the vast differences in geometric scales between the gap and the rotor and stator plates have proven difficult to analyze. Based upon available computing power with 3GB of memory and utilizing the commercial software CosmosDesignSTAR® v4.5 only air gaps larger than 200µm were successfully analyzed at full scale. To achieve FE validation for smaller gaps, models with reduced thickness were created which permitted analysis of gaps of 25µm to be achieved with close comparison to the analytic models. The air gap in this analysis was a simple air gap and did not contain a dielectric. Figure 63 and Figure 64 show examples of these FE models with mesh.

Using FE analysis, models with air gaps of 25µm, 100µm and 200µm have been analyzed. These three air gaps have then been simulated at 1kV and 0.4kV with 0, 6.63, 13.3, 50, 80, 93.3 and 100 percent overlap. (These correspond to overlaps of 0mm, 1mm, 2mm, 7.5mm, 12mm, 14mm and 15mm for the specific model.)

Figure 65 through Figure 67 compare the FE and analytic calculation capacitance values. Figure 68 through Figure 70 compare the FE and analytic calculation values for the normal force. Figure 71 through Figure 73 compare the FE and analytic calculation values for the tangential force. These figures reveal a distinction between the computed and FE values, namely that they are dependent upon overlap of the rotor and stator and the gap size. The difference between the values is minimized when the overlap is maximized and the gap is minimized.

Comparison of tangential force values show a similar trend to that of capacitance and normal force with a percent difference below 10% until there is complete overall. When there is 100% overlap, the tangential force FE value drops quickly as there is no longer a leading edge to pull the rotor, an expected result due to the assumptions made while building the analytic model.

The FE analysis results show the trend that as the gap decreases and overlap increases the FE and analytic calculation values tend to align. In most cases, the percent different drops below 10% when alignment is above 50% which is expected due to the assumptions of fringing as presented in Chapter 3.

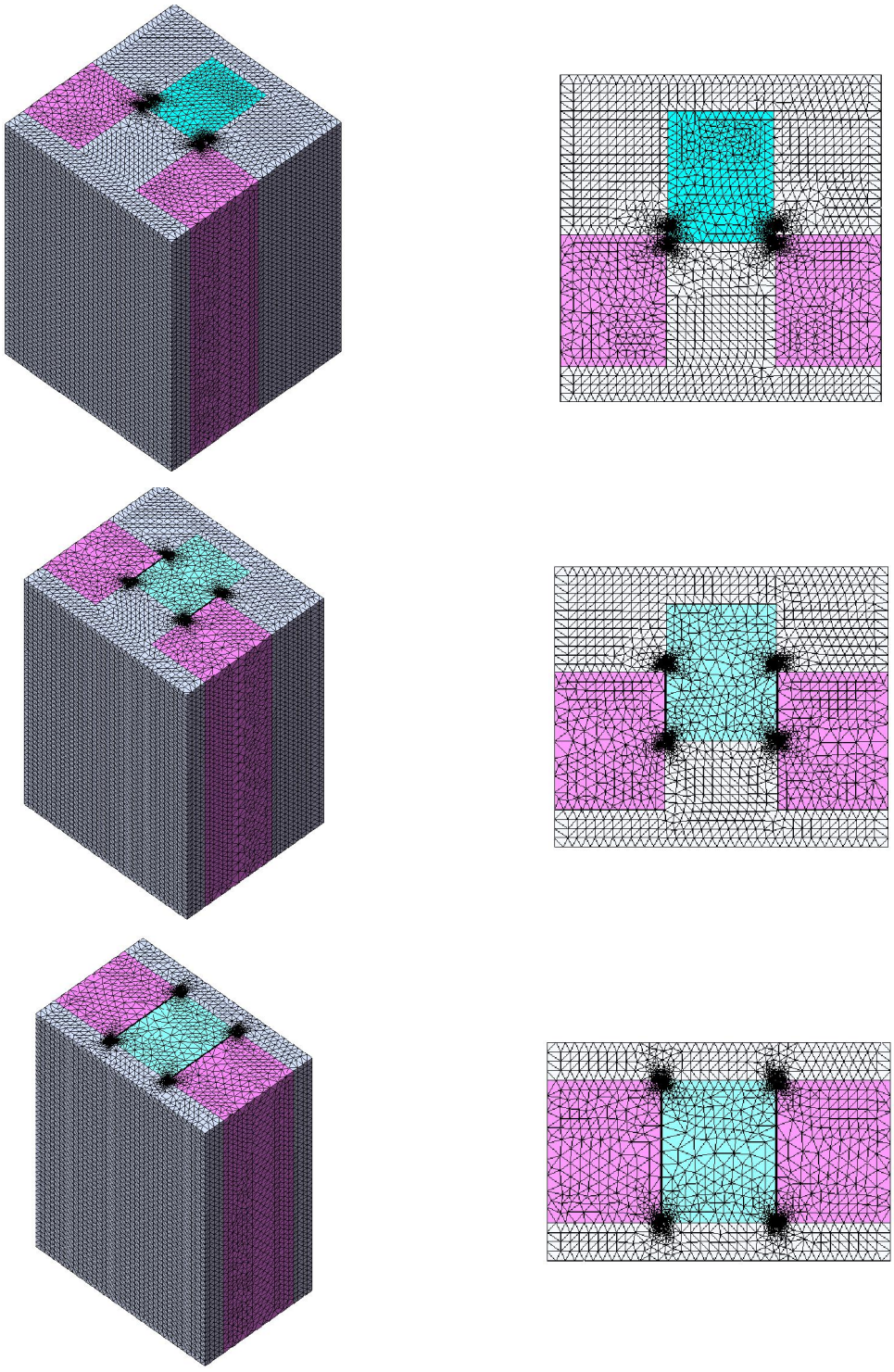

Figure 63 FE Mesh Examples for full 3D Models – 1%, 50% and 100% Overlap

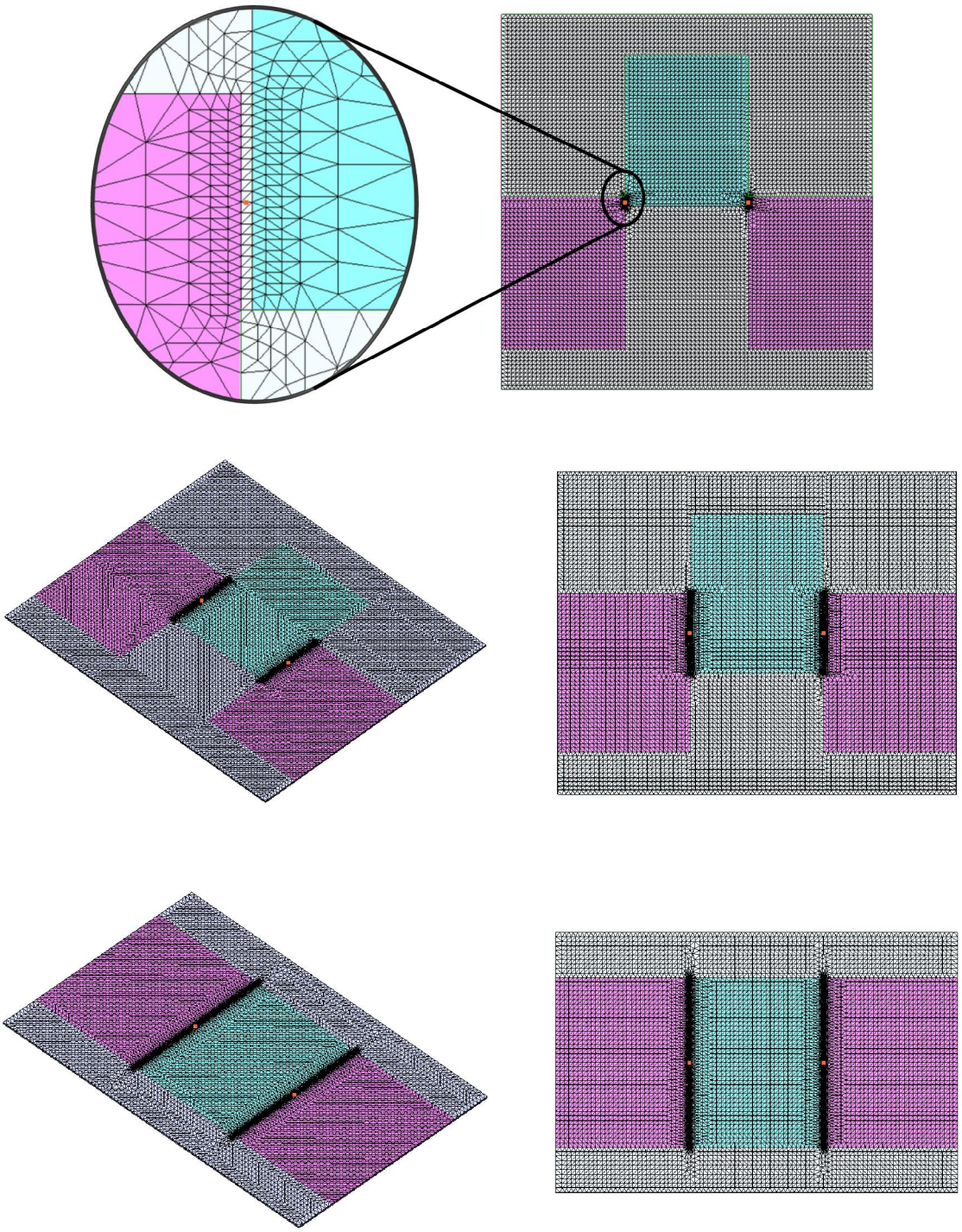

Figure 64 FE Mesh Examples of Reduced Thickness Models – 1%, 50% and 100% Overlap

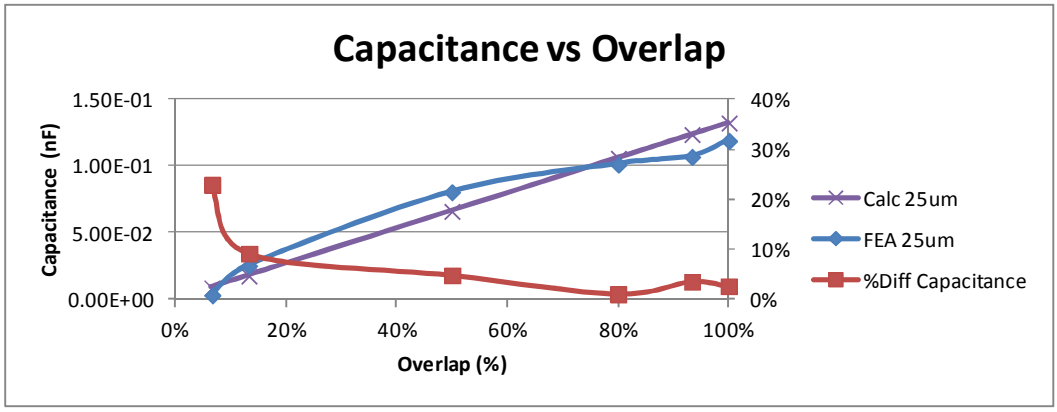

Figure 65 FEA vs Calculated Capacitance value at 25um

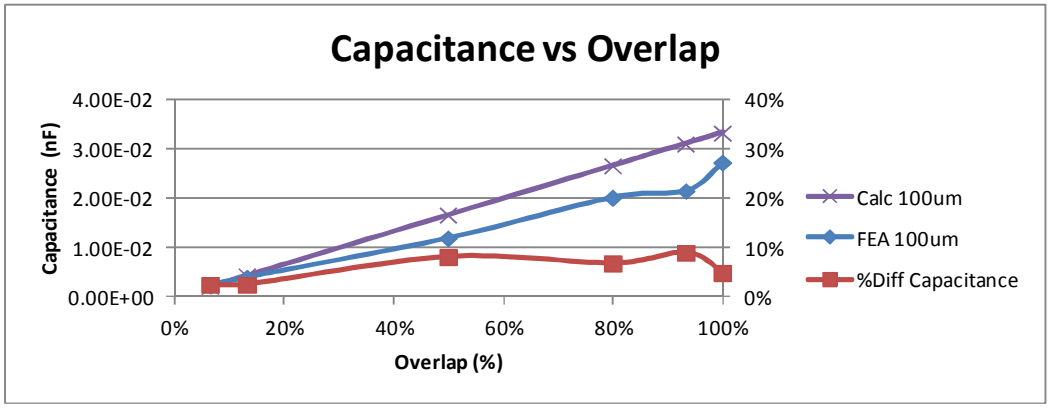

Figure 66 FEA vs Calculated Capacitance value at 100um

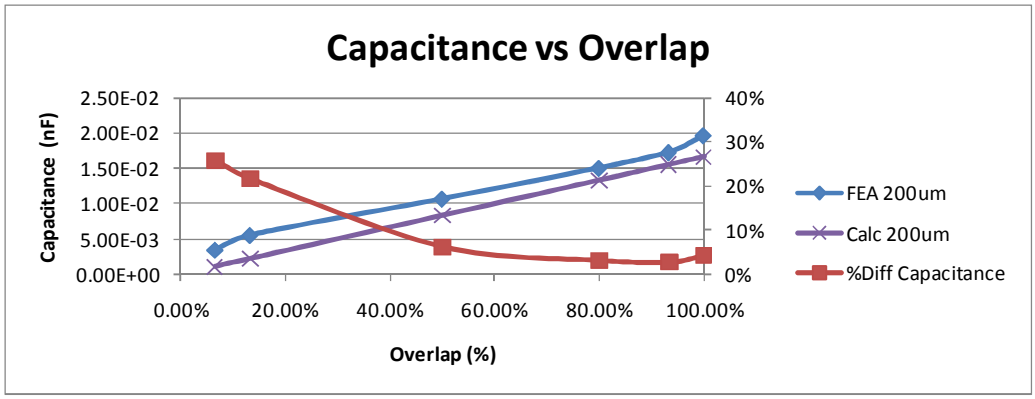

Figure 67 FEA vs Calculated Capacitance value at 200um

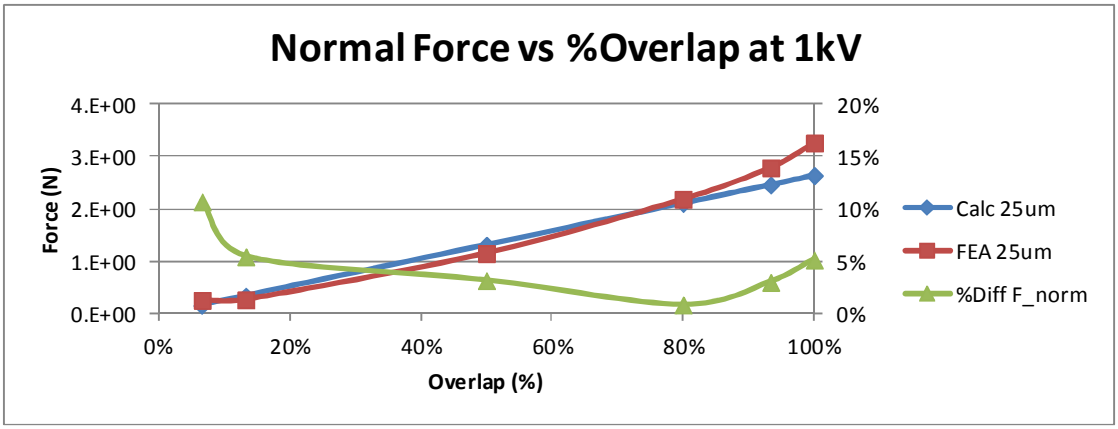

Figure 68 FEA vs Calculated Normal Force value at 25um

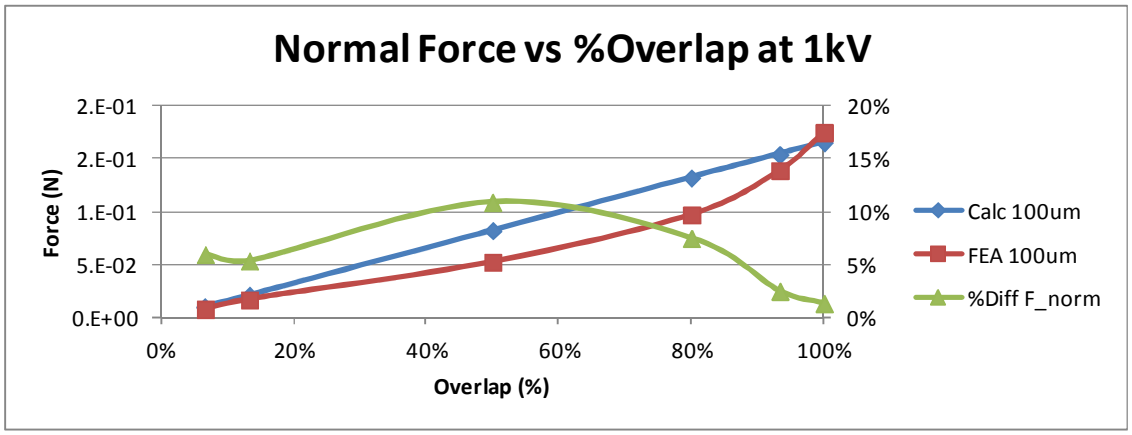

Figure 69 FEA vs Calculated Normal Force value at 100um

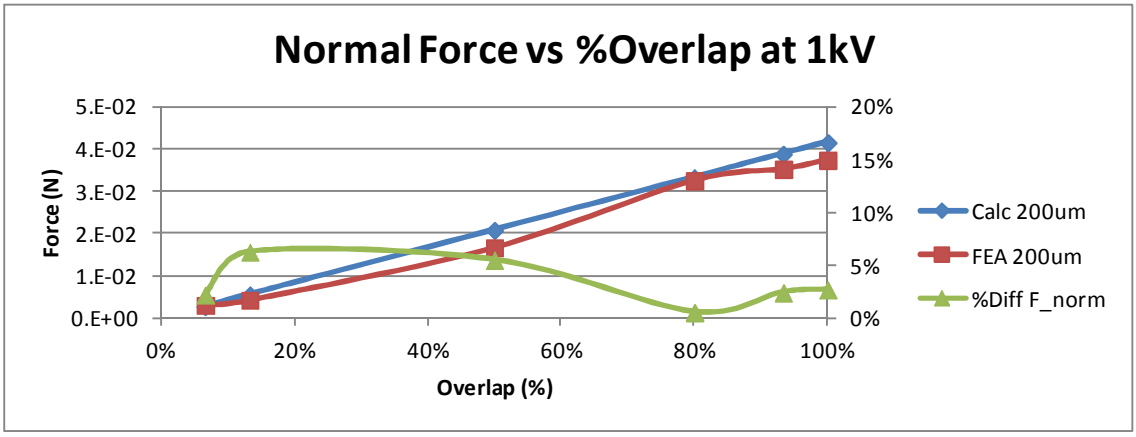

Figure 70 FEA vs Calculated Normal Force value at 200um

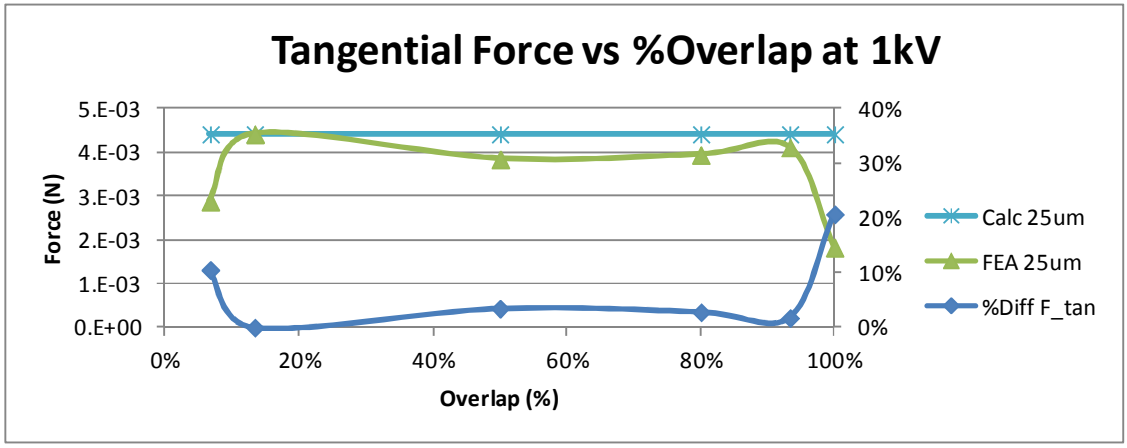

Figure 71 FEA vs Calculated Tangential Force value at 25um

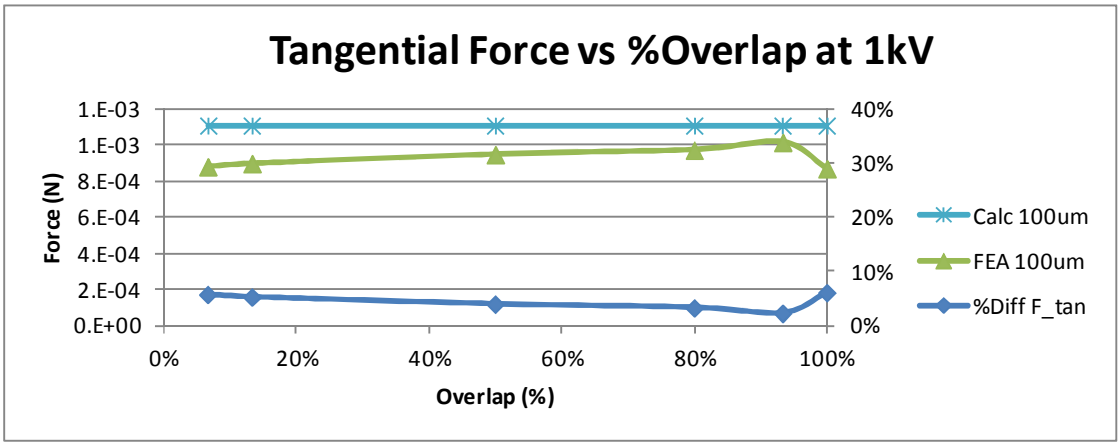

Figure 72 FEA vs Calculated Tangential Force value at 100um

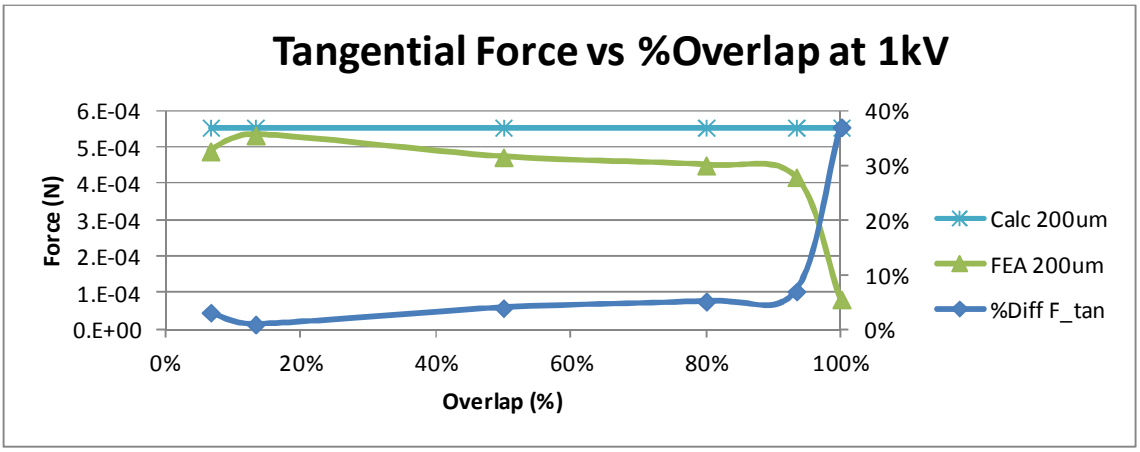

Figure 73 FEA vs Calculated Tangential Force value at 200um

4.4.2 Linear Force Test Rig Experimental Results

Figure 74 compares the experimental and calculated force vs capacitance values while Figure 75 compares the experimental and calculated force vs computed effective gap of HN30 at various overlaps. The figures show close agreement between the calculated and measured values for the capacitance range that was measured. Figure 76 and Figure 77 compares the experimental and analytic calculation values of HN30 at various overlaps for the tangential force vs capacitance and gap respectively. Figure 78 shows capacitance vs air gap for various overlaps and plots the maximum and minimum measured capacitance at the respective overlaps such that an understanding of the achieved air gap is made apparent. These three figures should be considered together.

Figure 78 shows capacitance vs air gap with the maximum and minimum measured capacitance values for the respective overlap conditions. The plot shows the minimum obtainable gap is roughly 16μm at 100% overlap, although slightly larger gap values were easier to achieve repeatedly. It is worth noting that higher capacitances (smaller gaps) could be achieved if the conduction heads were forcibly compressed, however, this resulted in a marked reduction of force. This reduced force value is due to the inability for the load cell to displace in response to an applied voltage.

Figure 79 shows the charge vs voltage plots for various overlap conditions. The plot is analogous to the flux vs current plots of induction machines. Note that unlike the flux plots of induction machines, the plots are linear as there is no saturation. This plot represents the operating envelop for a motor as it traverses from no overlap to full overlap and will be discussed further in Chapter 6.

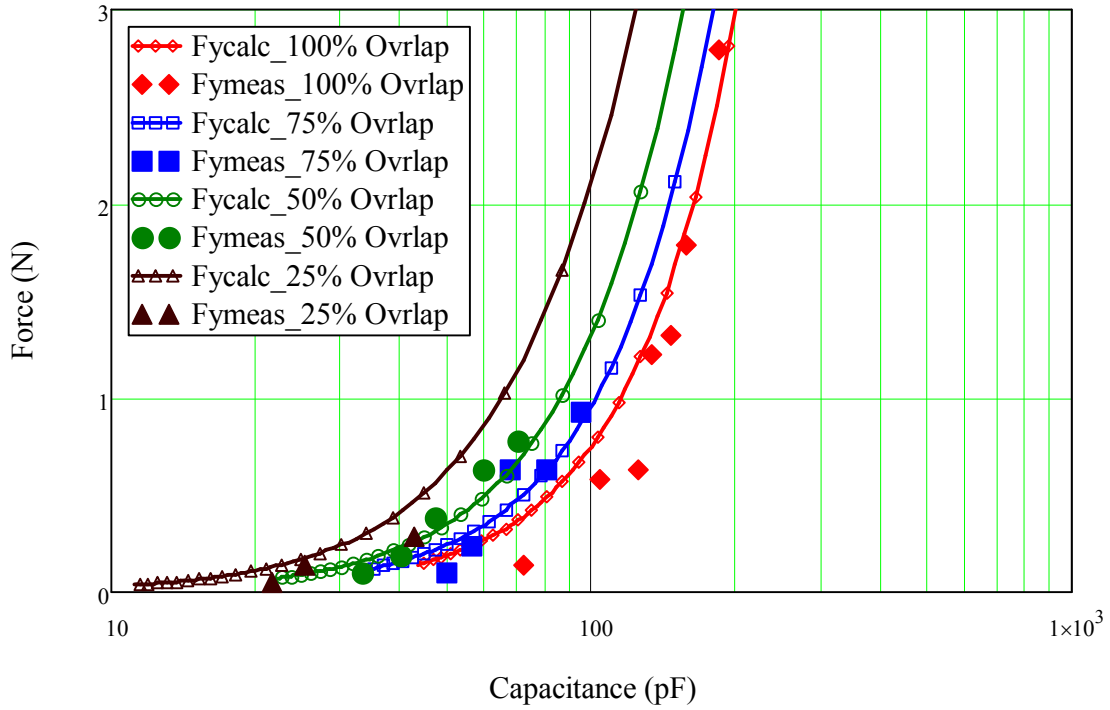

Figure 74 Normal Force vs Capacitance

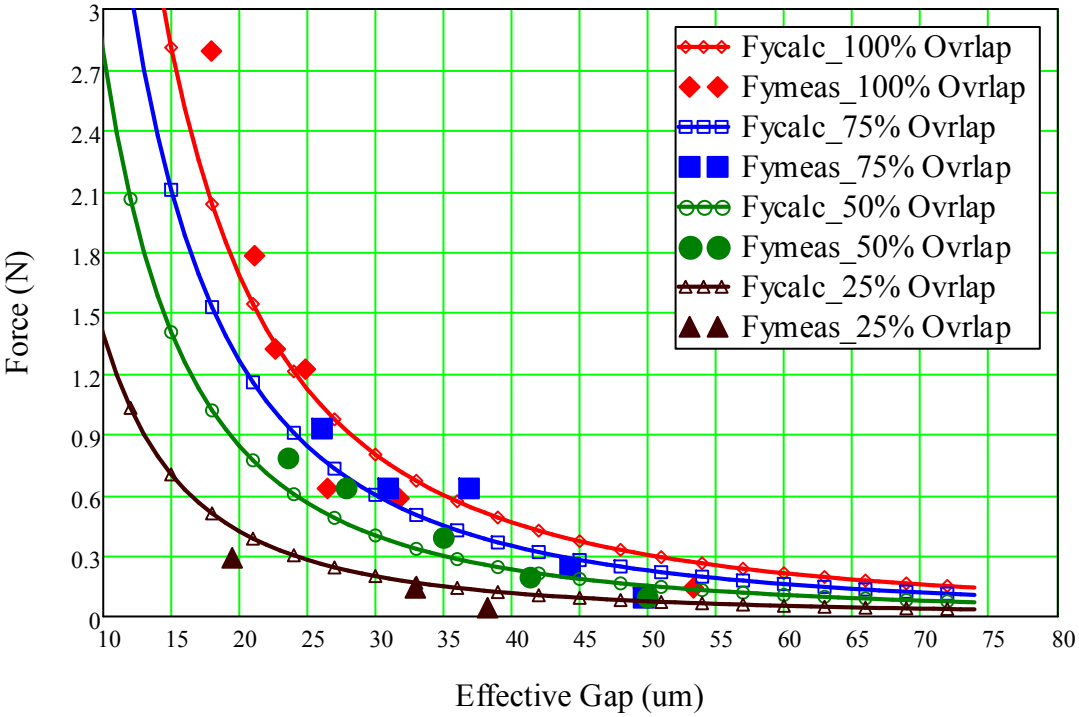

Figure 75 Normal Force vs Effective Gap

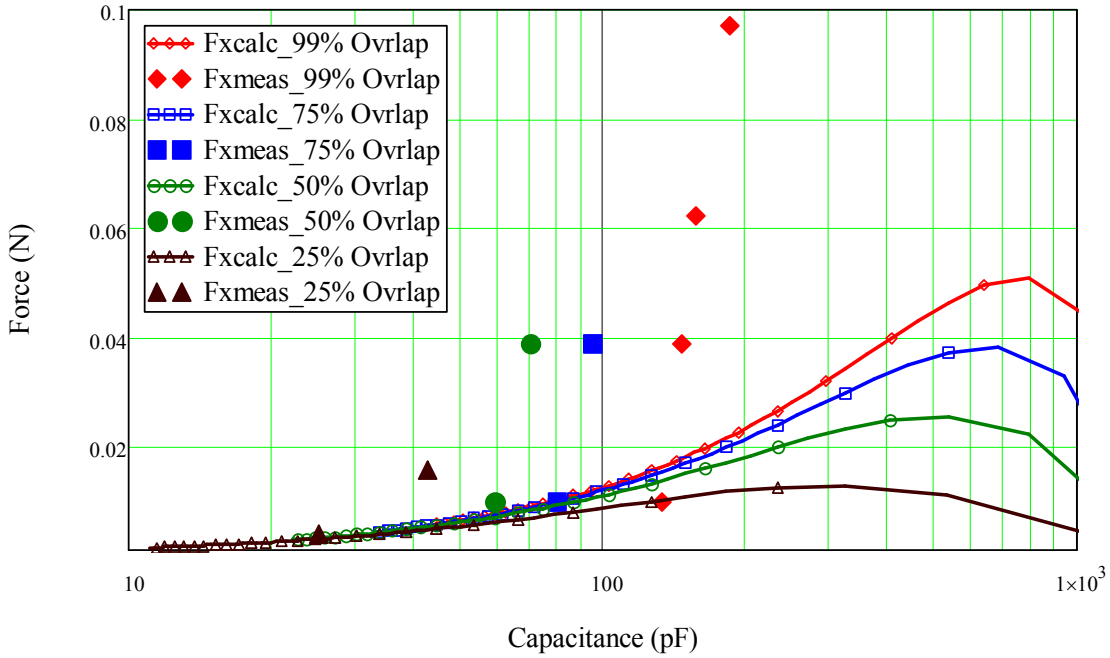

Figure 76 Tangential Force vs Capacitance

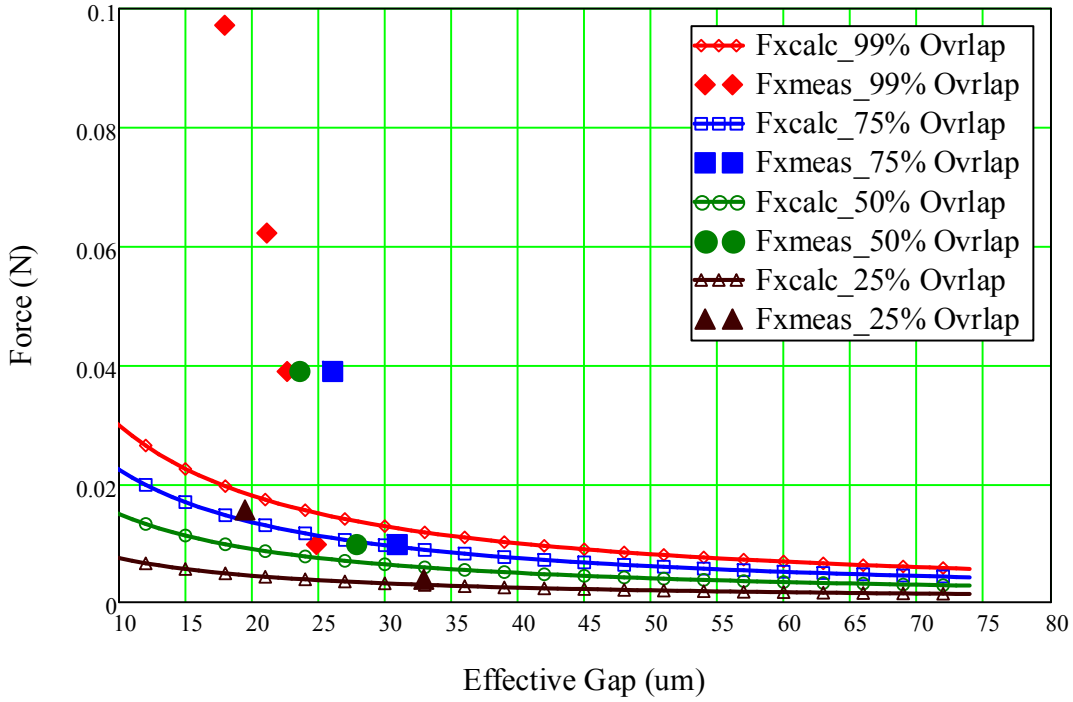

Figure 77 Tangential Force vs Effective Gap

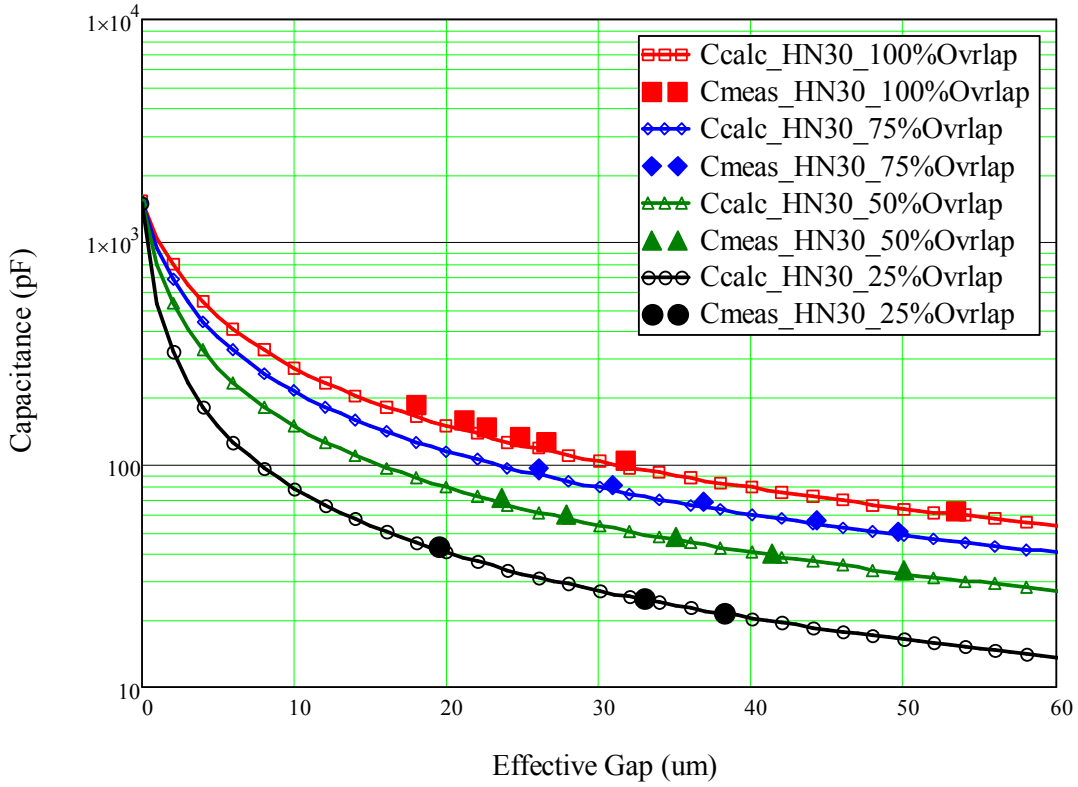

Figure 78 Capacitance vs Effective Gap

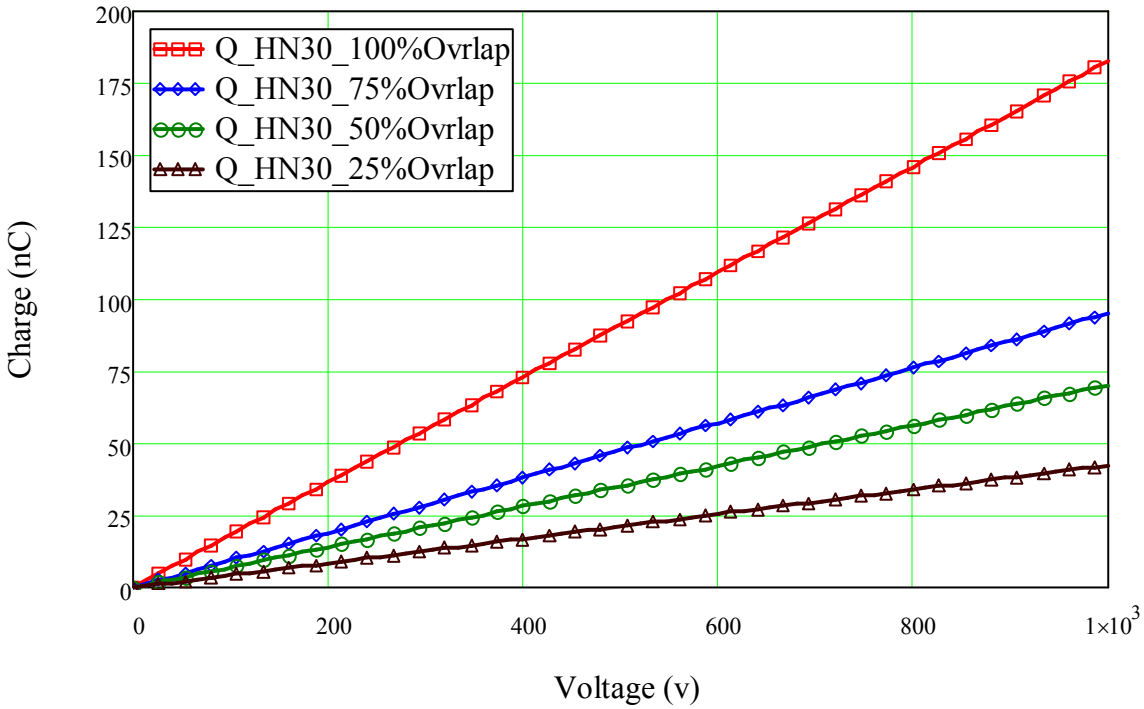

Figure 79 Computed Charge vs Voltage Profile

4.5 Experimental Limitations

Figure 76 and Figure 77 show large error and was inconsistent with the predicted results. A primary reason for this discrepancy lies with the physical test rig. The rig was designed to decouple the normal and tangential axial forces, however, this was not perfectly achieved with the rotor plate. The conductive rotor plate is connected via two ceramic screws, to insure electrical isolation. However, ceramic screws have a low torque limit and prevented perfect rigidity between rotor plate and the rotor mount. Because of the sensitivity of the system, minute vibrations were detectable, thus shifting of the rotor assembly when a voltage was applied resulted in a force measurement that was partially coupled to a stator. A reason for this it, when a voltage is applied, it produces force on the Kapton film, visually observable on occasion, due to flexing of the film from ions in small air gaps (pockets) between the film and the conduction head. Thus, the measured tangential forces for this system were due in part to a flexing film.

An *effective gap* rather than an *actual gap* must be considered due to the difficulty in obtaining an absolute or true zero positioning of the conduction heads. The difficulty arises for several reasons, namely an inability to measure contact with the Kapton film and an inability to obtain a true conformal surface with the film. While measures were taken to minimize dust to insure cleanliness of the film before application, it was improbably that all particulate matter was removed from the surface of the film. Because of particulate matter and any small crease in the film, small voids or other cavities between the film and conduction head inevitably occurred and prevented a perfect surface to surface bond between the film and conduction head. Because of this, perfect contact between the two surfaces, contact across the total surface area in a uniform manner was unlikely. However, considering Figure 78 and the close relation between the gap value computed from the measured capacitance vs the analytically computed gap value, the surface imperfections are shown to be small.

This experimental rig has shown several issues that need to be solved for successful future designs. Namely, a true dielectric boundary layer that is bound directly to a conducting surface, thus preventing any shifting, should be used in future designs. While known at the outset, this rig design has reinforced the need for extreme rigidity of the substrates supporting the conductive surface and dielectric coatings.

4.6 Conclusion

The development of experimental tests to validate the analytic models was presented in this chapter. To validate force models, knowledge of the achievable Paschen curves were empirically measured to plot breakdown voltage vs gap at 1atm. These tests were conducted with the dielectrics zirconium dioxide and Kapton. The ZrO_2 coating proved difficult to create and showed results below that of Kapton. The section concluded with a comparison between the empirically achieved electric and magnetic Maxwell stresses as mentioned in Chapter 1. Based upon the experimental Paschen rig results, it was shown that it is possible to exceed the stress of a magnetic system fields in a macro system with air gaps below 10µm using a dielectric to prevent an avalanche breakdown.

This Chapter also detailed the design and analysis of a linear force test rig to validate force models. This section began with a discussion of the construction and theory of operation of the force rig and continued with a detail of the experimental setup. Using the experimental force results, this chapter concluded with comparisons between predicted and experimental force values which showed close agreement. The comparisons were made using FE models and experimental results using the linear rig. The linear rig results also showed close agreement with the predicted values in all but measurement of the tangential force which fell below the inherent physical limitations of the system.

These tests have highlighted a number of issues that will need to be addressed in future designs. The linear force test rig has shown the difficulty in measuring the maximum tangential force due to an inability to completely decouple the component forces. Additionally, the FE analysis has shown that full scale modeling of micro coatings and gaps with significantly larger substrate components is challenging and may require specialized routines to address the disproportionate geometric scales.

The previous chapter presented empirical Paschen curves showing the obtainable field strengths for micron level air gaps. These curves were then used as a base line to validate analytic SIM models using FE analysis and empiric tests of a linear static rig. Using the validated models, design of a rotational dynamic SIM is now presented. Dynamic simulations of the designed motor will be presented in the next chapter.

Chapter 3 Equation (50) gives the force of a linear electrostatic system. By converting this equation to a cylindrical coordinate frame, an equation describing the forces of a simple two plate rotational system can be formed and is given below in Equation (55) and Figure 80. Note that a SIM with symmetric design, i.e., with two stator poles on opposite sides of the rotor, will develop symmetric forces. Symmetric force development means that the net normal force on the rotor will be zero as the forces are in opposite directions, while the net tangential force will be twice that shown in (55). In (55) r_{in} and r_{out} are respectively the inside and outside radius of the plate, θ_{Ovr} is the angle of overlap between the rotor and stator plates, z_{gap} is the gap between the plates (along the z-axis) and ε is the combined relative and free space permittivity.

$$\overrightarrow{F_{ES-Rotation}} = \left(\frac{\varepsilon \cdot ln\left(\frac{r_{out}}{r_{in}}\right)}{2}\frac{V^2}{z_{gap}}\right)a_\theta + \left(\frac{\varepsilon \cdot (r_{out} - r_{in}) \cdot \theta_{Ovr}}{2}\frac{V^2}{{z_{gap}}^2}\right)a_Z \quad \textbf{(55)}$$

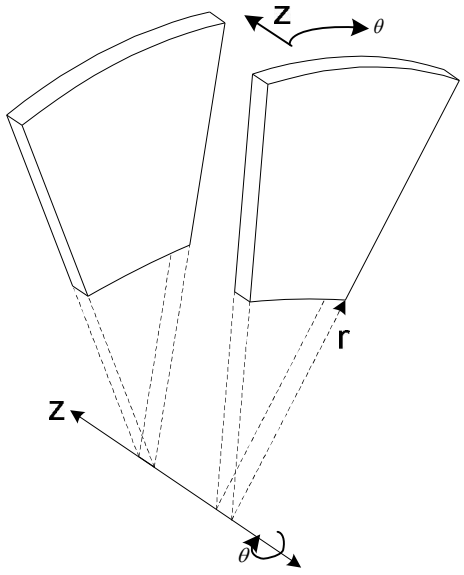

Figure 80 ES Force Diagram of Rotational Plates

As is seen in Equation (55), the respective *z* and θ-component forces are proportional to the square of the voltage and plate length *r* and inversely proportional to the gap distance (z_{gap}). As expected, these characteristics maximize a capacitor value as given in Equation (15).

5.1 Expanded Breakdown Envelope

Experimental results from Chapter 4 have shown the feasibility of a SIM that operates with a modified Paschen curve, one that includes a plateau region, thus allowing improved field strengths to be achieved. Figure 81 shows the expanded breakdown envelope for HN25, although similar expanded envelopes for HN50 and HN100 could also be created.

It is worth restating that while thicker films allow higher breakdown voltages the goal of the SIM designer is to maximize the electric field while minimizing the applied voltage, which requires a minimal gap size for achievement. Figure 47, shown previously, highlights the near equality of the various Kapton film thicknesses to achieve the same field strengths, although the thinner films allow this field to be achieved with a lower voltage.

Maximizing the voltage of the gap, allows the maximum electric field to be developed, which then helps to maximize force. It is the voltage of the gap that is to be maximized, not the applied voltage that is of critical importance. For this reason, dielectrics of maximum strengths should be sought. The ultimate goal of the SIM designer is to economically achieve the highest field strength from the lowest applied voltage within a mechanical structure and system that can maintain the desired gap within a nominal tolerance.

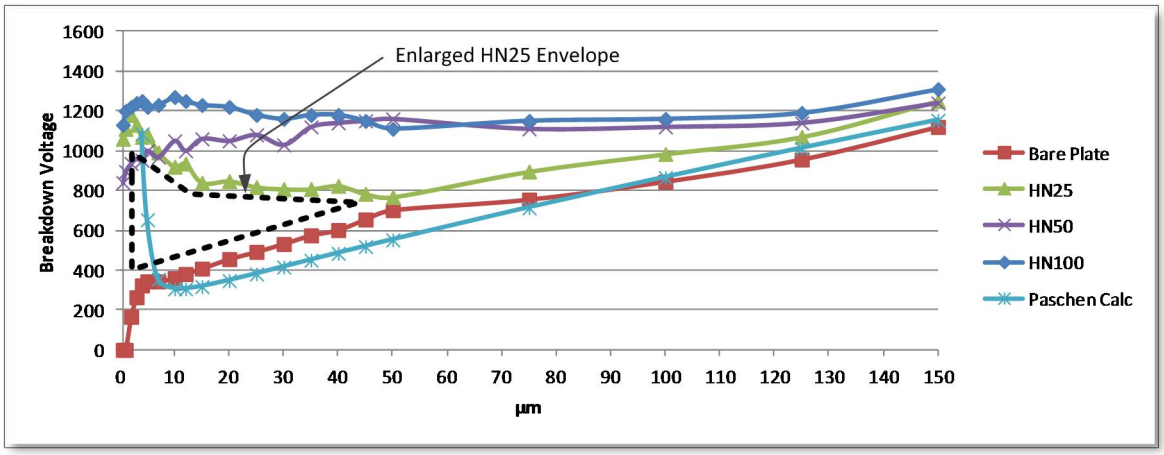

Figure 81 Enlarged HN25 Operating Envelope

5.2 Linear vs Sinusoidal Capacitance Variation

Due to his limited control methods, Trump was limited to sinusoidal designs (see the exposed plates in Figure 13), or designs that resulted in sinusoidal capacitances, voltages and currents. By utilizing modern switching techniques that allow for square wave voltage patterns to be utilized, improved densities may be achieved over Trump's AC designs. Equations (56)-(58) show that a linear square wave pattern results in a density of $\sqrt{2}$ times that of sinusoidal.

$$\frac{dC_{Sin}}{d\theta} = \frac{d}{d\theta}\sin(\theta)\Big|_{RMS} = \frac{1}{\sqrt{2}} = 0.707 \quad \textbf{(56)}$$

$$\frac{dC_{Lin}}{d\theta} = \frac{d}{d\theta}\theta\Big|_{RMS} = 1 \quad \textbf{(57)}$$

$$\frac{Linear}{Sinusoidal} = \sqrt{2} = 1.414 \quad \textbf{(58)}$$

Equation (58) shows the ratio of RMS power for sinusoidal and linear plate designs. Because the ratio is greater than one, it is shown that a linear design provides greater power throughput than a sinusoidal one. The importance of this is that modern solid state switches allow for pulse width modulation (PWM) of sources, which provides improved flexibility and control schemes.

5.3 SIM Electro-Mechanical Relations

Using the rotational plate design as shown in Figure 80, electro-mechanical relations can now be developed. Through the establishment of an electric field, via charge placement, electrical energy may be converted to useful mechanical energy through Coulombic forces. These energies may be defined by first considering the instantaneous power (*P*) of the system, shown in Equation (59).

$$P = vi = v\frac{dq}{dt} \quad \textbf{(59)}$$

Power is the rate at which energy is transmitted. If linearity of charge is assumed, the electrical energy (W_{Elec}) stored in the capacitor plates at time *t* is given by the general integral of (60) and by (61). A linear relation between charge and energy, as presented earlier, is a good assumption so long as the electric field is below the field breakdown of the surrounding medium.

$$W_{Elec} = \int_{t_0}^{t} P\,dt = \int_{t_0}^{t} (v\frac{dq}{dt})dt = \int_{q_0}^{q} v\,dq \quad \textbf{(60)}$$

$$W_{Elec} = \int_{q_0}^{q} \frac{q}{C} dq = \frac{1}{2C}[q(t)^2 - q(0)^2] \quad \textbf{(61)}$$

If Equation (60) is rewritten to solve for the coenergy of the system (i.e., expressing the integral in terms of voltage rather than charge), then a more convenient expression may be found.

$$W_{Coenergy} = \int_{v_0}^{v} q\, dv = \int_{v_0}^{v} (Cv) dv = \frac{1}{2} Cv^2 \quad \textbf{(62)}$$

Coenergy is a mathematical expression for energy that is not stored in the electric field of the gap. Rather than being stored in the field, it is the energy that is converted to mechanical energy as force and/or torque. Assuming linear material properties, Equation (62) shows that only half of the input energy is available for mechanical purposes (the coenergy), while the other half stays within the field. A pictorial relation of energy and coenergy is shown in Figure 82 on page 86.

Energy of a mechanical system is called *work* and is defined is by the product of force (*F*) and distance (*x*). A differential amount of work may then be expressed as the product of a force with a differential change in distance, as shown in Equation (63).

$$dW_M = F \cdot dx \quad \textbf{(63)}$$

Mechanical power is the amount of work done per unit of time, or the time rate of change of work and can then be expressed as the product of force (*F*) and velocity (*v)* as shown in Equation (64).

$$P_M = \frac{dW_M}{dt} = F\frac{dx}{dt} = Fv \quad \textbf{(64)}$$

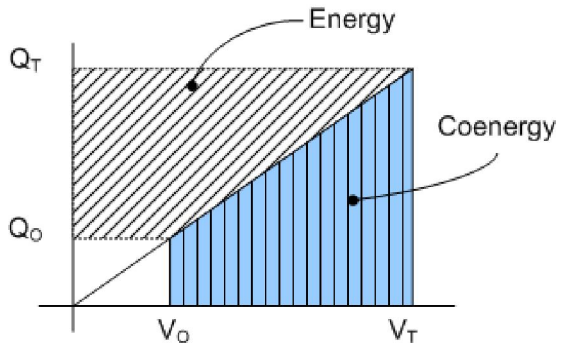

Figure 82 Energy - Coenergy Relation

If the torque of the motor t_{Mtr} is now defined as the cross product of force and distance, as shown in Equation (65), then a new expression for differential work and mechanical power may be written in terms of torque.

$$t_{Mtr} = F \times r \tag{65}$$

$$dW_M = F(r\, d\theta) = T d\theta \tag{66}$$

$$P_M = \frac{dW_M}{dt} = t_{Mtr}\frac{d\theta}{dt} = T\omega\ \frac{rad}{sec} \tag{67}$$

Now, solving Equation (66) for torque and setting mechanical work (energy) equal to the energy of the capacitor, allow for a relation between torque, charge, voltage and position to be revealed. This relation is shown in (68).

$$\begin{aligned} t_{Mtr} = \frac{dW_M}{d\theta} = \frac{dW_C}{d\theta} &= \frac{d}{d\theta}\left[\int_{v_0}^{v} q(\theta, v)dv\right] \\ &= \frac{\partial}{\partial\theta}\left[\int_{v_0}^{v} q(\theta, v)dv\right] \\ &= \int_{v_0}^{v}\left[\frac{\partial}{\partial\theta}q(\theta, v)\right]dv \\ &= \int_{v_0}^{v}\left[\frac{\partial q(\theta, v)}{\partial\theta}\right]dv \end{aligned} \tag{68}$$

The partial differential equation and integral of Equation (68) can be approximated for ease of analysis. This final form is shown in Equation (69).

$$t_{Mtr} \approx \sum \frac{\Delta q}{\Delta\theta}\Big|_{v=constant} \tag{69}$$

The total charge on the SIM capacitor plates will be a function of the applied voltage and rotor position. This relationship can be determined by considering the current of a capacitor when the capacitance is a function of angular position. To do so, Equation (15) is rewritten such that charge (q) is $q = Cv$ then expanded to show the relation of capacitance to position. This is shown in (70).

$$\begin{aligned} i = \frac{dq}{dt} = \frac{d(Cv)}{dt} = C\frac{dv}{dt} + v\frac{dC}{dt} &= C\frac{dv}{dt} + v\frac{dC}{d\theta}\frac{d\theta}{dt} \\ &= C\frac{dv}{dt} + v\omega\frac{dC}{d\theta} \end{aligned} \tag{70}$$

In (70) $\omega = \frac{d\theta}{dt}$ and ω is the angular velocity of the rotor and θ is the angular position of the rotor. This SIM capacitance current equation has two terms. The first term ($C\frac{dv}{dt}$) gives the traditionally known current of a capacitor, one that has a fixed capacitance. The second term, with which we are most interested for electrostatic machinery, is ($\omega v\frac{dC}{d\theta}$), which gives a current value that is proportional to the speed of the rotor. The second term may be called the *speed current* and represents a current source. This relation and equivalent circuit diagram are given in Equation (71) and Figure 83.

$$i_{Ph} = C\frac{dv}{dt} + v\omega\frac{dC}{d\theta} = i_C + i_\omega \tag{71}$$

It is worth noting that, as speed increases, an ever increasing amount of current will be going to the speed current, meaning less current (and thus less charge) is available for developing Coulombic force. A similar process occurs with induction machines wherein the motor's terminal voltage drops with increased speed.

As most power supplies are defined by voltages, it may be easier to understand when Equation (71) is expressed in terms of an applied voltage. To write (71) in terms of a voltage a small resistance known as an equivalent series resistance, R_{ESR}, may been assumed such that a phase current, i_{Ph}, may be defined. (R_{ESR} is representative of line resistance, which may be small, but not zero.) This phase current may now be defined in terms of voltage and resistance using Ohm's Law and Kirchhoff's current law as shown in Equation (72). This equation is then used to redefine (71) with a voltage source, as expressed in (73).

$$i_{Ph} = \frac{V_{Ph} - V_C}{R_{ESR}} \tag{72}$$

$$V_{Ph} = R_{ESR}(i_C - i_\omega) + V_C = R_{ESR}C\frac{dv_C}{dt} - v_C\omega R_{ESR}\frac{dC}{d\theta} + V_C \tag{73}$$

With the addition of a mechanical load, a complete single phase SIM model can be created and is shown in Figure 84.

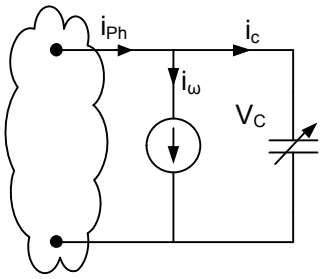

Figure 83 Single Phase SIM Equivalent Electrical Circuit

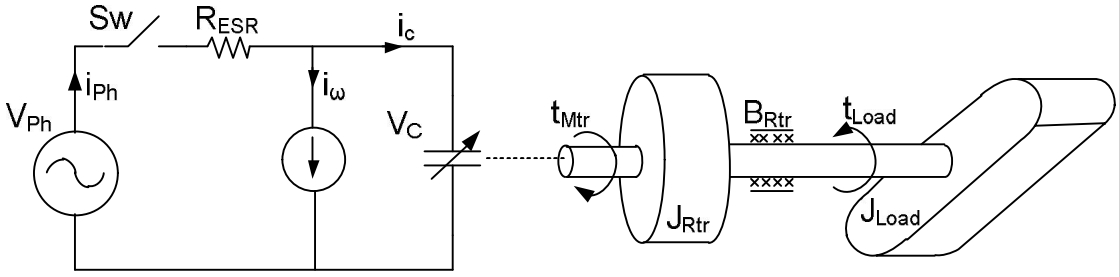

Figure 84 Single Phase Free Body Diagram of SIM

In Figure 84, t_{Mtr} is the developed torque of the motor, B_{Rtr} is the friction of the rotor and is inclusive of all friction sources including bearing and windage. J_{Rtr} and J_{Load} are the inertia of the rotor and load due to their mass and t_{Load} is the torque required to rotate the load. For operation of the mechanical motor, the electrical power source must develop a torque in the SIM to overcome all of the mechanical impedances including friction, inertia and loading. The torque of the motor can now be defined in terms of mechanical constraints, as shown in Equation (74).

$$t_{Mtr} = (J_{Rtr} + J_{Load})\dot{\omega} + B_{Rtr}\dot{\theta} + t_{Load} \quad \textbf{(74)}$$

From conservation of energy principals, a change of electrical energy will be equal to the sum of the change of field energy and the change of mechanical energy. This sum is equivalent to the sum of the change of field energy and the product of torque and the change in angular position, as shown in Equation (66). This allows for a third equivalent expression to describe the torque of the motor. This equivalent third form is shown below in (76). These relations are shown below.

$$\Delta W_{elec} = \Delta W_{field} + \Delta W_{Mechanical} = \Delta W_{field} + t_{Mtr}\Delta\theta \quad \textbf{(75)}$$

$$t_{Mtr} = \frac{\Delta W_{elec} - \Delta W_{field}}{\Delta\theta} \quad \textbf{(76)}$$

In industry, operation of common machinery typically requires rotational force whose measurement is torque. Torque is a direct function of force (F), given in Equations (77) and (78), where r is a radial distance upon which the force is applied. That force is then a function of the applied voltage (V), area of overlap (A_{ovr}) and phase air gap distance (d).

$$\vec{T} = \vec{F} \times \vec{r} \tag{77}$$

$$P_{Mech} = s \cdot T \tag{78}$$

Reviewing Equations (79) and (80) reveals a potential disproportion between the two forces. The tangential force, or theta force ($\vec{F}_{\theta}$), is that which will produce torque, while the normal force, the force acting normal to the rotor and stator plates and extending into the air gap ($\vec{F}_{gap}$), may present a material challenge due to its achieved values with micro gaps and large voltages.

$$\overrightarrow{F_{\theta}} = \frac{1}{2}\varepsilon \cdot ln\left(\frac{r_{out}}{r_{in}}\right)\frac{V^2}{d_{gap}} \tag{79}$$

$$\overrightarrow{F_z} = \frac{1}{2}\varepsilon \cdot (r_{out} - r_{in})\theta_{Ovr}\left(\frac{V}{d_{gap}}\right)^2 \tag{80}$$

5.4 Mechanical Constraints

The SIM has many potential advantages over traditional induction motors. One primary advantage being the potential for lower weight due to the fact that the SIM lacks the dense copper coils and iron yoke required in an induction motor. However, the SIM may require a tight tolerance on the gap to insure that it performs at a known operating point. Several mechanical issues hinder the gap tolerance and are discussed below.

5.4.1 Material Options

Unlike induction machines, SIMs only need a conducting surface for operation. Although only large gross plate designs are considered here, the conductor of the SIM could be a simple surface coating, such as conductive paint or monolayer on a rigid backing. However, with this approach the adherence between the backing and conductive surface must be able to withstand the normal force to prevent the coating from pealing. If this issue could be economically overcome, SIMs could be constructed of ceramics, glass or some composite materials. With this vast increase in material options, it is easy to conceive of SIMs that are significantly lighter than their induction motor counterpart.

5.4.2 Thermal Expansion

To achieve an operational SIM, as described previously, a gap must be maintained at micron levels. Although the SIM is an inherently low current machine and will thus have negligible I^2R losses, the losses will not be zero. Charge on the conduction plates, swapping from face-to-face as the rotor traverses a full rotation, will cause heating. This heating of the metal plate, an energy loss, will cause it to expand into the air gap. Equation (81) describes this linear thermal expansion. In Equation (81), ΔL is the change in length, α is the coefficient of expansion for the material, L_0 is the original length of the material and ΔT is the change in temperature. Common AISI 304 stainless steel has a manufacturer's α value of $16.9\frac{\mu m}{mK}$. Stainless steel plates have again been specified to insure corrosion, oxidation or other causes of deterioration do not dimensionally alter the parts with time. An initial rotor plate thickness of 1cm has been chosen as a conservative conduction plate thickness value. The ΔT change is a result of the heating loss due to the internal currents. Assuming the I^2R losses are embodied solely as thermal energy and can be expressed as a thermal conduction loss, then an approximation for the temperature change from the rotor plate to the surrounding ambient environment can be found. These approximations are shown in Equations (82) and (83).

$$\Delta L = \alpha L_0 \Delta T \quad \textbf{(81)}$$

$$P_{loss\_cond} = P_{loss\_I^2R} \quad \textbf{(82)}$$

$$P_{loss\_cond} = \frac{\lambda A \Delta T}{L_0} \quad \textbf{(83)}$$

In (83) λ is the thermal conductivity and *A* is the surface area for conduction dissipation. Solving Equation (81) by rearranging (83) for a 1HP motor with 1kV source, results in a current of 0.746A and a calculated linear expansion via conduction heating of about 1picometer with a thermal conductivity of $16.3\frac{W}{mK}$ and an area of $2.5cm^2$, parameters to match the SIM model. This small value is due to the low current inherent on SIMs, large surface areas and relatively thin conduction plates. This shows that expansion due to internal heating is negligible.

However, if the ambient temperature of the SIM were to increase by 20˚C, then via Equation (81), each conduction plate will expand by about 4.6μm, which is a compound effect and could effectively destroy the air gap. For this reason, SIMs may have difficulty operating in an outdoor environment without some means of active gap control either through appropriate cooling and/or by actively controlling the gap with feedback.

5.5 Mechanical Layout

Based upon the developed models, an S18/R12 SIM has been designed and analyzed. The conceptual design presented has been developed with emphasis for simplicity on fabrication, construction and operation and is shown in Figure 85 and Figure 86. The design is not intended to be ready for fabrication as there are many mechanical details yet to be developed. However, the design builds upon earlier models. It assumes that bearings or other techniques are sufficient to mitigate vibration issues as discussed earlier. Utilizing aerospace bearings, such as ABEC 7 or 9 bearings, potentially with active gap control in conjunction with precision ground shafts supports this assumption. It is also assumed that a housing structure allowing a fluid or gas dielectric could be fabricated and maintained. Figure 85 shows the assembled SIM model and is intended to provide illustration for one possible embodiment of the motor.

The design incorporates a housing that is 160mm tall, 85mm deep and 150mm wide with a shaft diameter of 10mm. The housing is intended to support the rotor on bearings and to purposefully locate stator plates in such a manner that a gap of 25µm (1mil) is maintained. Figure 86 shows an exploded view of the conceptual SIM.

Figure 87 shows a profile view of the shaft with rotor and stator plates stacked with gap spacing of 25µm (1mil). The rotor and stator substrate plates are constructed of a premium glass which is electrically insulative. The conductive surface coating is applied to this glass substrate. As embodied, the glass plates would be fabricated from 'Crysterna' IG335 fabricated by Ishizuka Glass Co. The substrate is 3.5mm thick and has undergone a chemical surface tempering process to significantly improve is strength and minimize scratching. Because it is a glass, the surface can be polished to insure flatness and parallelness between opposite faces and has a low thermal expansion coefficient. Figure 88 shows the published properties of 'Crysterna' glass.[19]

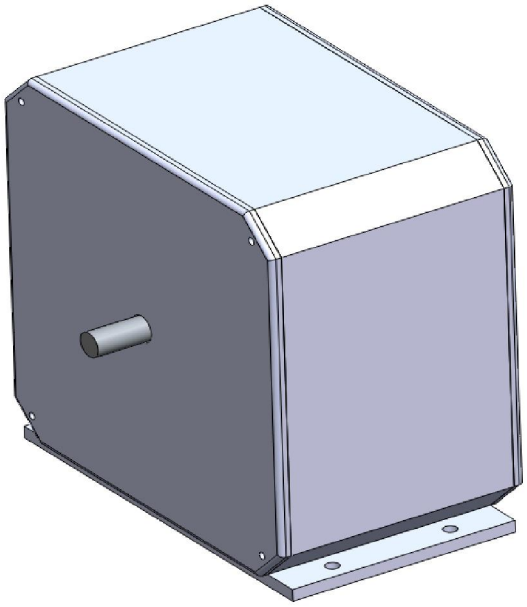

Figure 85 Assembled S18/R12 SIM

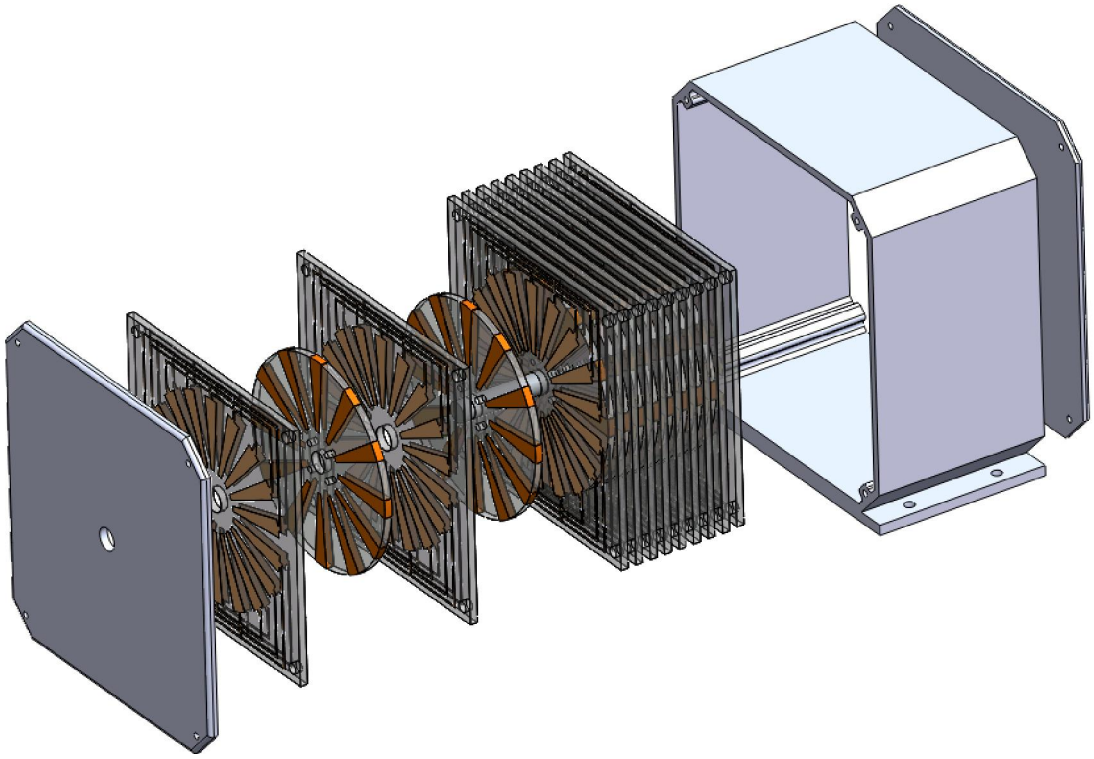

Figure 86 Exploded View of S18/R12 SIM

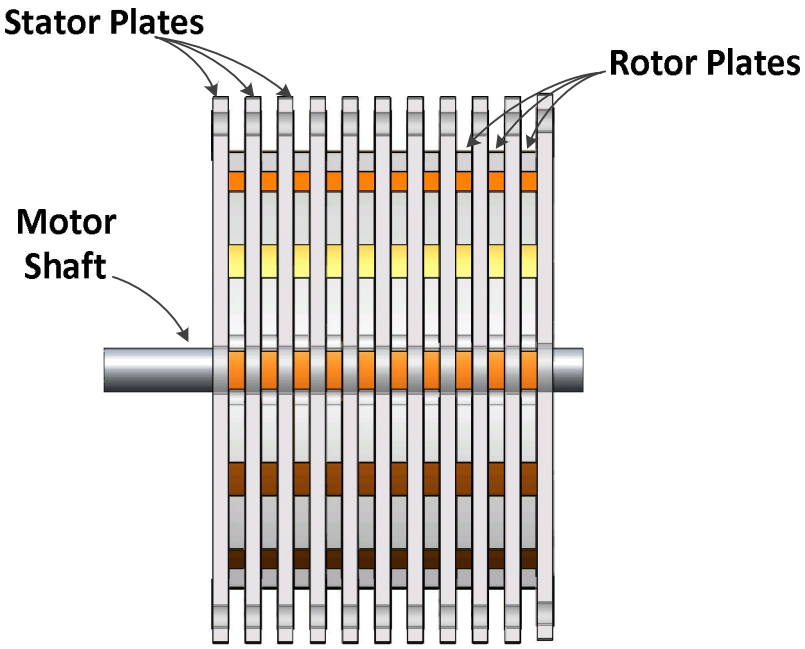

Figure 87 Profile View of Shaft with Rotor and Stator Plates

Characteristics of "CRYSTERNA"

Specific gravity		2.51	g/cm^3	JIS C 2141
Chemical durability		0.28	Na_2Omg	ASTM C 225
Refractive index		1.52	nD	JIS K 7105
Thermal properties	Strain point	511	°C.	JIS R 3103
	Softening point	708	°C.	JIS R 3103
	Expansion (a)	8.7	×10-6/C	JIS C 2141
Mechanical properties	Bending strength	863	MPa	JIS C 2141
	Vickers hardness (Hv)	640	300g,15sec	JIS C 2141
	Young's modulus	7 × 104	MPa	JIS R 3103
	Surface compression	588 to 980	MPa	Measured by"FSM-60" (TOSHIBA CORPORATION)
	Surface compression layer	20	μm	

Figure 88 Crysterna Glass Properties

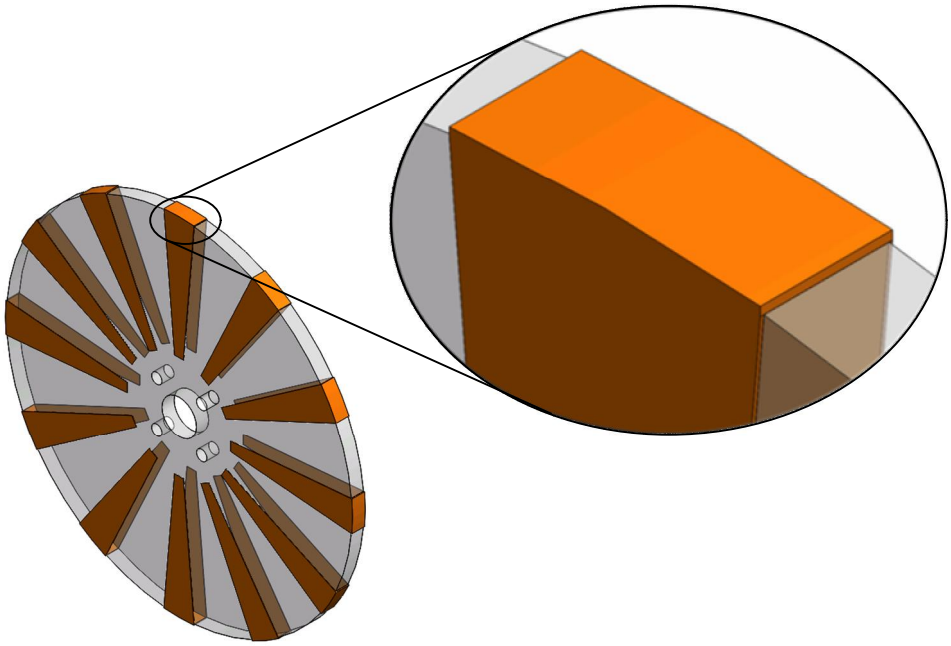

Figure 89 Rotor Plate with Conductive Coating View

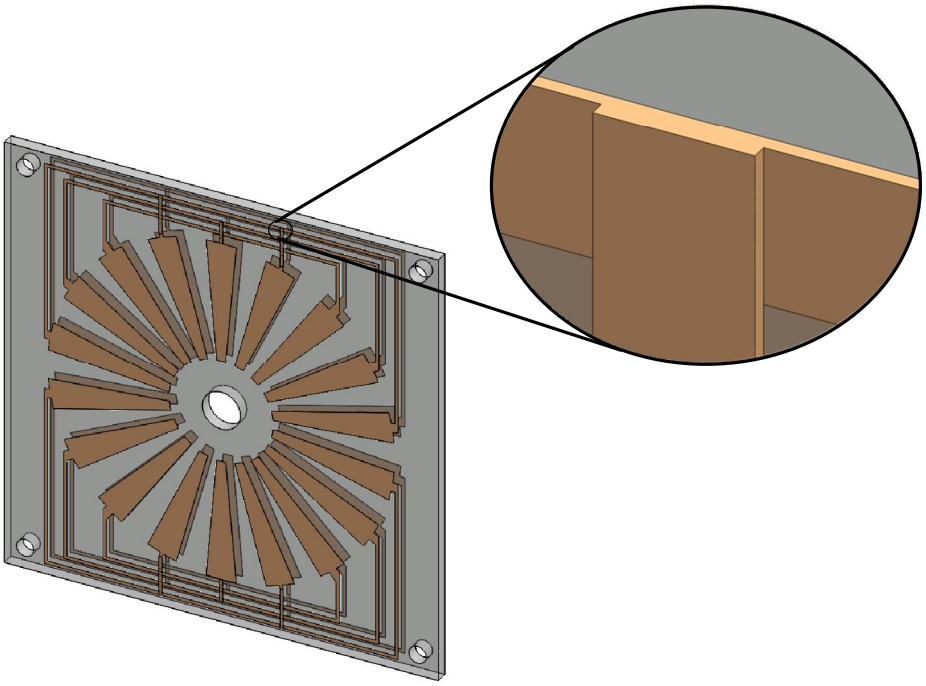

Figure 90 Stator Plate with Phase Connection View

Figure 89 shows the rotor plate. It has an outer diameter of 100mm with 12 conductive segments spaced across its two faces. For this prototype design the segments are embodied as a conductive coating 100µm thick, each with an effective area of 200mm^2. Segments on opposite faces are connected through a conductive band that straddles the two faces.

Figure 90 shows a stator plate with 18 segments. The respective phases are interconnected via a bus system located at the top and bottom of the plate. Similar to printed circuit board techniques, the phases are able to straddle across the bus to make the necessary electrical connections.

The present design employs 10 rotor plates and 11 stator plates to generate the needed torque. This rotating assembly has a computed mass of 612 grams with a mass moment of inertia of 780kg*mm^2. The design also assumes that a conformal coating of Kapton® HN25 can be applied uniformly to the stator parts .

5.6 Design of a 1HP SIM

With an understanding of rotational forces and how they are developed within a SIM, a 3ϕ, 1kV SIM with six parallel poles (repeated poles) design is presented. As will be shown later, utilizing six parallel poles will limit the motor speed, but this will keep F_{gap} to a manageable level. To limit the effects of vibration, a small motor is preferred as any minor vibration, accentuated by a large radius, has the potential to damage the motor. For this reason, the outside radius (r_{out}) was set at 100mm while the inside radius (r_{in}) was set at 32mm.

$$Ph = 3 \quad \textbf{(84)}$$

$$Repeats = 6 \quad \textbf{(85)}$$

$$S_{num} = Ph * Repeats = 18 \quad \textbf{(86)}$$

$$R_{num} = 2\frac{S_{num}}{Ph} = 12 \quad \textbf{(87)}$$

Based upon these general design values, it is now possible to compute some geometric data, such as the rotor and stator pole angles.

$$\alpha_{Stator\ Pole} = \frac{180^\circ}{Ph * Repeats} = 10^\circ \quad \textbf{(88)}$$

$$\alpha_{Rotor\ Pole} = \frac{360^\circ - R_{num}\alpha_{Stator\ Pole}}{R_{num}} = 20^\circ \quad \textbf{(89)}$$

This results in a stator with 18poles and a rotor with 12poles, an S18/R12 motor, with 10˚ and 20˚ per stator and rotor pole respectively.

Now, based upon the rotor and stator pole angles, the total angle for a complete electrical rotation may be computed and a phase engagement pattern is shown in Figure 91.

$$\alpha_{Elec\ Rotation} = \alpha_{Stator\ Pole} + \alpha_{Rotor\ Pole} = 30^{\circ} \quad \textbf{(90)}$$

As described previously, capacitance will be in direct proportion to the area overlapped between the rotor and stator and can be measured as the rotor rotates. The equivalent circuit model for computing this capacitance is shown in Figure 92. From this model a plot showing capacitance versus mechanical position (degrees) can now be generated based upon physical and geometric constrains as shown in Figure 93. Knowing how capacitance varies with position makes it possible to compute the resulting charge (Q) buildup that develops the desired force for a given voltage and position. Figure 94 shows this relation for three voltages, 0.1kV, 0.4k and 1kV.

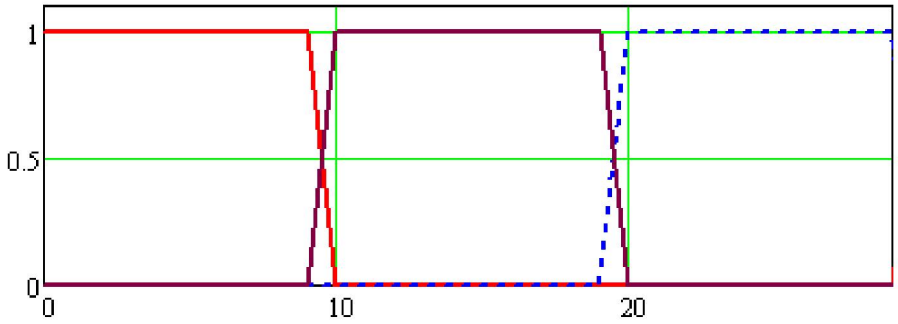

Figure 91 2D Electrical Rotation Diagram

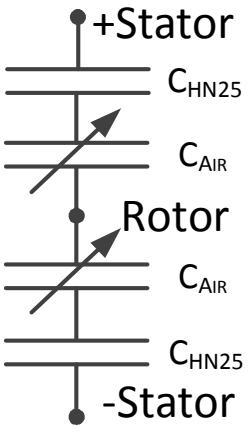

Figure 92 Rotational SIM Capacitance Model

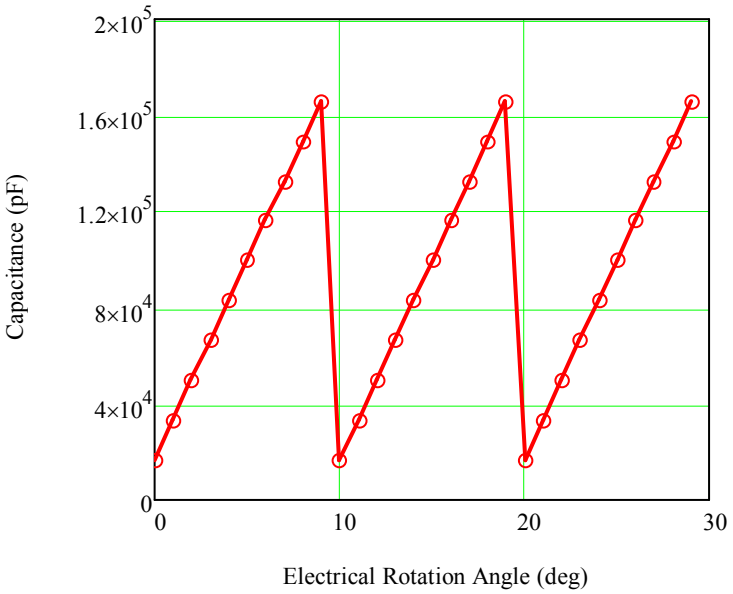

Figure 93 Rotational SIM Capacitance vs Position

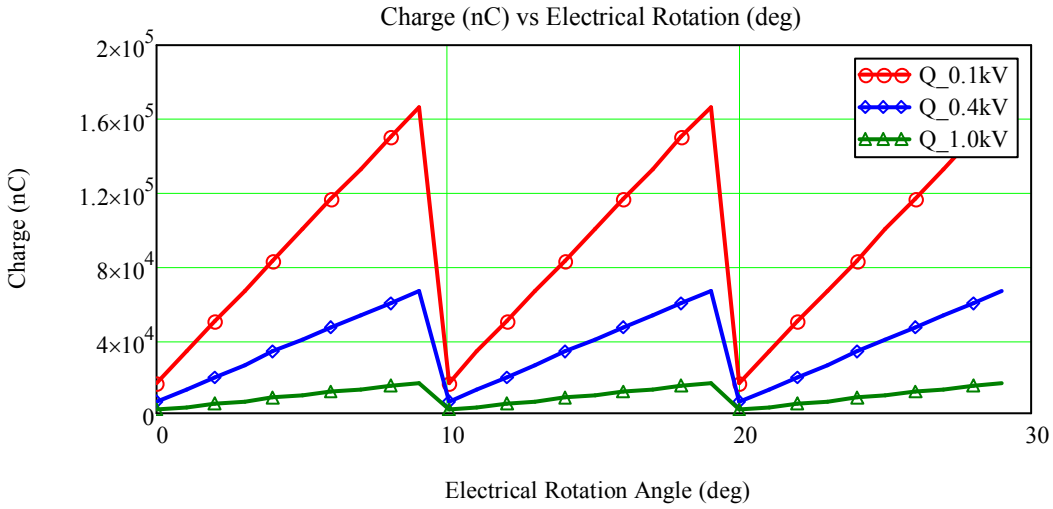

Figure 94 Charge vs Position for 0.1kV, 0.4kV and 1.0kV

The computed charge will give rise to fields and forces between the rotor and stator. These forces can now be computed based upon Equations (79) and (80) showing the rotational theta force (tangential) and the gap (normal) forces respectively. Figure 95 shows the tangential force relation if the voltage is held fixed at 0.1kV, 0.4kV and 1kV while the rotor position varies. Similarly, if the rotor is positioned at 1˚, 5˚ and 10˚ while the voltage is varied through its full range while force is measured then a family of identical curves result, as plotted in Figure 96. Figure 97 displays a 3D perspective of the tangential force.

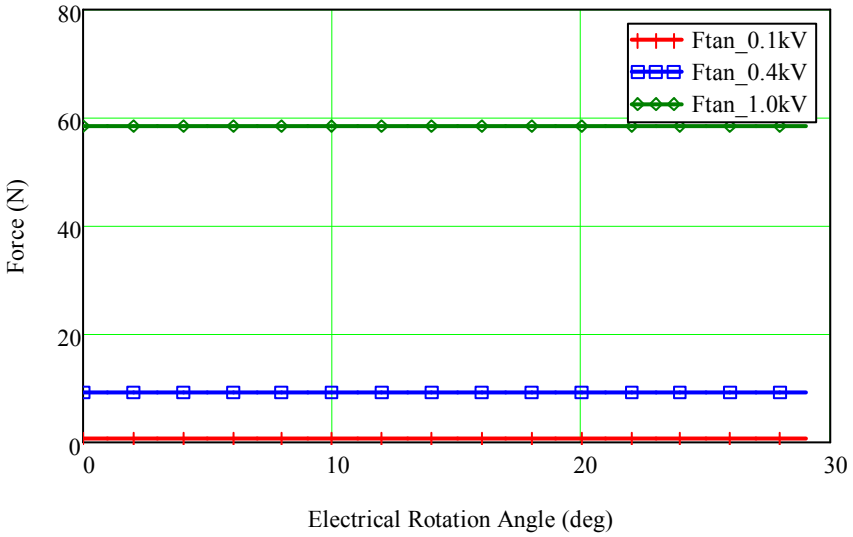

Figure 95 Tangential Force (N) vs Position (deg) for 0.1kV, 0.4kV and 1.0kV

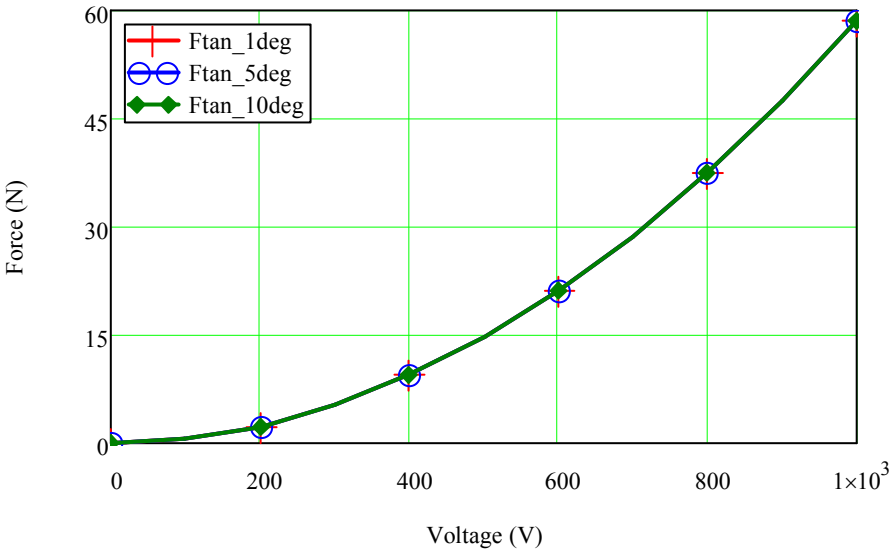

Figure 96 Tangential Force (N) vs Voltage (kV) for 1˚, 5˚ and 10˚ of Overlap

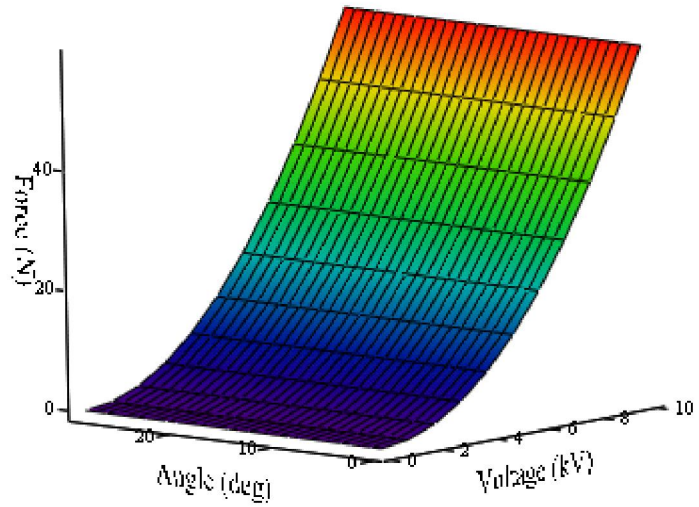

Figure 97 Tangential Force 3D

These figures show that tangential force is dependent solely upon voltage and has no relation to position once engaged. This is because tangential force is only developed by fringing flux that is on the leading edge of a plate. For flux that is not on the leading edge there is no tangential component which tends to be laminar as this is the minimum energy state. These conditions are shown in Figure 98 and Figure 99 and help illustrate why additional overlap can only increase normal force.

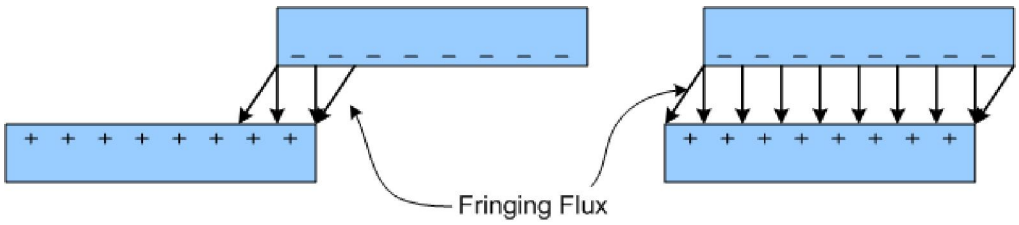

Figure 98 Leading Edge Flux

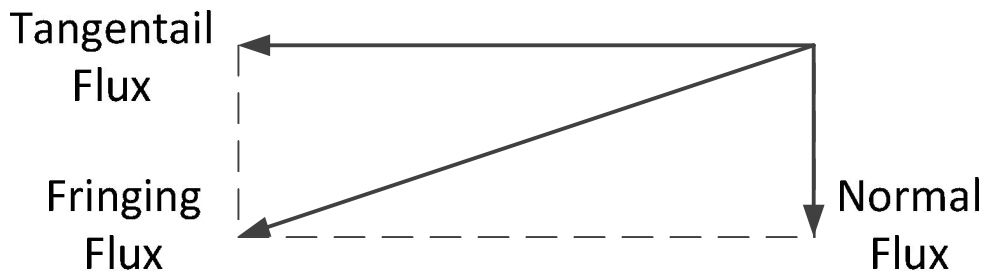

Figure 99 Flux Vectors

Utilizing Equation (80), Figure 100 - Figure 102 have been generated to show the linear relation between the normal force and position (overlap) for a given voltage. A large ratio between the two forces means that a disproportionate amount of energy is being utilized to generate normal force rather than a useful torque generating tangential force. Thus, this normal force is wasted energy and adds a design burden on the mechanical SIM designer as the motor must withstand the forces to maintain the gap for continuous operation.

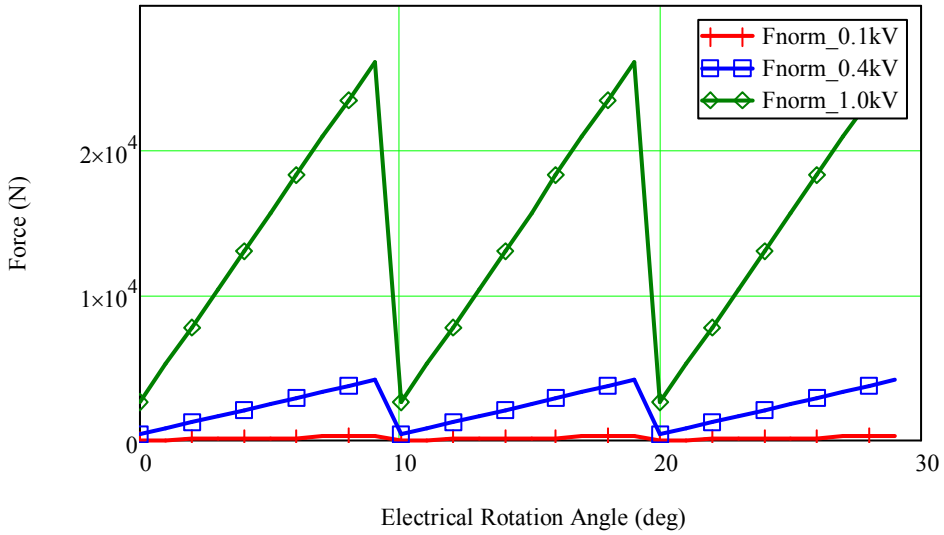

Figure 100 Normal Force (N) vs Position (deg) for 0.1kV, 0.4kV and 1.0kV

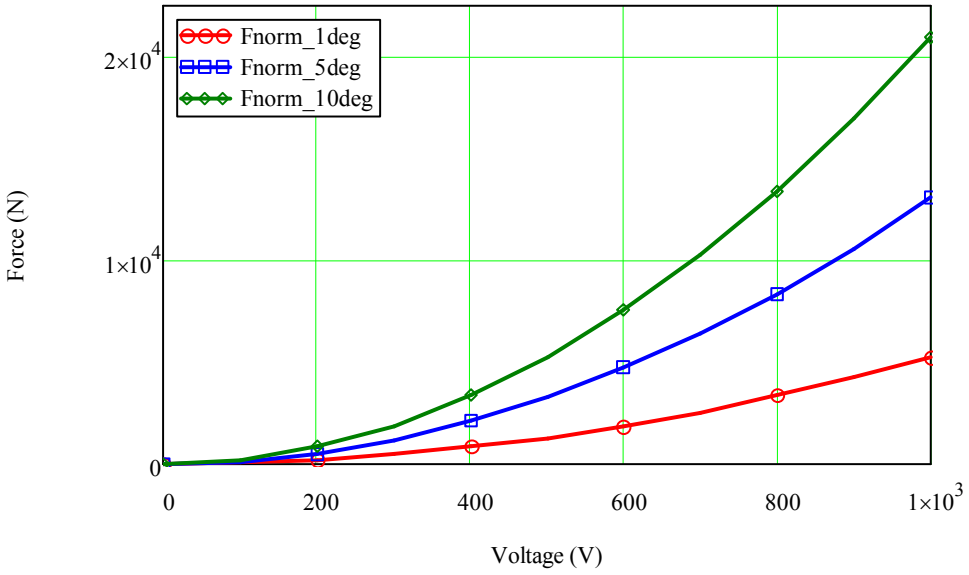

Figure 101 Normal Force (N) vs Voltage (kV) for 1˚, 5˚ and 10˚

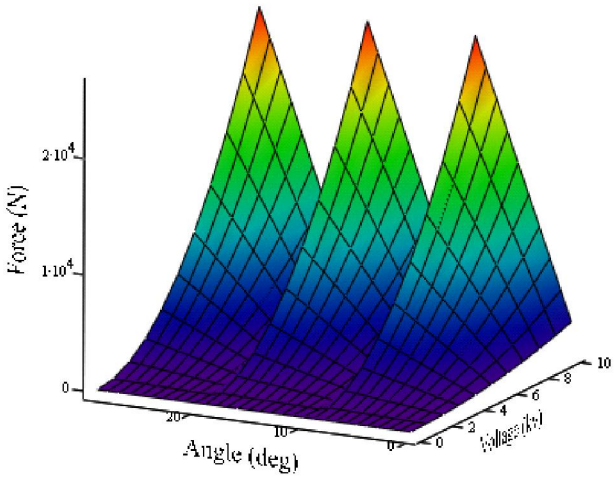

Figure 102 Normal Force (N) 3D

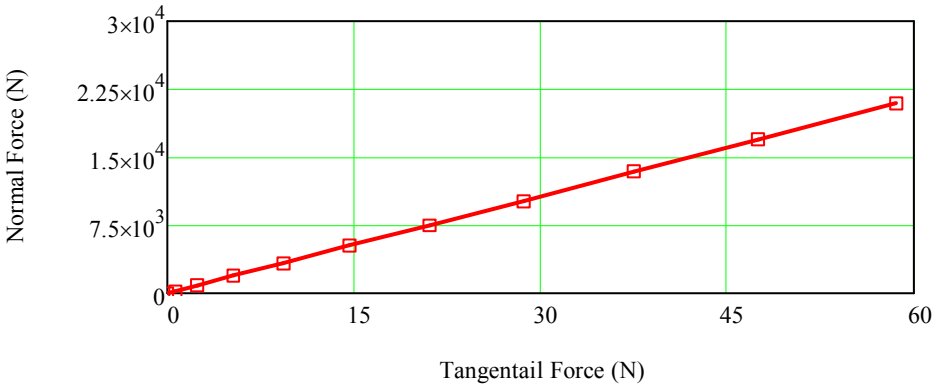

Figure 103 Force Ratio at 10deg for Varied Voltage

5.6.1 Minimizing Normal Force

One technique to keep the normal forces at manageable levels easing the design burden of the mechanical engineer is to increase the number of poles per phase. By increasing the poles, it is possible to maintain high total capacitance of a phase, but to achieve it through a small phase angle. Effectively, this is adding edges by which useful tangential force can be created, and operating in a region before normal forces become excessive and hinder the mechanical design. This technique, however, comes with increased complexity in total SIM parts count and required higher switching speeds.

With the present design, the ratio between normal and tangential forces may be computed and is shown in Equation (91) and Figure 103.

$$Force\ Ratio = \left.\frac{F_{Normal}}{F_{tangential}}\right|_{Max} \approx 447 \tag{91}$$

Having a large force ratio means that a majority of the developed force will be normal force rather than useful tangential force. Large force ratios imply that the stator and rotor must be able to withstand these forces without deflection, which is a serious concern when air gaps are measured in microns. One method to insure the resulting forces are manageable is to seek *mutual force cancellation*. In this design style, charges and thus forces are balanced on each side of a rotor and stator plate. To accomplish this, the SIM may be designed with either a floating or grounded rotor, as shown in Figure 104 and Figure 105. The difference between these two designs will be the total developed capacitance.

The floating rotor topology is effectively two variable capacitors that are in series, while the grounded rotor design effectively creates two variable capacitors in parallel. In operation, the floating rotor design will inherently maintain a neutral net charge as it is isolated, while the rotor charge with a grounded rotor design can vary due to the field intensity which is dependent upon the gap size.

Ultimately, maximum charge density is desired and a grounded rotor would be preferred as its capacitance is larger, as shown in Equations (92) and (93). However, if the rotor of the grounded rotor topology is not perfectly centered throughout its rotation, meaning the gaps on either side of the rotor are unequal, then a charge and force imbalance will occur that will tend to exacerbate non-symmetric loading, as illustrated in Figure 106.

$$\frac{1}{C_{Tot}} = \frac{1}{C_1} + \frac{1}{C_2} \rightarrow C_{Tot} = \frac{1}{2}C \tag{92}$$

$$C_{Tot} = C_1 + C_2 \geq C \tag{93}$$

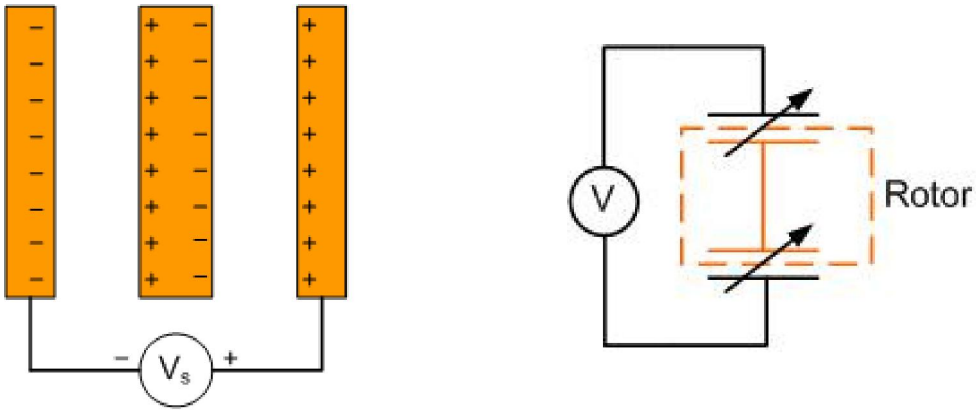

Figure 104 Floating Rotor SIM

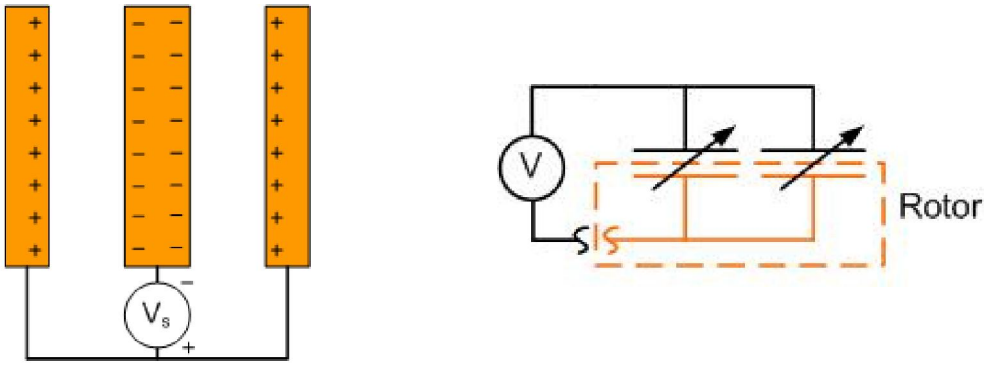

Figure 105 Grounded Rotor SIM

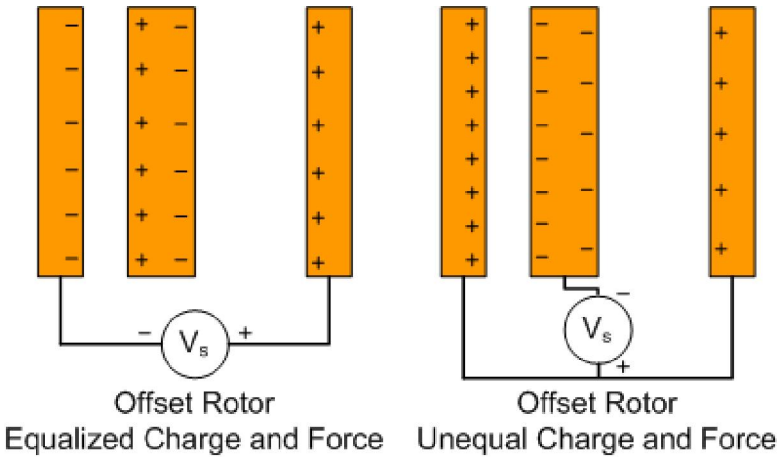

Figure 106 Mutual Force Balancing

5.7 Conclusion

This chapter has discussed the design and constraints of a dynamic SIM. It provided the dynamic force equation for a rotational system, which led into capacitance and electro-mechanical energy relations. These relations were used to compute the force relations for an operational SIM, the physical embodiment of which was previously described.

While force relations have been developed, this chapter discussed some of the unique problems still to be worked out for successful operation of a SIM. The assembly of an operational SIM will require attention to detail and may require more stringently controlled gap tolerances than traditional motors. However, no requirement is beyond present manufacturing techniques, which makes an operational SIM similar to that which has been described herein feasible.

The previous chapter described an embodiment of a mechanical SIM. Based upon that design, this chapter describes a dynamic simulation of that system.

6.1 Charge Dissipation

Unlike an induction machine, breaking the connection between the voltage source and load on an ESM does not remove the source of the motor's force. This is because the charge is static, purposefully isolated to prevent dissipation, and will remain in place until the charge is given a path to dissipate. This is a unique problem of ESMs.

Modern induction motor controls utilize a DC source (a.k.a. DC link between AC source and motor terminals) to generate the desired switching scheme necessary to control the currents and/or voltages that create the specific speeds , torques and motion profiles of the induction machine. A similar scheme is necessary for ESMs, however, the SIM with a linear capacitance variation requires a stepping scheme from one phase to the next to advance its position. Once the rotor has moved to the desired position, the charge that generated the force to initiate the move must be purposefully removed to eliminate that force. If the charge is not removed, its static force will inhibit further rotor motion. This is an ideal situation for a locked rotor scenario, as no additional energy needs to be applied to hold the rotor fixed. However, continuous rotation will be inhibited unless the charge is removed once the rotor is in a desired position.

The quickest solution to remove the charge is to short the terminals. However, in doing so the charge is lost as heat, an inefficient process. Another solution is to connect the terminals to a lower voltage bus, thus removing the charge while permitting it to be collected and reused rather than destroyed. This solution, however, requires multiple buses and added complexity. A simpler solution is to utilize a high voltage high frequency (HVHF) pulsing scheme. Using an alternating current (AC) source allows charge to pass through zero twice per period and is thus a natural point in time to switch between phases, as charge will be zero at this point. Figure 107 illustrates this pulsing scheme. (Although switching at a zero crossing is the ideal, a resistor is utilized to eliminate any residual charge once a phase is opened, as switching at a perfect 0V is challenging to achieve in a practical sense.)

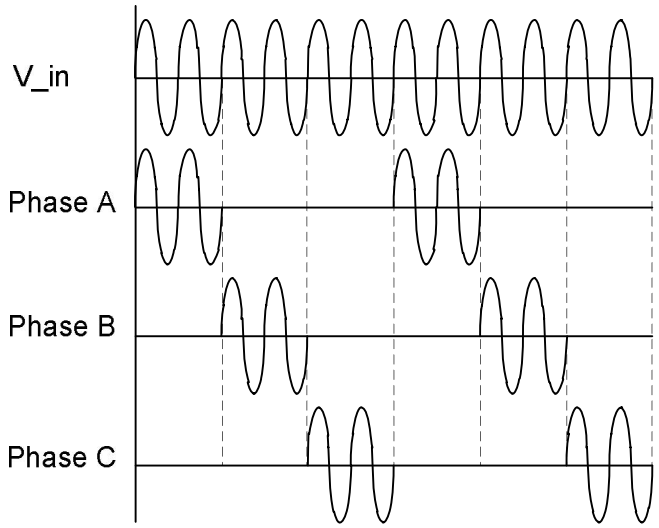

Figure 107 AC Switching Scheme

Because a HF source is utilized, the computed force is now a function of the RMS voltage. As polarity of the charge does not affect force direction, an AC source offers reduced complexity over more traditional induction motor drive topologies while still producing useful force.

6.2 HFHV Switching Schemes

The HF switching scheme allows for high voltages to be created using numerous drive topologies, two of which are shown in Figure 108 and Figure 109. In both topologies, a HF source is generated at low voltage (LV) which is stepped to a high voltage via a transformer. In doing so, desirable isolation between the source and motor is created. Figure 108 shows a HFHV system where a single transformer is used and each phase is switched at high voltage (HV). For very large voltages, this could be problematic as isolating the HV switch and its control can be difficult with existing off-the-shelf switches. An alternative design that does not have this issue is shown in Figure 109. In this design, switching occurs at LV which is then stepped-up via transformer action for each phase. While switch isolation issues are eliminated, this design has increased weight due to the transformer.

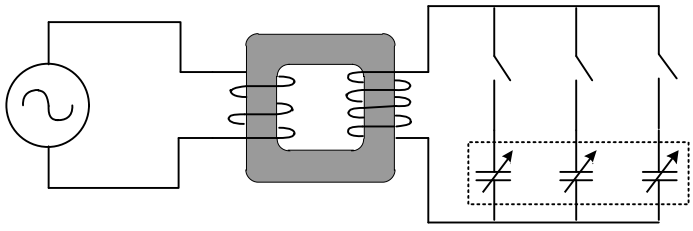

Figure 108 HVHF Drive Topology - HV Switching

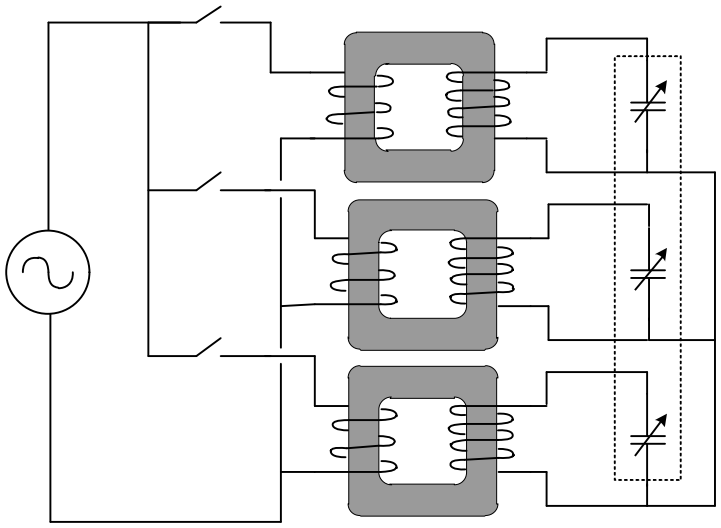

Figure 109 HVHF Drive Topology - LV Switching

Based upon the measured Paschen curves and material options previously described, the HV switching scheme is appropriate for dynamic modeling as existing off-the-shelf switches can be utilized for voltages through about 1.6kV without a significant price increase. (Assuming higher voltages are desired and an unlimited budget is available, there are HV IGBTs that can reach 6.5kV (at a cost of about $6k) and a DARPA program to develop a 13kV IGBT is underway, yet, its benefits are years from reaching the public sector.)

Although it is beyond the scope of this project, magnetic switches based upon magnetic amplifier technologies may be an alternative means to switch HVHF sources without suffering from isolation or polarity issues. Additionally, there is significant literature on multilayer DC systems using solid state switches as a means to generate HVs. This may be promising for future ESM drive research.

6.3 Control Algorithm

Equations (70),(71) and (74) are presented again for development of a control algorithm for a rotary SIM.

Current is the time rate of change of charge as shown in Equation (94) below.

$$i = \frac{dq}{dt} \tag{94}$$

Expanding the charge, q, to show that it is the product of capacitance (C) and voltage (V), allows Equation (94) to be expanded and is shown in Equation (95).

$$i = \frac{d(CV)}{dt} = C\frac{dV}{dt} + V\frac{dC}{dt} \quad \textbf{(95)}$$

Because capacitance is dependent upon angular position, Equation (95) can be rewritten to incorporate rotation which allows for a phase current to be described as shown in Equation (96).

$$i_{Ph} = C\frac{dV_C}{dt} + V_C\frac{dC}{dt} = C(\theta)\frac{dV_C}{dt} + \omega V_C\frac{dC(\theta)}{d\theta} \quad \textbf{(96)}$$

(Note that in Equation (96), the differential of capacitance has been rewritten to remove *dt* and replace it with the equivalent dt=ω/dθ.)

$$i_{Ph} = C(\theta)\frac{dV_C}{dt} + \omega V_C\frac{dC(\theta)}{d\theta} \quad \textbf{(97)}$$

Equation (97) shows the equivalent electrical model of a single phase ESM. The capacitor voltage V_C is that voltage which is applied to the stator plates.

Capacitance can be written as a function of geometry as shown in Equation (98). This Equation also shows that capacitance is solely dependent upon rotor angle θ_{Rtr}.

$$C_{Ph} = \varepsilon\theta_{Rtr}\frac{\left(r_{out}^2 - r_{in}^2\right)}{2gap}repeats = K_1\theta_{Rtr} \quad \textbf{(98)}$$

Substituting this into Equation (97) results in a final Equation describing the motor and is shown in Equation (99).

$$i_{Ph} = C(\theta)\frac{dV_C}{dt} + \omega V_C K_1 = i_C + i_\omega \quad \textbf{(99)}$$

This result is similar to induction motors in that it has two components, a capacitor current i_C and a "speed" current i_ω. The speed current is shown to be independent of angular change resulting in a simple constant.

Equation (99), in conjunction with a mechanical free-body diagram (FBD) of the motor, allows a complete single phase representation of the system to be developed and is shown below in Figure 110.

In Figure 110, $V_{Ph}$is the source phase voltage, Sw is a control switch, R_{ESR} is the equivalent series resistance of any control line, t_{Mtr} is the developed motor torque, B_{Rtr}, assumed to be negligible in this model, is friction due to rotor bearings, windage etc., t_{Load} is the counter torque of the load and J_{Load} is the inertia of the mechanical system inclusive of the load.

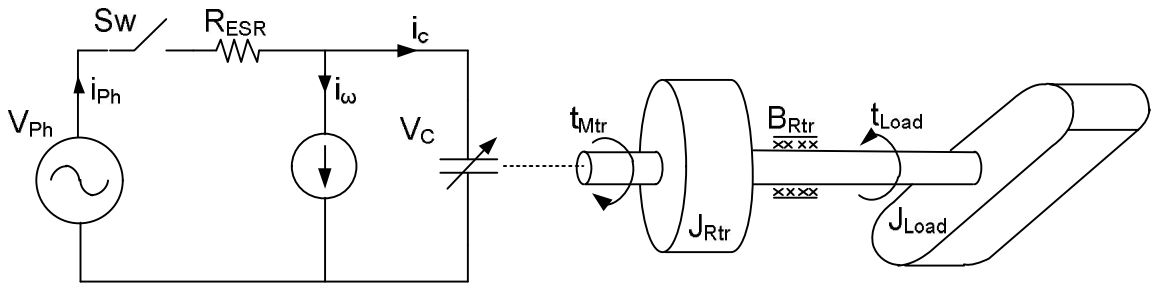

Figure 110 Single Phase Free Body Diagram of SIM

Using the single phase FBD of Figure 110, a control algorithm can now be created. Writing an equation for the mechanical system, the motor torque minus the load torque is equal to the product of inertia and acceleration plus the product of friction and speed. This is shown below in Equation (100).

$$\tau_{Mtr} - \tau_{Load} = (J_{Rtr} + J_{Load})\frac{d\omega_{rtr}}{dt} + f\omega_{rtr} \quad \textbf{(100)}$$

Transforming Equation (100) to the s-domain allows for rotor angle θ to be found and is shown in Equation (101). (Note that the inertia sources have been combined in to a single term.)

$$\theta_{Rtr} = \frac{1}{s}\left(\frac{\tau_{Mtr} - \tau_{Load}}{Js + f}\right) \quad \textbf{(101)}$$

A complete control scheme can now be created. A *bang-off-bang* control topology, one in which the system response is assumed to be fully ON or OFF, has been implemented to compliment the HVHF source topology and zero crossing switching scheme. The control diagram in Figure 111 shows the flow of control parameters with Figure 112 detailing the switching between phases.

The control algorithm works to control voltages such that a predefined speed profile is followed by the motor. Based upon the difference between the desired speed and the simulated value, an error signal is generated. Combining this error signal with a clock pulse that matches the zero crossing of the applied voltage with a tolerance of +/-50V allows for the individual phase switches to be controlled.

The switching detail of Figure 112 shows that if an error (*e*) between the desired and simulated value occurs, then the sign of the error and angular shaft position of the motor determine the appropriate switches to open or close.

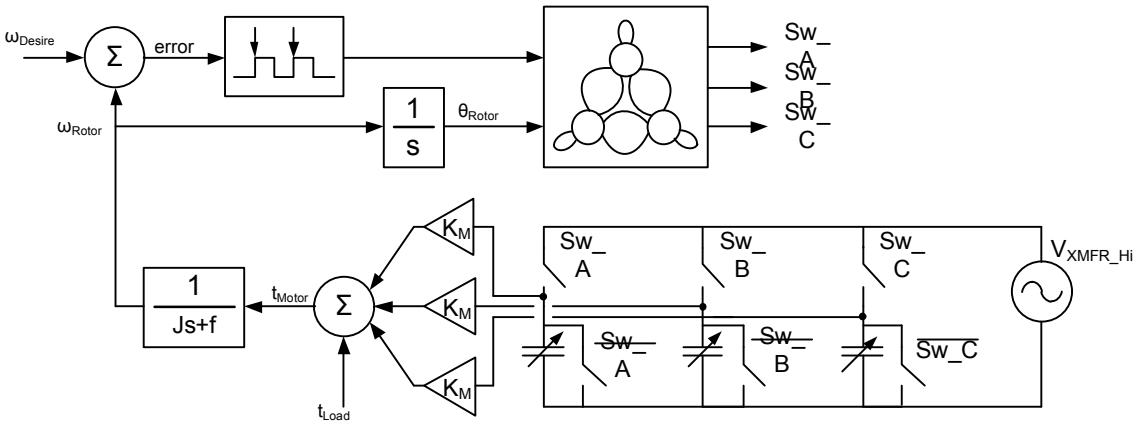

Figure 111 Control Diagram

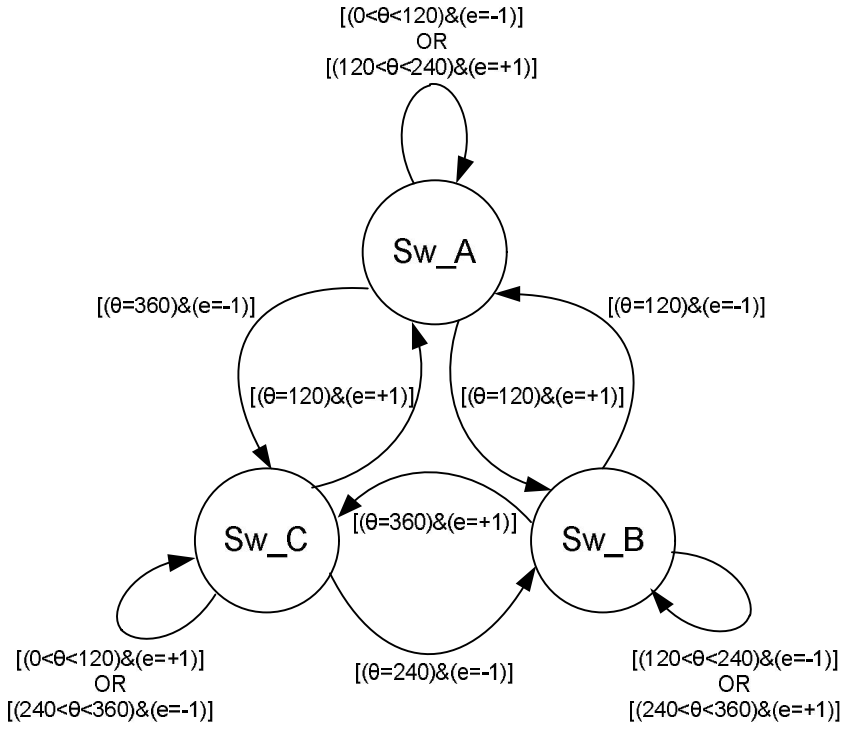

Figure 112 Switching Diagram Detail

6.4 Dynamic Spice Model

Figure 111 and Figure 112 show the governing control model graphically. To implement this control model with motor parameters, a dynamic model to embody the parameters of Equation (99) and the overall mechanical design was created using the software B2-Spice® v5.

6.4.1 Phase Capacitor Circuit Element

A custom circuit to model the capacitance of a phase was created. The custom circuit is represented by the custom circuit element symbol shown in Figure 113 and whose underlying circuit is shown in Figure 114. The phase capacitor symbol has four terminals, two that provide the capacitance value necessary for computing the speed current and two others that compute the voltage over the capacitor terminals, C_val_pos-to-C_val_gnd and C_pos-to-C_neg respectively.

In Figure 114 the voltage over the terminals C_pos-to-C_neg is measured by Vm1 shown in Figure 114. This voltage is multiplied by the capacitance value, brought into the model through the terminals C_val_pos-to-C_val_gnd, which is then differentiated via the function block A1, and represents the capacitor current as shown in Equation (102). This function block outputs a voltage C_ref, which is the governing parameter for the B3 dependent current source needed to determine the current of the capacitor.

$$i_{C\_ref} = C\frac{dV}{dt} \tag{102}$$

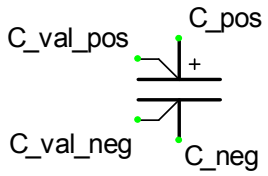

Figure 113 Custom ESM Phase Capacitor Symbol

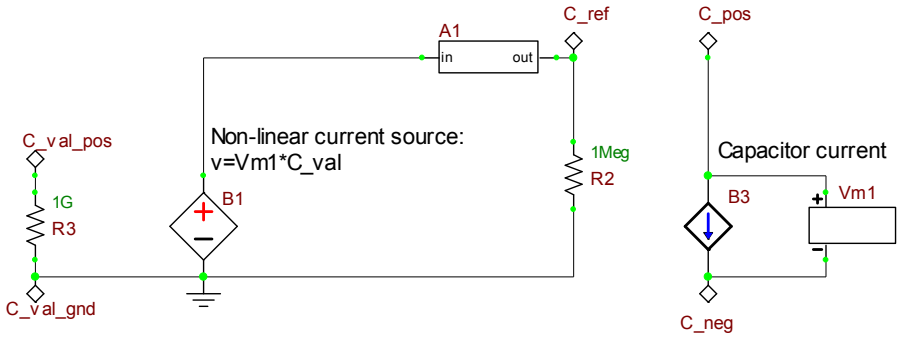

Figure 114 Phase Capacitor Circuit Detail

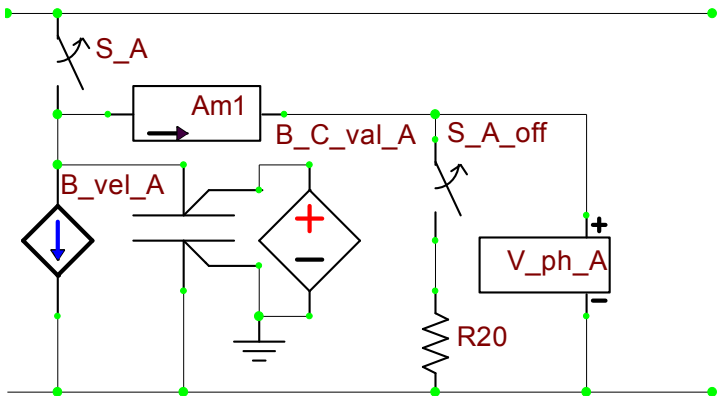

Figure 115 ESM Phase Model

6.4.2 Single Phase Model

Figure 115 shows a complete model of a single phase of SIM. The series switch S_A connects the HVHF signal to phase capacitor previously described, the modeled motor phase, when the terminal A_sw is positive. This occurs according to the switching diagram detail shown in Figure 112. If the A_sw terminal is negative the S_A switch opens and parallel switch S_A_Off closes to eliminate any remaining charge via resistor R20.

6.4.3 Torque, Speed and Position

Torque is computed by summing together the respective forces of each phase. Passing this torque parameter through the transfer function, A1_J_F, representing the inertia and friction of the ESM, as shown in Figure 116, results in a rotor velocity. The velocity is then passed to the custom Speed-to-Position block, shown in Figure 117 and detailed in Figure 118. The velocity value is integrated in order to recover position in radians, which is then converted to electrical and mechanical reference frames.

The capacitance of each phase is incorporated into the system through a piecewise linear (PWL) control block as shown in Figure 119. This block, via a simple look-up table, computes capacitance based on position, Shft_Real, the computed mechanical position of the shaft. The position-to-phase circuit for all three phases is shown in Figure 120.

The complete Spice circuit that models the dynamic characteristics of the ESM is shown in Figure 121. Because it does not directly relate to the ESM, the model assumes that a LVHF source is driving the voltage of the system and that an appropriate HF transformer is available to step-up the voltage to the desired value.

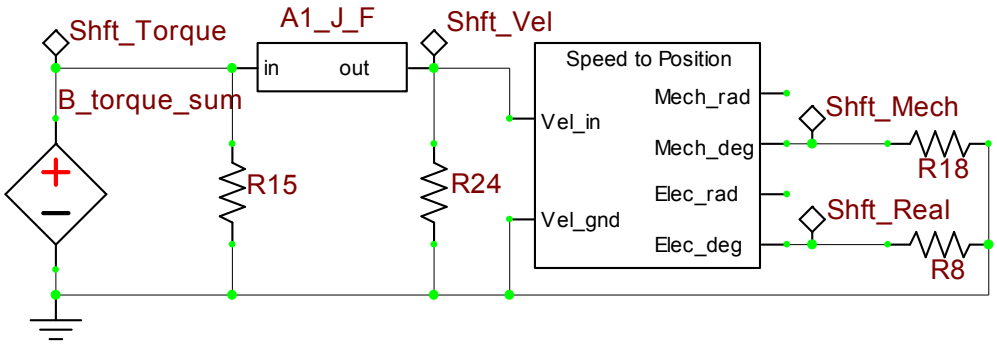

Figure 116 Torque to Speed and Position

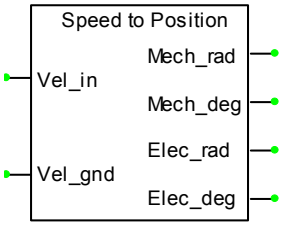

Figure 117 Speed-to-Position Block

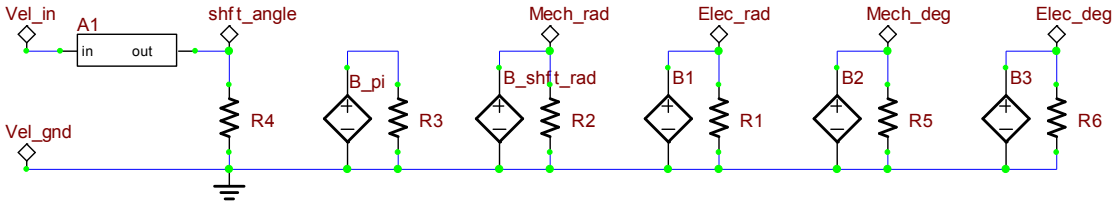

Figure 118 Speed to Position Circuit Detail

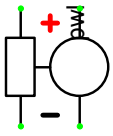

Figure 119 Piecewise Linear Controlled Source

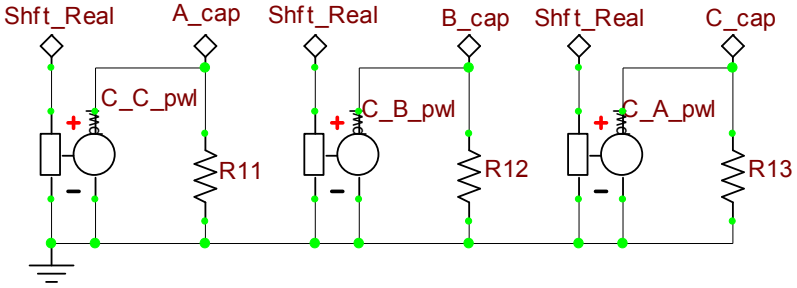

Figure 120 Position to Phase Capacitance Circuit

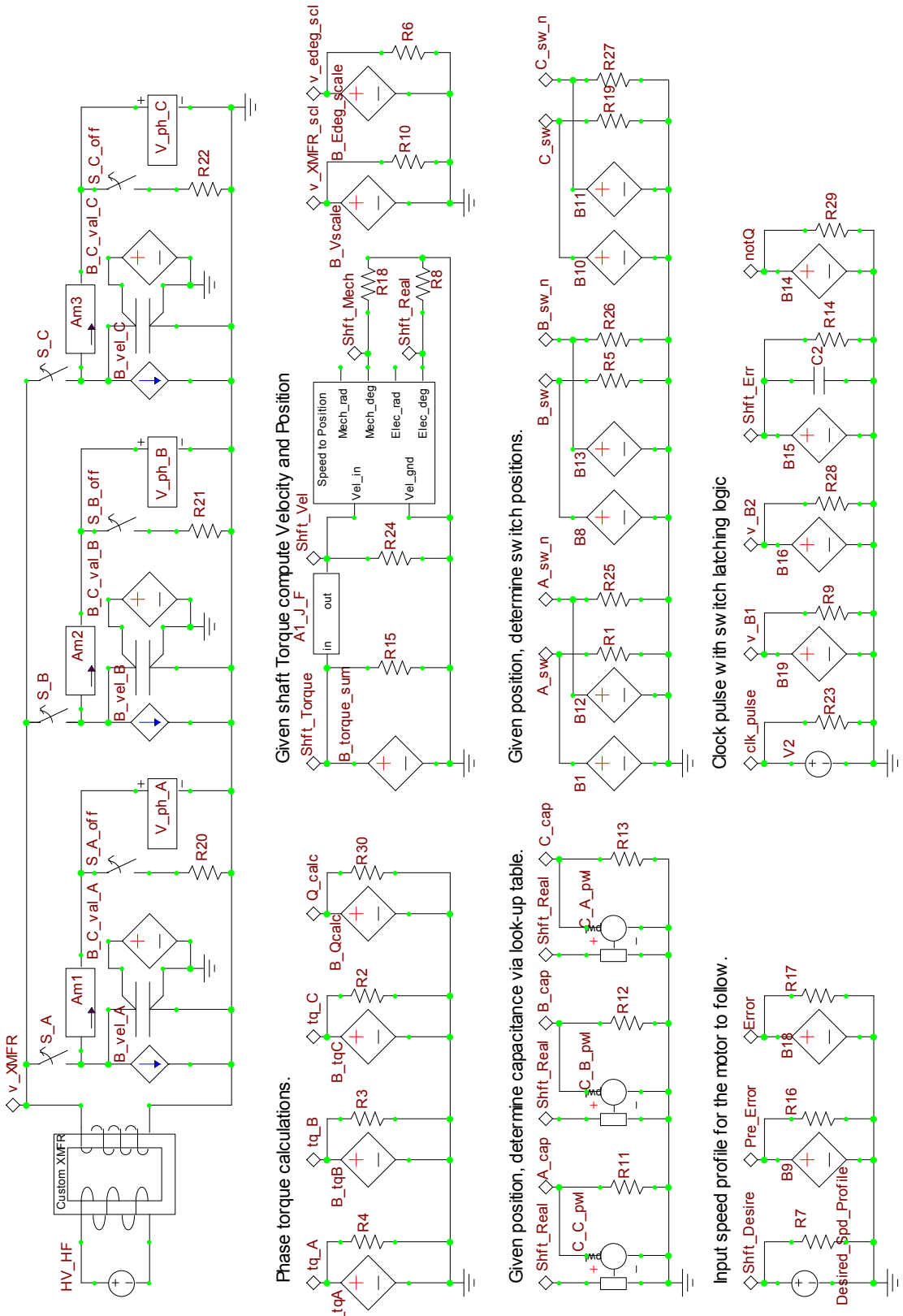

Figure 121 Dynamic ESM B2Spice Model

6.5 Dynamic Simulation Results

Using the SIM mechanical parameters described previously, a simulation of its dynamic operation has been completed and is shown below. The simulated motor operates using an HFHV source with a peak voltage of 1.1kV and a dielectric of Kapton HN25.

The simulation control input is a desired speed profile, shown in Figure 122. The profile begins by increasing speed from 0 to 2π rad/s before reaching a plateau that is held for 1 sec. This speed is then quickly decelerated to 0 rad/s which is held. The profile shows acceleration and deceleration for the motor with a computed mass moment of inertia of 0.01107 kg*m^2 that is inclusive of the glass and shaft and an assumed coefficient of friction of 0.01 representing the friction of the shaft bearing.

Figure 123 through Figure 125 show the computed complete, initial and final profiles of capacitance respectively. Figure 125 shows slight oscillation of the capacitance representing motion of the shaft, but is limited to rough 10pF. This oscillation at the shaft is better seen with Figure 126 showing the desired speed profile and the achieved shaft profile which tends to slightly overshoot the desired profile. The degree of overshoot can be controlled with tighter control parameters.

Figure 127 shows the achieved torque profile and its RMS value. The torque profile has both positive and negative components as expected due to the HF voltage source.

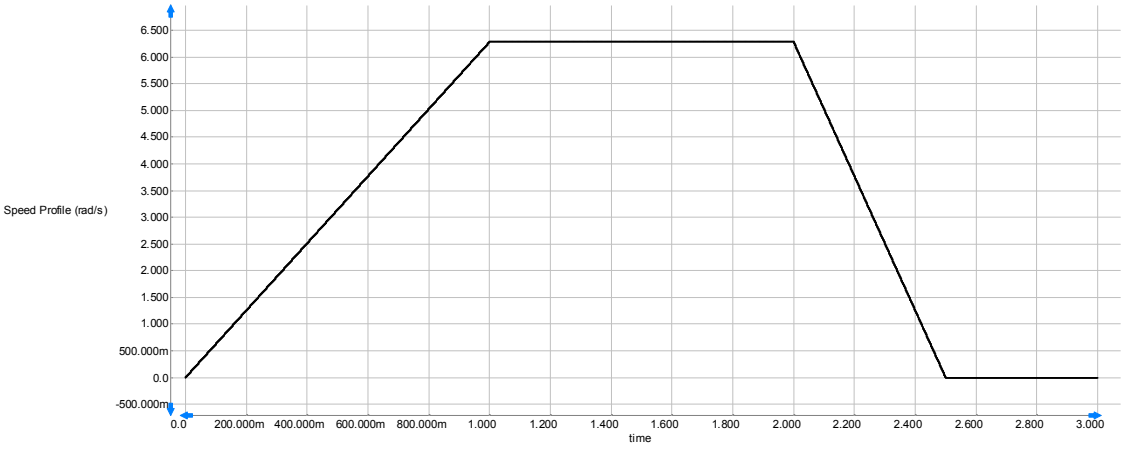

Figure 122 Desired Speed Profile

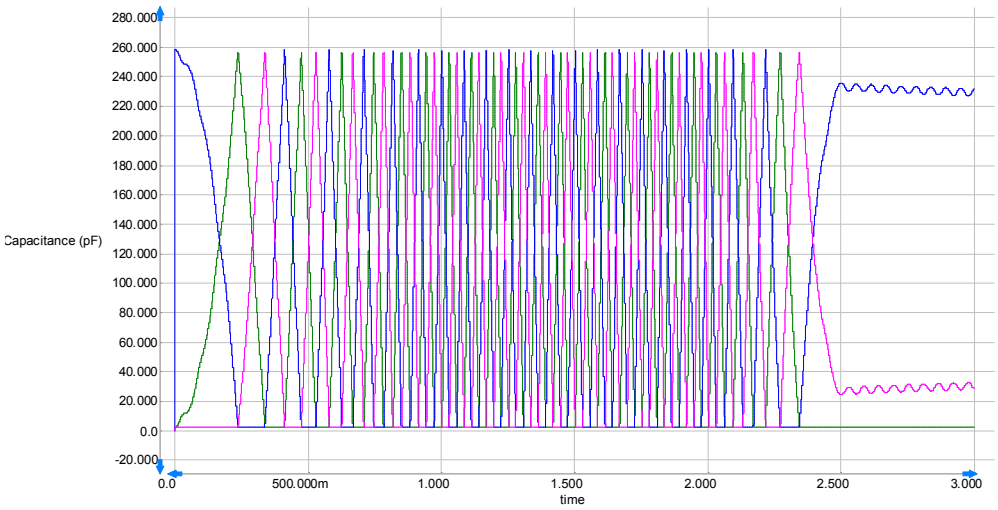

Figure 123 Capacitance Profile for Complete Simulation

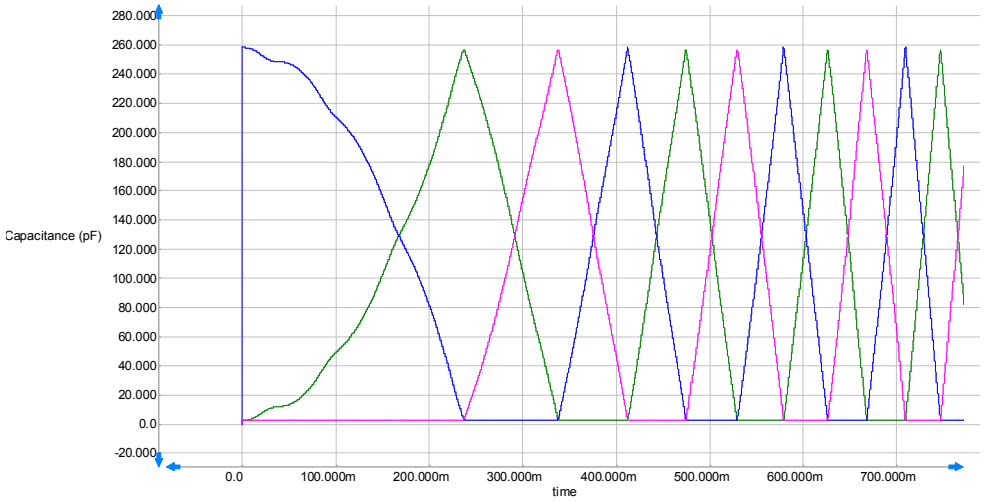

Figure 124 Initial Capacitance Profile

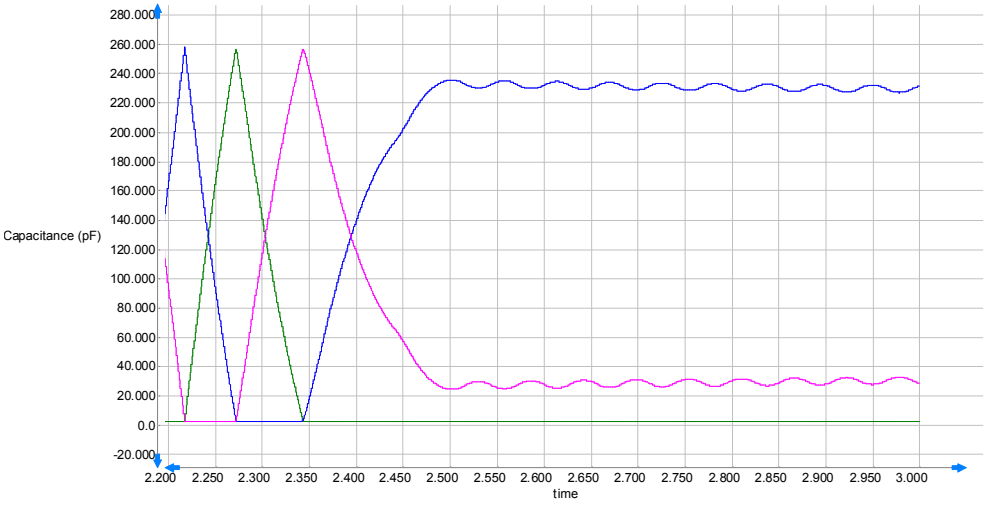

Figure 125 Final Capacitance Profile

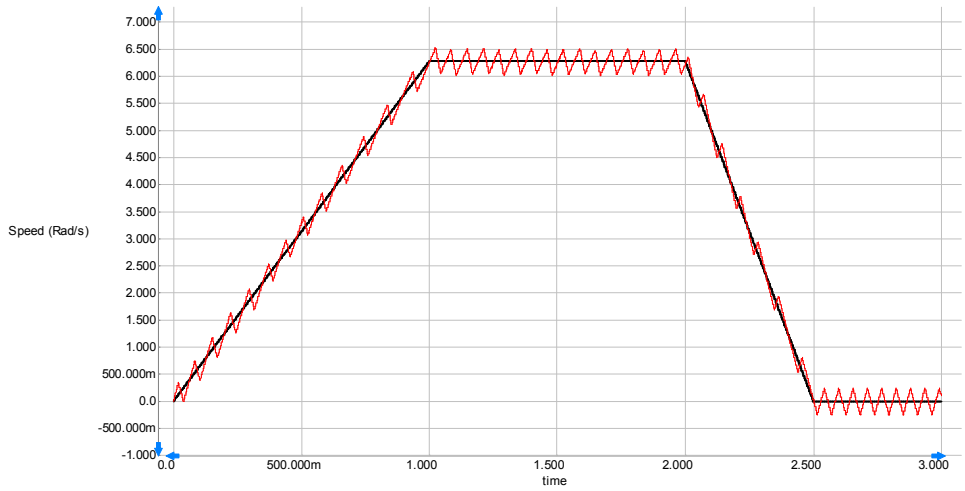

Figure 126 Desired and Simulated Speed Profile

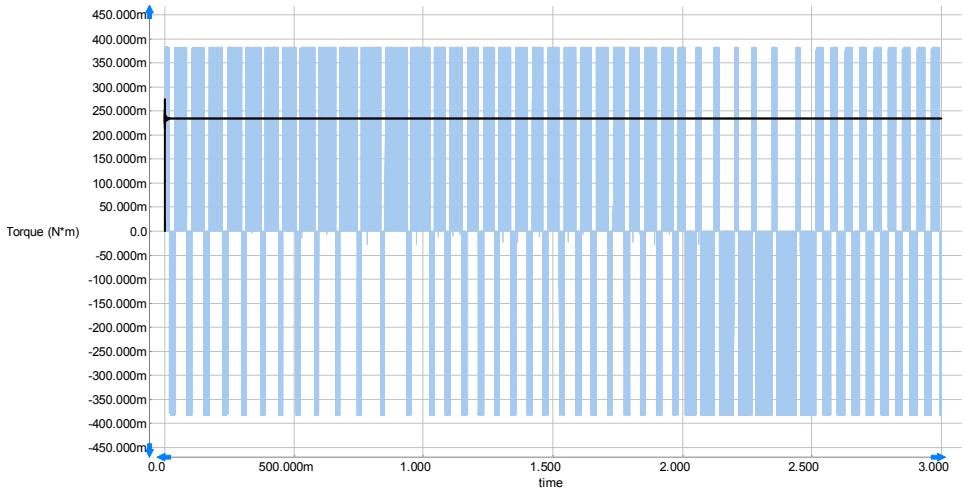

Figure 127 Torque and RMS Torque

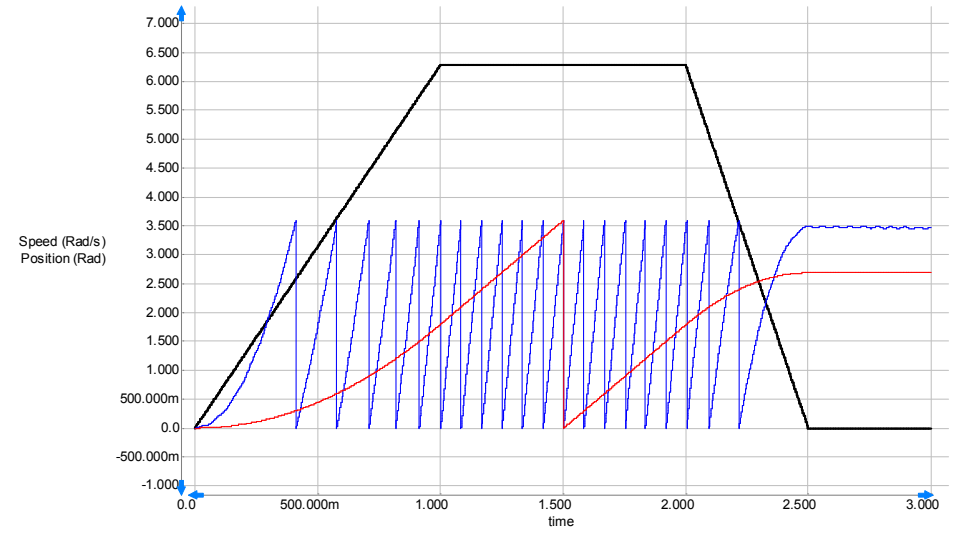

Figure 128 Mechanical and Electrical Position with Speed Profile

Figure 128 compares the desired speed profile with the computed mechanical and electrical shaft positions. Note that there are 12 electrical rotations for 1 completed mechanical rotation, the first and only complete rotation occurs at 1.5s. The 12 electrical rotations of the three phases motor wherein each phase consumes 10degs of rotation thus equaling one 360deg mechanical rotation (12rotations*3ph/rotation*10deg/ph=360deg).

Figure 129 through Figure 131 show the desired speed profile with each pulse pattern of the three phases respectively. Note that only one phase is able to operate at a given time, but because of the bang-off-bang control scheme, two phases are needed to control speed, one to increase speed while another is used to decrease it. While one phase is able to produce positive torque to increase speed, another phase is able to produce negative torque to slow it down in such a way that the rotor shaft meets any given error conditions. This oscillation around the desired speed profile can been see in with Figure 126.

Figure 132 shows the HFHV pulsing pattern described previously in Figure 107. For clarity, positive or negative torque on the shaft is developed due to the phase pulsing (stepping) pattern and not the polarity of the voltage because voltage is a squared value in force development.

Figure 133 shows the computed charge vs voltage (Q vs V) diagram for the simulated SIM. Figure 134 shows a typical charge vs voltage (Q vs V) diagram with capacitance rotation cycle imposed upon it. As mentioned in Chapter 4, this diagram is similar to the flux vs current (λ vs i) diagrams for induction machines, although there are several differences. The first difference is that saturation does not play a role in ESMs and thus the capacitance curves are linear. Second, note that the diagram is completely shaded rather than encompassing only the outer edge. This is because the voltage source is alternating, thus the charge also alternates from zero to its maximum value for the given position. Also, the unaligned position will have virtually zero capacitance as the rotor and stator plates do not overlap in the unaligned position, thus any capacitance in this position will be limited to parasitic ones. The final primary difference between the induction and capacitive machine plots is that the corners of the rotation cycle will be sharp and any curvature will be either purposefully placed or due to parasitic capacitances.

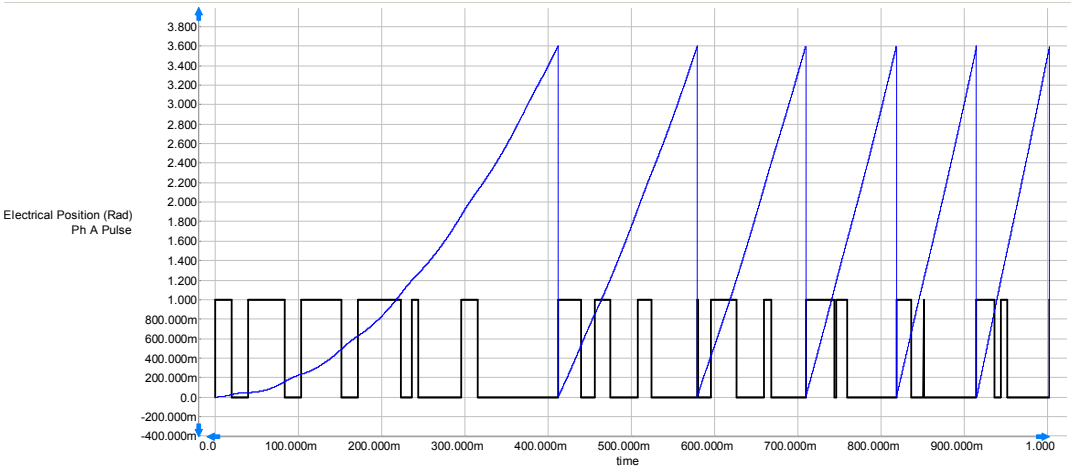

Figure 129 Electrical Position with Phase A Pulse

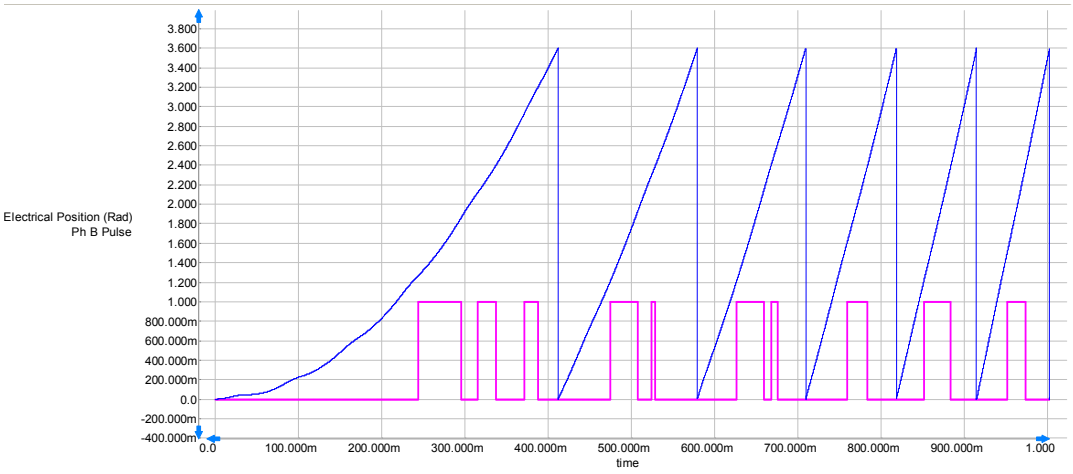

Figure 130 Electrical Position with Phase B Pulse

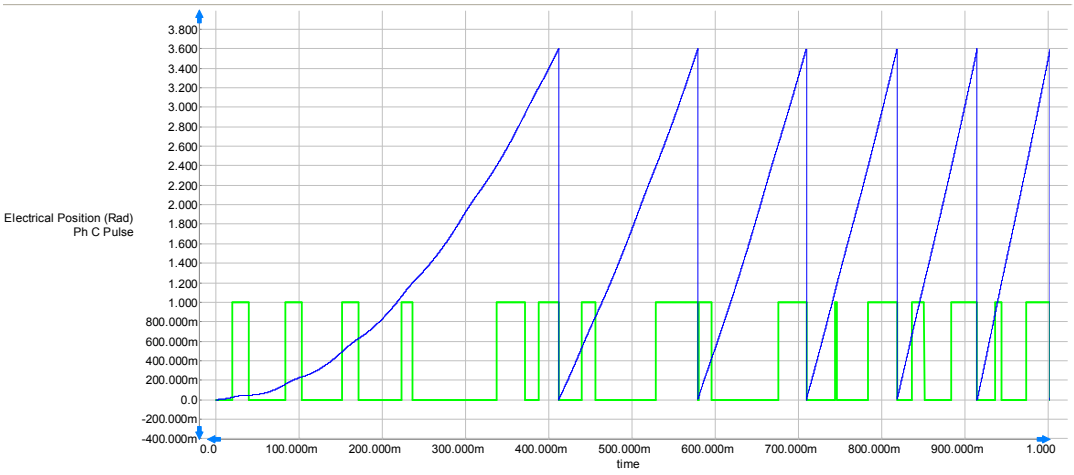

Figure 131 Electrical Position with Phase C Pulse

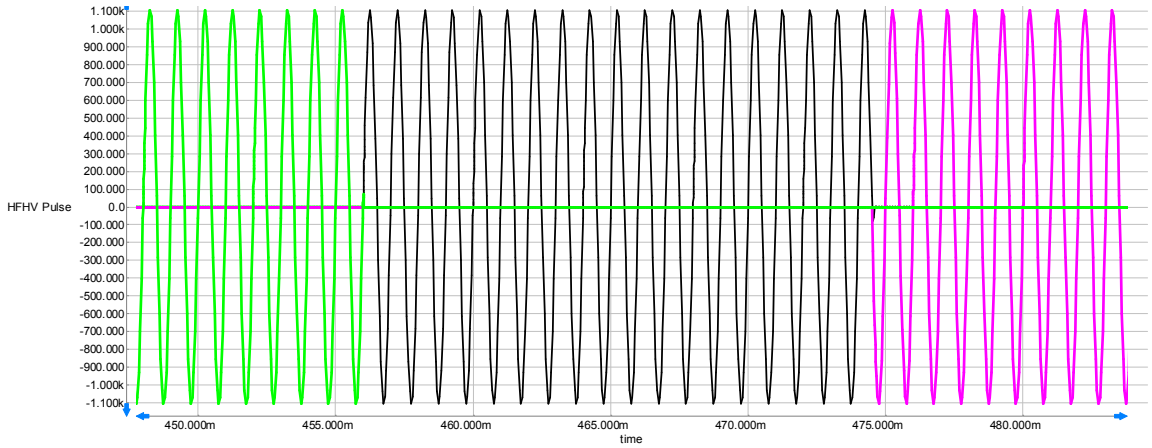

Figure 132 HFHV Sample Pulse (Ph C left, Ph A center, Ph B right)

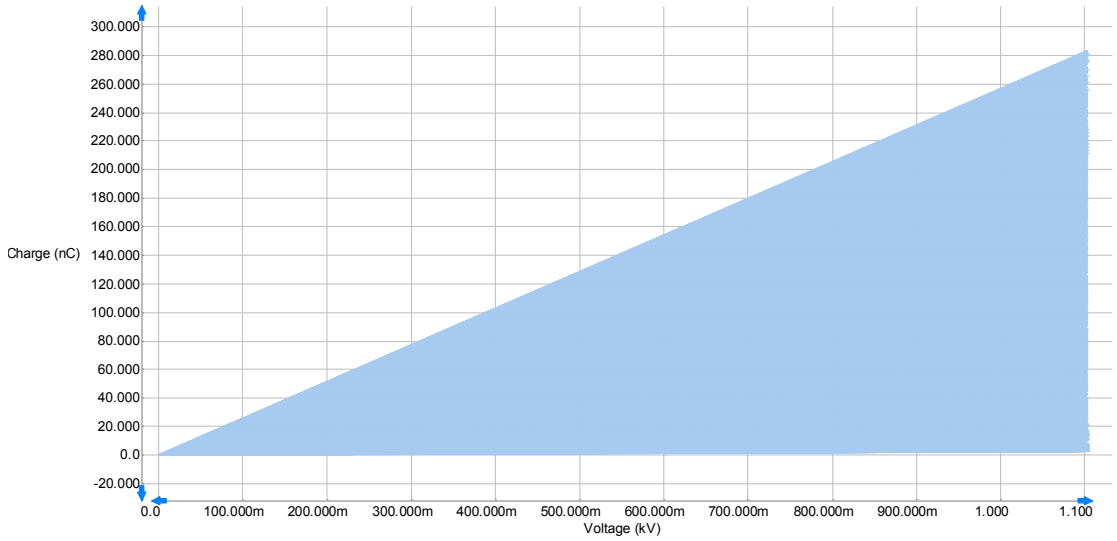

Figure 133 Simulated Q vs V Diagram

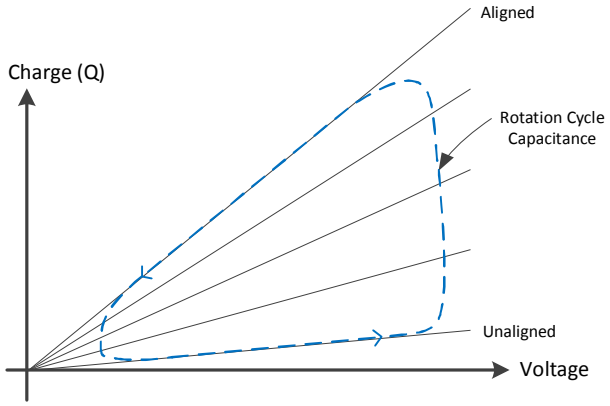

Figure 134 Typical Q vs V Diagram

6.6 Conclusion

This chapter began with a discussion how to remove a charge once it had been placed. For ease, an alternating voltage source was utilized because it inherently drives the charge to zero twice per cycle. Following this, a discussion of a pulsed switching scheme was presented as a means to control the SIM with this alternating source. The discussion included a simple drive topology overview to implement this control scheme. A detailed analysis of the control scheme then followed that showed how to implement a bang-off-bang control method that was supportive of the HV source and allowed switching to occur when the voltage was at a natural zero crossing point. A dynamic simulation that implemented all of these control features as well as the unique traits of the SIM was then presented. This section discussed how a variable capacitor for the simulation was modeled and how its physical parameters, load, mass, etc., were input as characteristics of the model. This chapter then concluded with results of the simulation showing the unique results of the control system and SIM.

Chapter 7 Conclusions and Future Work

Chapter 1 began with a discussion and comparison of forces developed from electrical means. The discussion described the prime methods to develop them and how they could be generated. It was shown that, while electrostatic methods do not presently have the greatest force density, it does, however have the potential to surpass that of traditional induction based magnetic field methods within certain boundaries.

With the understanding that ES force methods have potential advantages over traditional induction based methods, a historical development of the electrostatic motor, starting with Benjamin Franklin in 1748 with his spark gap motor, and a brief description of various topologies was presented in order to provide scope and background to the field of research. With this further understanding of the ES topologies, the switched impedance motor topology was chosen for further development for its applicability to industry and greater power density among the topologies.

Chapter 3 presented SIM design fundamentals which included a detailed model for force development for the linear case. As part of this modeling of force development, a design methodology for development of a SIM was presented. The chapter continued with a detailed description of electric field breakdown and the mechanisms that lead to it, some of which have inhibited prior development of this topology. With the understanding of air gap breakdown, an analytic model of the field in the gap was developed and presented. It was shown that while the field of the leading edge could be solved directly with a basic assumption, the trailing edge field, which has no easily defined boundary, necessitated the need for a conformal map to solve for the field with relative ease and to do so analytically. The analytic models of the leading edge, direct air gap and lagging edges were developed methodically, with graphical outputs for clarity. Chapter 3 concluded with the development of a linear force model used to predict experimental results.

Chapter 4 presented experimental results which began with empiric measurements of field breakdown with an air gap at 1atm. This experiment was necessary to define the upper boundary of achievable fields and applied voltages for a given gap size. The plot of field breakdown versus gap confirmed that breakdown of the gap is not linear for small gaps, nor does it follow the ideal Paschen curve.

Using the measured Paschen curve data to define the upper boundary for field breakdown, an experimental rig to measure linear forces was presented. The design and theory of operation for this linear force rig and how it was to measure micron displacements and forces was then presented in detail. The results of this experimental setup were compared with FEA results for relatively large gaps, as smaller gaps presented an issue with computer processing power. The FEA results compared closely to the calculated value, maintaining a percent difference at or below 20% in most cases. Empiric test results from the force rig were then presented for small gaps, gaps that would be applicable for approaching densities of magnetic machines. These tests showed close agreement between the analytic and experimental models, despite an imperfect test rig.

Using the validated analytic model, Chapter 5 presented a dynamic SIM mechanical design. The forces of a rotation system were presented which led to a development of how electrical energy can be converted to useful mechanical energy in a motor. The development led to the creation of a single phase equivalent SIM circuit model. Utilizing this circuit, a complete electro-mechanical control model, as well as a mechanical design embodying the principals and lessons learned previously, was then presented.

Using the physical constraints of the mechanical SIM design and developed circuit model, a simulation of the full system was then presented in Chapter 6. In addition to presenting charge versus voltage plots, as well as other models, the simulation model presented a novel high frequency high voltage control scheme that utilized a bang-off-bang switching method that complimented the SIM control structure and allowed for inherent removal of charge from stator plates. The simulation, developed in B2Spice®, represented the complete ESM system as an equivalent electrical circuit.

The motor drive, while utilizing existing components, is in its infancy and has vast potential for development. The measured Paschen curve plots showed that, in combination with small gaps, existing solid state switching technology is sufficient for control and operation of SIMs, thus seeking to define future goals for this field is unnecessary. However, the plots also show that, because of breakdown, a gap medium of air will continue to require extreme gap tolerance control to be successful. Although achievable, by utilizing novel fluids with high permittivity, such as de-ionized water with its own dielectric strength of 60kV/cm and a relative permittivity of 80, the SIM topology begins to encroach on the stress values of the induction motor and allows a SIM with a gap of 25µm (1mil) to be more easily achieved. With this in mind,

should future material researchers be able to achieve a relative permittivity of 1000 in a gaseous or low density fluid to reduce drag medium, then it is possible for a SIM to achieve stress density that is equivalent to an induction machine with very achievable gaps of 100µm (4mil), as shown in Figure 135.

The development of the presented analytic models and empiric results show the potential for this motor topology. Future work for the SIM topology includes development of new dielectric materials that could be conformally coated to conduction plates to limit parasitic friction. Conformal coatings could be in the form of Kapton® or something similar, but they could also exist as a dielectric gas or liquid. Now that design tools and models have it has been shown to be achievable, the purpose of future work is to find an appropriate material and environmental combination that permits the gap to be expanded to ease manufacturing constraints, yet achieve a force density equal to, or better than, that of traditional induction machines. By enlarging the gap, manufacturing costs are reduced. By exceeding the stress density of induction machines, coupled with the greater efficiency and lower weight of this topology, the SIM will be a true market contender against the induction machine.

The work presented here has shown that the SIM has many advantages over induction machines and that SIMs that embody these advantages are achievable. Through insightful use of the models presented herein with existing or emerging dielectric materials, an economically viable SIM with superior force density and efficiency can be created. The creation of this SIM motor will mean that existing global energy supplies will be conserved through lower energy use.

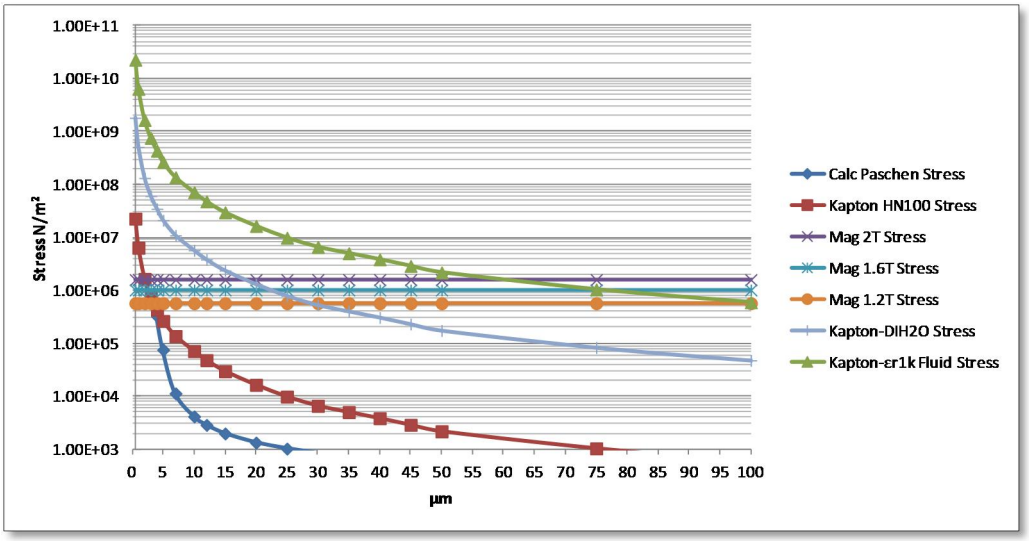

Figure 135 Stress Comparason with DI Water

Appendix A: Minkowski Force per Unit Volume Equation

Expand the Lorentz Force Equation (1).

$$\vec{F} = q\overrightarrow{(E} + v \times \vec{B}) = q\vec{E} + \vec{J} + \vec{B}$$

Use Maxwell's first and third Equation and substitute for q and J.

$$\vec{F} = \vec{E}(\nabla \times \vec{D}) + \left[\frac{1}{\mu}(\nabla \times \vec{B}) - \varepsilon\frac{\partial \vec{E}}{\partial t}\right] \times \vec{B}$$

Expand and rewrite the terms.

$$\vec{F} = \varepsilon\vec{E}(\nabla \cdot \vec{E}) + \frac{1}{\mu}\left[(\nabla \times \vec{B}) \times \vec{B}\right] - \varepsilon\frac{\partial \vec{E}}{\partial t} \times \vec{B}$$

The last term can be rewritten as shown.

$$\varepsilon\frac{\partial \vec{E}}{\partial t} \times \vec{B} = \varepsilon\frac{\partial}{\partial t}(\vec{E} \times \overrightarrow{B)} - \varepsilon\vec{E} \times \frac{\partial \vec{B}}{\partial t} = \varepsilon\frac{\partial}{\partial t}(\vec{E} \times \overrightarrow{B)} - \varepsilon\vec{E} \times (\nabla \times \vec{E})$$

Substitute the last term back in and rewrite.

$$\vec{F} = \varepsilon\vec{E}(\nabla \cdot \vec{E}) + \frac{1}{\mu}\left[(\nabla \times \vec{B}) \times \vec{B}\right] - \varepsilon\frac{\partial}{\partial t}(\vec{E} \times \overrightarrow{B)} - \varepsilon\vec{E} \times (\nabla \times \vec{E})$$

$$= \varepsilon\vec{E}(\nabla \cdot \vec{E}) - \varepsilon\vec{E} \times (\nabla \times \vec{E}) + \frac{1}{\mu}\left[(\nabla \times \vec{B}) \times \vec{B}\right] - \varepsilon\frac{\partial}{\partial t}(\vec{E} \times \overrightarrow{B)}$$

Substituting Maxwell's first Equation, realizing that it is zero, can make the equation symmetric.

$$\vec{F} = \varepsilon\left[\vec{E}(\nabla \cdot \vec{E}) - \vec{E} \times (\nabla \times \vec{E})\right] + \frac{1}{\mu}\left[\vec{B}(\nabla \cdot \vec{B}) - (\nabla \times \vec{B}) \times \vec{B}\right] - \varepsilon\frac{\partial}{\partial t}(\vec{E} \times \overrightarrow{B)}$$

Expand the operators and recombine in tensor notation.

$$\vec{F} = \nabla \cdot \left[\left(\varepsilon\overrightarrow{E_\iota E_J} - \frac{1}{2}E^2\right) + \left(\varepsilon\overrightarrow{B_\iota B_J} - \frac{1}{2}B^2\right)\right] - \varepsilon\frac{\partial}{\partial t}(\vec{E} \times \overrightarrow{B)} = \nabla \cdot \Pi - \frac{\partial}{\partial t}(\vec{D} \times \vec{B})$$

Maxwell's stress tensor is Π and the last term is known as the electromagnetic momentum vector as it is a force that varies with the time rate of change.

Starting with Equation (11) and inserting it into Poisson's Equation, allows the voltage and electric field of an ion propulsion system to be computed.

$$v(x) = \sqrt{\frac{2q(V_{Max} - V_0)}{m}} \tag{11}$$

$$\nabla \cdot \vec{E} = -\nabla^2 V = \frac{\rho}{\varepsilon}$$

Let $\rho = \frac{Nq}{A}$ and $J = \frac{Nqv}{A} = const$ when in steady state. Now, $\rho = \frac{J}{v}$ and we can expand.

$$\nabla^2 V = -\frac{J}{\varepsilon}\left[\frac{2q(V_{Max} - V_0)}{M}\right]^{-\frac{1}{2}} = -\frac{J}{\varepsilon}\left[\frac{M}{2q(V_{Max} - V_0)}\right]^{\frac{1}{2}}$$

Note that $\nabla^2 V = \frac{d^2V}{dx^2} = \frac{d}{dx}\left(\frac{dV}{dx}\right)$. Now, multiply both sides by $2\frac{dV}{dx}$ and expand in order to collect terms and eventually simplify.

$$\left(2\frac{dV}{dx}\right)\frac{d}{dx}\left(\frac{dV}{dx}\right) = -\frac{2J}{\varepsilon}\left[\frac{M}{2q(V_{Max} - V_0)}\right]^{\frac{1}{2}}\left(\frac{dV}{dx}\right)$$

Letting $\acute{V} = \frac{dV}{dx}$ and recognizing that $2\acute{V}\frac{d\acute{V}}{dx} = \frac{d(\acute{V})^2}{dx}$ now allows both sides to be integrated with respect to x.

$$\int \frac{d(\acute{V})^2}{dx}dx = -\frac{2J}{\varepsilon}\sqrt{\frac{M}{2q}}\int \frac{1}{\sqrt{V_{Max} - V_0}}\acute{V}dx$$

Now simplify.

$$\int d(\acute{V})^2 = -\frac{2J}{\varepsilon}\sqrt{\frac{M}{2q}}\int \frac{1}{\sqrt{V_{Max} - V_0}}dV$$

$$\left(\frac{dV}{dx}\right)^2\Big|_{Max} - \left(\frac{dV}{dx}\right)^2\Big|_{a} = -\frac{4J}{\varepsilon}\sqrt{\frac{M(V_{Max} - V_0)}{2q}}$$

Ion density will be maximized at the ion source but will decrease with distance as ions are accelerated away but the electric field. For this reason, the field near the source will have a limit of zero and be maximized at the acceleration grid. For this reason $\left(\frac{dV}{dx}\right)^2\Big|_{Max} \approx 0$.

$$\left.\frac{dV}{dx}\right|_a = 2\sqrt{\frac{J}{\varepsilon}}\sqrt[4]{\frac{M(V_{Max}-V_0)}{2q}}$$

Finally, the electric field at the acceleration grid can be computed.

$$E_a = -\left(\frac{dV}{dx}\right)_a$$

Force is defined as the product of the stored charge and electric field.

$$\vec{F} = Q\vec{E}$$

The charge can be rewritten in terms of the electric field and the electric flux density.

$$\nabla \cdot \vec{D} = \rho$$

$$Q = \oint_V \rho \cdot dV = \oint_V \nabla \cdot \vec{D} = \oint_V \nabla \cdot \varepsilon\vec{E}$$

Rewrite the charge in terms of terms of a tensor and volume integral.

$$\nabla \cdot \varepsilon\vec{E} = \frac{\partial(\varepsilon\vec{E}_x)}{\partial x} + \frac{\partial(\varepsilon\vec{E}_y)}{\partial y} + \frac{\partial(\varepsilon\vec{E}_y)}{\partial y} = \sum_{j=1}^{3} \frac{\partial(\varepsilon\vec{E}_j)}{\partial j}$$

$$Q = \oint_V \sum_{j=1}^{3} \frac{\partial(\varepsilon\vec{E}_j)}{\partial j}$$

Now substitute this new definition for charge back into the force question.

$$\vec{F} = \oint_V \sum_{j=1}^{3} \frac{\partial(\varepsilon\vec{E}_j)}{\partial j} dV * \vec{E} = \overrightarrow{F_X} + \overrightarrow{F_X} + \overrightarrow{F_X} = Q\overrightarrow{E_X} + Q\overrightarrow{E_Y} + Q\overrightarrow{E_z}$$

For an arbitrary direction ‘k’, force is now solved via the following. Here, ‘j’ represents the direction of a surface where charge exists and ‘k’ is the direction of force to be determined.

$$\overrightarrow{F_k} = Q\overrightarrow{E_k} = \oint_V \frac{\partial(\varepsilon\vec{E}_j)}{\partial j} dV * \overrightarrow{E_k}$$

Because $\overrightarrow{E_k}$ is a constant, it can be moved inside the integral.

$$\overrightarrow{F_k} = Q\overrightarrow{E_k} = \oint_V \frac{\partial(\varepsilon\vec{E}_j\overrightarrow{E_k})}{\partial j} dV$$

The partial derivative can now be rewritten.

$$\frac{\partial(\varepsilon\vec{E}_j\overrightarrow{E_k})}{\partial j} = \frac{\partial(\varepsilon\vec{E}_j)}{\partial j}\overrightarrow{E_k} + \frac{\partial(\overrightarrow{E_k})}{\partial j}\ \varepsilon\vec{E}_j$$

$$\frac{\partial(\varepsilon\vec{E}_j)}{\partial j}\overrightarrow{E_k} = \frac{\partial(\varepsilon\vec{E}_j\overrightarrow{E_k})}{\partial j} - \frac{\partial(\overrightarrow{E_k})}{\partial j}\,\varepsilon\vec{E}_j$$

Now substitute this back into the original force equation. While the equations are equivalent, the substitution allows for future geometric simplifications.

$$\overrightarrow{F_k} = Q\overrightarrow{E_k} = \oint_V \left[\frac{\partial}{\partial j}(\varepsilon\vec{E}_j\overrightarrow{E_k}) - \varepsilon\vec{E}_j\frac{\partial}{\partial j}(\overrightarrow{E_k})\right]dV$$

If $j \neq k$ then the second term is zero. Utilize the delta operator to help simplify.

$$\overrightarrow{F_k} = Q\overrightarrow{E_k} = \oint_V \left[\frac{\partial}{\partial j}(\varepsilon\vec{E}_j\overrightarrow{E_k}) - \mathcal{L}_{jk}\left(\varepsilon\vec{E}_j\frac{\partial}{\partial j}(\overrightarrow{E_k})\right)\right]dV$$

$$\mathcal{L}_{jk} = \begin{cases} 1\ if\ j = k \\ 0\ if\ j \neq k \end{cases}$$

If $j = k$ then another simplification can be made.

$$\varepsilon\vec{E}_j\frac{\partial}{\partial j}(\overrightarrow{E_k}) = \varepsilon\frac{\partial}{\partial j}(\overrightarrow{E_j E_k}) = \varepsilon\left[\overrightarrow{E_k}\frac{\partial}{\partial j}(\overrightarrow{E_j}) + \overrightarrow{E_j}\frac{\partial}{\partial j}(\overrightarrow{E_k})\right] = 2\varepsilon\overrightarrow{E_{k=j}}\frac{\partial}{\partial j}(\overrightarrow{E_{k=j}})$$

Substitute this back into the force equation.

$$\overrightarrow{F_k} = Q\overrightarrow{E_k} = \oint_V \left[\frac{\partial}{\partial j}(\varepsilon\vec{E}_j\overrightarrow{E_k}) - \mathcal{L}_{jk}\left(\frac{\varepsilon}{2}\frac{\partial}{\partial j}(\vec{E}_j\overrightarrow{E_k})\right)\right]dV$$

$$= \oint_V \left[\frac{\partial}{\partial j}(\varepsilon\vec{E}_j\overrightarrow{E_k}) - \mathcal{L}_{jk}\left(\frac{\varepsilon}{2}\left(\vec{E}_{j=k}{}^2\right)\right)\right]dV$$

Now that a generalized simplification has been found, reconsider the larger application.

$$\vec{F} = \vec{F}_x + \vec{F}_y + \vec{F}_z = \oint_V \left[\frac{\partial}{\partial x}(T_x) + \frac{\partial}{\partial y}(T_y) + \frac{\partial}{\partial z}(T_z)\right]dV = \oint_V (\nabla\cdot T)\mathrm{dV}$$

Thus,

$$\overrightarrow{F_k} = \oint_V (\nabla\cdot T_k)\mathrm{dV}$$

Now utilize the divergence theorem to transform the volume integral into a surface integral.

$$\overrightarrow{F_k} = \oint_V (\nabla\cdot T_k)\mathrm{dV} = \oint_V (\nabla\cdot T_k)\mathrm{dV} = \oint_S \left(T_{jk}\hat{n}_j\right)ds$$

Finally, we have a simplified force representation based upon an integration over surfaces. In this representation, 'k' is the direction that we want to determine the force and 'j' is the direction of the surface creating the force.

$$\overrightarrow{F_k} = \oint_S \left(\left(\varepsilon \vec{E}_j \overrightarrow{E_k} \right) - \mathcal{L}_{jk} \left(\frac{\varepsilon}{2} \left(\vec{E}_{j=k}{}^2 \right) \right) \hat{n}_j \right) ds$$

To compute the force using the figure below, consider the upper plate as fixed while the lower plate is allowed to slide along the x-axis.

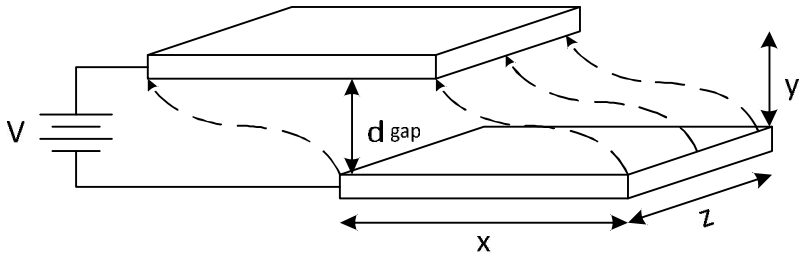

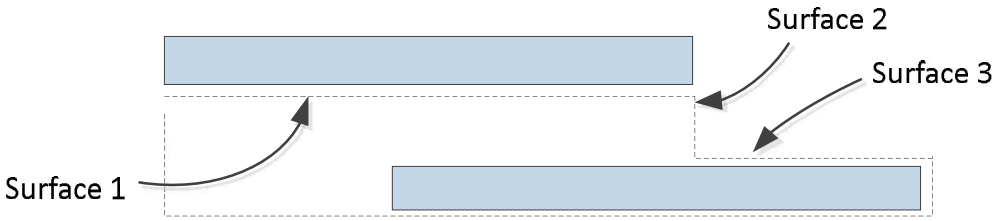

To determine the force in any direction, consider a surface a small differential (dl) height above or below each plate surface.

Now, compute $\overrightarrow{F_x}$.

$$\overrightarrow{F_x} = \iint_{zx} \left(\left(\varepsilon \vec{E}_y \overrightarrow{E_x} \right) - \mathcal{L}_{yx} \left(\frac{\varepsilon}{2} \left(\vec{E}_y \vec{E}_x \right) \right) \hat{n}_j \right) dxdz$$
$$+ \iint_{zy} \left(\left(\varepsilon \vec{E}_y \overrightarrow{E_x} \right) - \mathcal{L}_{xx} \left(\frac{\varepsilon}{2} \left(\vec{E}_x{}^2 \right) \right) \hat{n}_j \right) dydz$$
$$+ \iint_{zx} \left(\left(\varepsilon \vec{E}_y \overrightarrow{E_x} \right) - \mathcal{L}_{yx} \left(\frac{\varepsilon}{2} \left(\vec{E}_y \vec{E}_x \right) \right) \hat{n}_j \right) dxdz$$

Recall that the delta operation variables are only valid when the field and desired direction of force are in the same direction. Thus $\overrightarrow{F_x}$ can be simplified to the following.

$$\overrightarrow{F_x} = \iint_{zy} \left(\frac{\varepsilon}{2}\left(\vec{E}_x{}^2\right)\right) dydz = -\iint_{zy} \left(\frac{\varepsilon}{2}\left(\frac{V}{y_{gap}}\right)^2\right) dydz = -\frac{\varepsilon V^2}{2}\iint_{zy} \left(\left(y_{gap}\right)^{-2}\right) dydz$$
$$= \frac{1}{2}\frac{\varepsilon z}{y_{gap}} V^2$$

Now, compute $\overrightarrow{F_y}$.

$$\overrightarrow{F_y} = \iint_{zx} \left(\left(\varepsilon \vec{E}_y \overrightarrow{E_x}\right) - \mathcal{L}_{yx}\left(\frac{\varepsilon}{2}\left(\vec{E}_y \vec{E}_x\right)\right)\hat{n}_j\right) dxdz$$
$$+ \iint_{zy} \left(\left(\varepsilon \vec{E}_y \overrightarrow{E_x}\right) - \mathcal{L}_{xx}\left(\frac{\varepsilon}{2}\left(\vec{E}_x{}^2\right)\right)\hat{n}_j\right) dydz$$
$$+ \iint_{zx} \left(\left(\varepsilon \vec{E}_y \overrightarrow{E_x}\right) - \mathcal{L}_{yx}\left(\frac{\varepsilon}{2}\left(\vec{E}_y \vec{E}_x\right)\right)\hat{n}_j\right) dxdz$$

Assume that surface 2 is at the leading edge of the top plate. With this assumption, then surface 3 has no overlap and thus no force.

$$\overrightarrow{F_y} = \iint_{zx} \left(\varepsilon \vec{E}_y{}^2 - \frac{\varepsilon}{2}\varepsilon \vec{E}_y{}^2\right) dxdz = \frac{1}{2}\varepsilon \vec{E}_y{}^2 \iint_{zy} 1\, dxdz = \frac{1}{2}\varepsilon \vec{E}_y{}^2 xz = \frac{1}{2}\varepsilon A_{ovrlap}\left(\frac{V}{y_{gap}}\right)^2$$

Differential Adjuster for Optic Mounts

The DM22 differential adjuster uses two leadscrews; one pushes the center spindle forward at 400µm per revolution and one pulls it back at 375µm per revolution. The resultant total forward motion of the center spindle is thus 25µm per revolution of the graduated knob. Each small graduation of the fine control knob is 0.5µm; the smallest incremental move for the DM22 is approximately 50nm.

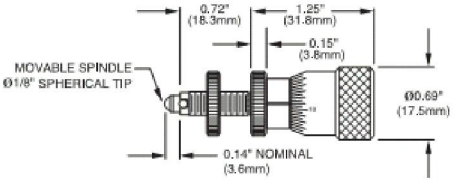

Fine Adjustment
- 250µm Range
- 25µm/rev

Coarse Adjustment
- 0.73" Long 1/4"-80 Threads
- 0.012"/rev (80 TPI)

ITEM#	$	£	€	RMB	DESCRIPTION
DM22	$ 94.00	£ 59.20	€ 87.40	¥ 897.70	Differential Adjuster 1/4"-80 External Thread

Differential Adjuster for Translation Stages: 1/2" and 1.0" of Travel

The DM12 and DM10 use the same internal mechanism as the DM22 (described above). These models are designed specifically for use in our 1/2" (13mm) and 1" (25mm) translation stages (See pages 260-263).

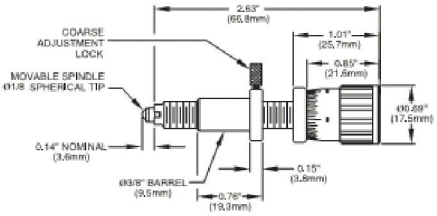

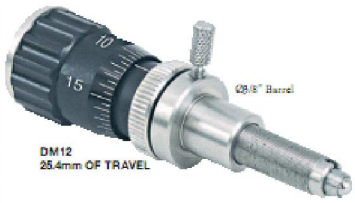

Fine Adjustment
- 250µm Range
- 25µm/rev

Coarse Adjustment
- 1" (25.4mm) for DM12
- 1/2" (12.7mm) for DM10

ITEM#	$	£	€	RMB	DESCRIPTION
DM10	$ 96.00	£ 60.50	€ 89.30	¥ 916.80	Differential Adjuster, 1/2" (12.7mm) of Coarse Travel
DM12	$ 99.00	£ 62.40	€ 92.10	¥ 945.50	Differential Adjuster, 1" (25.4mm) of Coarse Travel

1/4"-80 Fine Hex Adjuster Locking Nut

- Compatible with Any Thorlabs 1/4"-80 Adjuster
- Minimal Beam Shift When Locking Mirror Mount Actuator
- Make any Mount with 1/4"-80 Adjusters Lockable

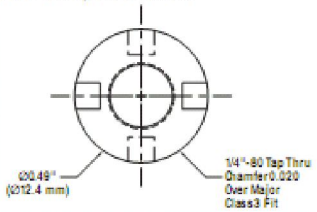

KM100 with LN2580
KM100 Sold Separately

Please refer to our website for complete models and drawings.

ITEM#	$	£	€	RMB	DESCRIPTION
LN2580	$ 8.00	£ 5.55	€ 7,20	¥ 67.60	1/4"-80 Lock Nut

Differential Adjuster Screw

The DAS110 is a standard 1/4"-80, 1.00" long adjuster screw with an internal differential adjustment mechanism. The fine adjustment is actuated by inserting a hex wrench through the clearance hole in the adjuster knob. Every rotation of the DAS110 fine adjustment mechanism yields a highly demagnified displacement of just 25 µm/rev. This adjuster is ideal as a drop-in replacement for increasing the resolution on most Thorlabs' mirror mounts.

ITEM#	$	£	€	RMB	DESCRIPTION
DAS110	$ 38.00	£ 26.40	€ 33,80	¥ 320.90	Miniature Differential Adjuster

1/4"-100 UltraFine Hex Adjusters

1/4"-100 hex adjusters are commonly used when making high-precision optomechanical mounts. Mating parts can be made using a tap (ITEM# 99940, see page 514) or either the F25USN1 or F25USN2 threaded bushing. Also available for use with the 1/4"-100 hex adjusters are removable knobs and vacuum-compatible lock nuts.

Mechanical Drawings Available on the WEB

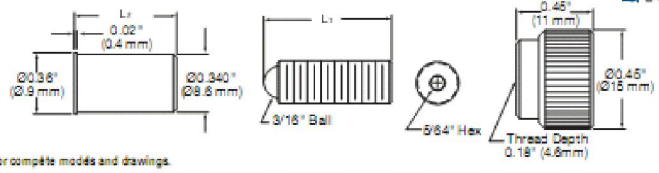

Please refer to our website for complete models and drawings.

ITEM#	$	£	€	RMB	DESCRIPTION	LENGTH
F25US050	$ 8.10	£ 5.60	€ 7,20	¥ 68.40	1/4"-100 Adjuster Screw	L1 = 1/2"
F25US075	$ 8.60	£ 5.95	€ 7,70	¥ 72.70	1/4"-100 Adjuster Screw	L1 = 3/4"
F25US100	$ 9.10	£ 6.30	€ 8,10	¥ 76.90	1/4"-100 Adjuster Screw	L1 = 1"
F25US150	$ 10.80	£ 7.50	€ 9,60	¥ 91.20	1/4"-100 Adjuster Screw	L1 = 1 1/2"
F25US200	$ 12.40	£ 8.60	€ 11,10	¥ 104.80	1/4"-100 Adjuster Screw	L1 = 2"
F25USN1	$ 9.70	£ 6.70	€ 8,70	¥ 82.00	1/4"-100 Threaded Bushing	L2 = 0.63"
F25USN2	$ 9.70	£ 6.70	€ 8,70	¥ 82.00	1/4"-100 Threaded Bushing	L2 = 0.57"
F25USK1	$ 8.10	£ 5.60	€ 7,20	¥ 68.40	1/4"-100 Removable Knob	0.45"
LN25100	$ 8.20	£ 5.70	€ 7,30	¥ 69.30	1/4"-100 Locking Nut	–

```
HV_Drive_Circuit_8a.cpr

***** subcircuit definitions

************************
* b2 spice subcircuit
************************
* pin #                 pin name
* xmfr_sec_2            xmfr_sec_2
* xmfr_sec_1            xmfr_sec_1
* xmfr_pri_1            xmfr_pri_1
* xmfr_pri_2            xmfr_pri_2
.subckt XMFR_custom xmfr_sec_2 xmfr_sec_1 xmfr_pri_1 xmfr_pri_2
***** main circuit
e_sec 14  4 13 xmfr_pri_2  2.080000000000e+001
f_pri 13  xmfr_pri_2 vi_sec  4.807692307692e-002
iv_pri 13  xmfr_pri_2 0
vi_sec xmfr_sec_2  4 0
lx_sec_leakage 14  16  ic = 0
r_sec 16  xmfr_sec_1  1.500000000000e-001
lx_core 13  xmfr_pri_2  5.000000000000e-003 ic = 0
r_core xmfr_pri_2  13  3.400000000000e+002
r_pri 19  13  1.000000000000e-001
lx_pri_leakage xmfr_pri_1  19  ic = 0
.ends

************************
* b2 spice subcircuit
************************
* pin #                 pin name
* mech_rad              mech_rad
* elec_rad              elec_rad
* 0                     vel_gnd
* vel_in                vel_in
* elec_deg              elec_deg
* mech_deg              mech_deg
.subckt Speed_to_Position mech_rad elec_rad 0 vel_in elec_deg mech_deg
***** main circuit
b_pi 5  0 v=4*atan(1)
b_shft_rad mech_rad  0 v=2*v(5,0)*(atan(tan(v(shft_angle)*v(5,0)/(2*v(5,0)) -v(5,0)/2))+v(5,0)/2) /v(5,0)
r2 mech_rad  0 1meg
r3 5  0 1meg
r4 shft_angle  0 1meg
a1 vel_in  shft_angle integrator_block
b1 elec_rad  0 v= 1.200000000000e+001 *(2*v(5,0)/( 1.200000000000e+001 ))*(atan(tan(v(shft_angle)*v(5,0)/(2*v(5,0)/
1.200000000000e+001) -v(5,0)/2))+v(5,0)/2) /v(5,0)
r1 elec_rad  0 1meg
r6 elec_deg  0 1meg
b3 elec_deg  0 v=v(elec_rad)*180/(4*atan(1))
r5 mech_deg  0 1meg
b2 mech_deg  0 v=v(mech_rad)*180/(4*atan(1))
.model integrator_block int  out_lower_limit = -1t   out_upper_limit = 1t
.ends

************************
* B2 Spice Subcircuit
************************
* Pin #                 Pin Name
* C_neg                 C_neg
* C_in_pos              C_in_pos
* 0                     C_in_neg
* C_pos                 C_pos
.Subckt Variable_Capacitor C_neg C_in_pos 0 C_pos

***** subcircuit definitions
```

```
**-- Continuous Filtering Function Macromodel --**
.SUBCKT X1_cffm 10  30  20
* Node 10= Input, Node 30= Output, Node 20= GND
RIN 10 20 1.000000e+000
BEIN 100 0 V=  V(10,20) * 1.000000e+000 - V(101) * 0.000000e+000
REI 100 0 1
G1 0 101 100 0 1
R1 101 0 1T
C1 101 0 1
BESO 102 0 V= V(100) * 0.000000e+000 + V(101) * 1.000000e+000
ROT 102 30 1.000000e+000
RDY 30 0 1T
.ENDS X1_cffm


***** main circuit
B1 5  C_neg v=v(N3,0)
B2 6  0 v = I(vam1) / (1e-12 + v(C_in_pos,0))
VAm1 C_pos  5 0
R3 C_in_pos  0  1G
XX1 6  N3  0 X1_cffm
R4 N3  0  1Meg

.ends


***** main circuit
B_C_val_C 7  0 v = v(C_cap)*10^(-12)
S_C V_C  21  C_sw 0 switch off
IV_ph_C 24  0 0
XU2 0  7  0  21 variable_capacitor
IXMFR_Hi V_C  0 0
XU1 0  8  0  18 variable_capacitor
IV_ph_B 27  0 0
S_B V_C  18  B_sw 0 switch off
B_C_val_A 15  0 v = v(A_cap)*10^(-12)
B_C_val_B 8  0 v = v(B_cap)*10^(-12)
S_A V_C  36  A_sw 0 switch on
IV_ph_A 31  0 0
R8 0  Shft_Real 1Meg
R4 30  0 1G
R3 33  0 1G
R2 57  0 1G
XC_A 0  15  0  36 variable_capacitor
B_phC_torq 57  0 v =  if( (u(v(Shft_Real)-240))=1, (v(21,0)^2)*6.547499909120e+002*10^(-12),if( ( u(120-
v(Shft_Real)))=1,-(v(21,0)^2)*6.547499909120e+002*10^(-12),0))
IC_torq 57  0 0
IB_torq 33  0 0
B_phB_torq 33  0 v =  if((u(v(Shft_Real)-120)* u(240-v(Shft_Real)))=1, (v(18,0)^2)*6.547499909120e+002*10^(-12),
if((u(v(Shft_Real)-240))=1,-(v(18,0)^2)*6.547499909120e+002*10^(-12),0))
IA_torq 30  0 0
B_phA_torq 30  0 v = if( (u(120-v(Shft_Real)))=1, (v(36,0)^2)*6.547499909120e+002*10^(-12), if ((u(v(Shft_Real)-
120)*u(240-v(Shft_Real)))=1,-(v(36,0)^2)*6.547499909120e+002*10^(-12),0))
VHV_HF 35  34 SIN( 0.000000000000e+000 6.790000000000e+002 1.000000000000e+003 0.000000000000e+000
0.000000000000e+000)
B2 A_sw  0 v = if( (u(v(Shft_Err)) *u(120-v(Shft_Real)))=1 # (u(-v(Shft_Err))*u(v(Shft_Real)-120)*u(240-
v(Shft_Real)))=1,1,0)
R7 A_sw  0 1k
B_torque Shft_Torque  0 v = v(30,0)+v(33,0)+v(57,0) - 0.0
A2 Shft_Desire  Shft_Desire_Diff differentiator
S_A_off 31  39  A_sw_n 0 switch off
S_B_off 27  41  B_sw_n 0 switch on
S_C_off 24  42  C_sw_n 0 switch on
XU4 37  Shft_Rad  0  Shft_Vel  Shft_Real  Shft_Mech  Speed_to_Position
VDesired_Spd_Profile Shft_Desire  0 PULSE( -5.000000000000e-001 5.000000000000e-001 0.000000000000e+000
5.000000000000e-001 3.500000000000e-001 1.000000000000e-001 1.000000000000e+000)
B1 Pre_Error  0 v = v(Shft_Desire)-v(Shft_Vel)
R5 Shft_Desire  0 1G
R9 B_sw  0 1k
```

```
B3 B_sw  0 v =  if((u(v(Shft_Err))*u(v(Shft_Real)-120)* u(240-v(Shft_Real)))=1 # (u(-v(Shft_Err))*u(v(Shft_Real)-
240))=1,1,0)
B4 C_sw  0 v =  if( (u(v(Shft_Err))*u(v(Shft_Real)-240))=1 # (u(-v(Shft_Err)) * u(120-v(Shft_Real)))=1, 1,0)
R10 C_sw  0 1k
R11 A_cap  0 1G
R12 B_cap  0 1G
AC_B_pwl %vd(Shft_Real   0)   %vd(B_cap   0)  pwl_B
R13 C_cap  0 1G
AC_C_pwl %vd(Shft_Real   0)   %vd(A_cap   0)  pwl_A
AC_A_pwl %vd(Shft_Real   0)   %vd(C_cap   0)  pwl
XU3 0  V_C  35  34  XMFR_custom
R14 A_sw_n  0 1k
R16 B_sw_n  0 1k
B7 C_sw_n  0 v = if( (v(C_sw,0)=0) & (abs(v(21,0))<50),1,0)
R17 C_sw_n  0 1k
B5 A_sw_n  0 v = if( (v(A_sw,0)=0) & (abs(v(36,0))<50),1,0)
R18 0  Shft_Mech 1Meg
B6 B_sw_n  0 v = if( (v(B_sw,0)=0) & (abs(v(18,0))<50),1,0)
R22 42  0 100
R21 41  0 100
R20 39  0 100
V1 clk_pulse  0 PULSE( 0.000000000000e+000 1.000000000000e+000 0.000000000000e+000 1.000000000000e-005
1.000000000000e-005 2.000000000000e-005 4.000000000000e-003)
B13 notQ  0 v = if( v(v_B2,0) =0, if( v(Shft_Err,0) =0,1,0),0)
B12 Shft_Err  0 v = if( v(v_B1,0) =0, if( v(notQ,0) =0,1,0),0)
R29 notQ  0 1G
B11 v_B2  0 v = if( ((v(Error,0)>0) & (v(clk_pulse,0)>0)), 1,0)
R28 v_B2  0 1G
B10 v_B1  0 v = if( ((-v(Error,0)>0) & (v(clk_pulse,0)>0)), 1,0)
R26 v_B1  0 1G
R23 clk_pulse  0 1G
R6 Shft_Err  0 1G
R27 Pre_Error  0 1G
C1 Shft_Err  0 25p
VAm1 36  31 0
VAm2 18  27 0
VAm3 21  24 0
B8 Error  0 v = if( ( abs(v(Pre_Error,0))<0.02), if(v(Shft_Desire_Diff,0)>0, -0.005, 0.005), v(Pre_Error,0))
R19 Error  0 1G
R15 Shft_Torque  0 1G
A1 Shft_Torque  Shft_Vel transfer_function
R1 Shft_Desire_Diff  0 1G
R24 Shft_Vel  0 1G

.model switch SW  vt = 1   vh = 0   ron = 1   roff = 1.000000000000e+009

.model pwl pwl  x_array = [0 60 120 180 240 300 360]   y_array = [23 13.8 2.3 2.3 2.3 13.8 23]   input_domain = .03

.model pwl_A pwl  x_array = [0 60 120 180 240 300 360]   y_array = [2.3 13.8 23 13.8 2.3 2.3 2.3]   input_domain = .03

.model pwl_B pwl  x_array = [0 60 120 180 240 300 360]   y_array = [2.3 2.3 2.3 13.8 23 13.8 2.3]   input_domain = .03

.model transfer_function s_xfer  num_coeff = [0 95.24]   den_coeff = [1 6.66]   int_ic = [0.0]   denormalized_freq = 1

.model differentiator d_dt  out_lower_limit = -1t   out_upper_limit = 1t


.TRAN  5E-6 2 0 2.5E-5 uic

.OPTIONS  gmin = 1e-14  reltol = 1E-4  abstol = 1nA  vntol = 100uV
+  temp = 27  itl1 = 1000  itl2 = 500  itl4 = 5000  gminsteps = 100
+  rshunt = 1Meg  bb_daOutLow = 0  bb_daOutHigh = 5  bb_daOutX = 2.5  bb_adInLow = .5
+  bb_adInHigh = 4.5
.end
```

References

[1] http://www.energy.gov/news/4503.htm
[2] http://www1.eere.energy.gov/femp/operations_maintenance/om_motors.html
[3] George Sutton, Arthur Sherman, *Engineering Magnetohydrodynamics*, McGraw-Hill, 1965
[4] Vassilis Lembessis, *P. N. Lebedev and Light Radiation Pressure;* Europhysics News (2001) Vol. 31 No. 7
[5] Tak Kenjo, *Electric Motors and their Controls*, Oxford University Press,1991.
[6] S. O. Kasap, *Electronic Materials and Devices*, McGraw-Hill Third Edition, 2006
[7] Piezo-Kinetics ®, www.piezo-kinetics.com, 11/9/06
[8] Robert G. Jahn, *Physics of Electric Propulsion*, McGraw-Hill, pg142-7, 1968.
[9] "Electrostatics and Its Applications", Wiley-Interscience Publication, A.D. Moore, pg 135
[10] B. Sujak, W. Heffner, *Acta Physica Polonica*, 1962 vol 23, pg715-726
[11] J.D.N Van Wyk, G.J. Kühn, *Nature*, 1961 vol 192, pg649-650
[12] Hidetaro Ho, "On Rotary Field Electrostatic Induction Motors"; IEE Japan, March 1901
[13] 'Vacuum Electrostatic Engineering', John G. Trump, PhD Dissertation, MIT 1933
[14] Al Wallash and Larry Levit; *Proceedings of SPIE* 2003, vol 4980, pg87-95
[15] Rakshit Tirumala and David B. Go; *An Analytical formulation for the Modified Paschen's Curve*, Applied Physics Letters vol 97, 2010
[16] Wang, Zhao et. all. *Applied Physics*, A-80 pg 1781-1787, 2005
[17] "*Numerical Conformal Mapping for Undergraduates", G* Warner and R Anderson, Int. J. of Electrical Engineering Education vol 18 pg 359-372, 1981
[18] "*Numerical Conformal Mapping for Undergraduates", G* Warner and R Anderson, Int. J. of Electrical Engineering Education vol 18 pg 359-372, 1981
[19] http://www.marubeni-sunnyvale.com/high_strengthened_glass.html ,9/3/2011

Vita

Birth: September 6, 1973 in Richmond, VA

MS Electrical Engineering, University of Tennessee, Knoxville TN — August 2005

BS Electrical Engineering, Mercer University, Macon GA — April 1998

Professional Experience

Founder and VP of Research and Development, Escent Technologies 1/10 to 9/11– Lexington, KY

Instructor, University of Kentucky, Electrical & Computer Engineering 5/07 to 7/07 - Lexington, KY

Project Engineer, Technicon Engineering, Automation Division 5/98 to 7/03 - Macon, GA

- Obtained patent #6,427,423 based on the project.

Fabrication Data System Contractor, Brown & Williamson Tobacco Corp. 5/97 to 5/98 - Macon, GA

Academic Publications and Projects

***Electric Methods of Force, IEEE* South East Conference** 3/07 – Richmond, VA

PhD Dissertation, *Design and Analysis of Switched Impedance* 8/05 to 12/11 - Lexington, KY

Masters Thesis, *Switched Reluctance Motor for Large Industrial* 8/03 to 8/05 - Knoxville,

- Won International Magnetics Association (IMA) Student Design Competition in 2004/2005.
- Obtained patent # 7,459,822 based on the project.

Graduate Analyst, National Transportation Research Center (NTRC) 7/04 to 8/05 - Knoxville,

Graduate Advisor , FORD 'FutureTruck' Competition 8/03 to 6/04 - Knoxville,

- Team won first place in National Instruments *LabView* software competition.